Università Degli Studi di Napoli "Federico II"

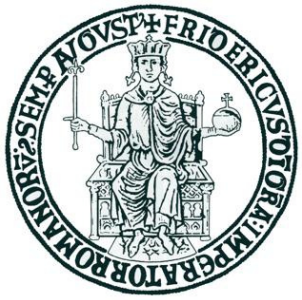

Ph.D. Thesis in Fundamental and Applied Physics

Data Quality Monitoring and Performance Studies of the Resistive Plate Chamber Detector at the CMS Experiment at LHC.

Supervisors:
Prof. Crisostomo Sciacca
Dr. Pierluigi Paolucci

Doctoral Candidate:
Anna Cimmino

XXIII Doctoral Cycle - 2007/2010

What is now proved,
was once only imagined.
W. Blake

What is now disproved,
was once thought self-evident.
T. D. Lee

Introduction

The Standard Model is a relativistic quantum field theory that encapsulates current knowledge of elementary particles and their interactions. The predictions of this theory coincide with observations in experiments with an astonishing precision. Still, the Standard Model falls short of being a complete theory of particle physics. A fair amount of theoretical and experimental research attempts to extend the Standard Model into a theory of everything, all foreseeing new physics at the TeV scale. Inadequacies of the Standard Model that motivate such research include: it does not incorporate gravity, it does not contain a viable candidate for dark matter, it requires a large number of constants whose values are unrelated and arbitrary, and it gives rise to the hierarchy problem, namely why the electro-weak scale and Planck scale are so disparate. Furthermore, the mechanism to give mass to particles is introduced *ad-hoc*, and requires the existence of a scalar boson, the Higgs boson, which is currently the only unobserved Standard Model particle.

Numerous extensions, revisions, replacements, and reorganizations of the Standard Model exist in attempt to correct for these and other issues. Unfortunately, there is, at present, no experimental evidence supporting one theory over the others. The Large Hadron Collider (LHC), at the European Organization for Nuclear Research (CERN), was built by with the intention of testing these various hypotheses, and searching for the hypothesized Higgs boson the entire allowed mass range. The LHC is the world's largest and highest-energy particle accelerator. Built in collaboration with over 10,000 scientists and engineers from more than 100 countries, it lies in a tunnel 27 km in circumference, as much as 175 m beneath the Franco-Swiss border near Geneva, Switzerland. This accelerator is designed to collide opposing particle beams of either protons at an energy of 7 TeV per particle, or lead nuclei at an energy of 574 TeV per nucleus.

The Compact Muon Solenoid (CMS) detector is one of the two multipurpose experiments at the LHC. As its name suggests, detecting muons is of central importance for CMS. Final state muons are expected to be produced in the decay of a number of hypothetical new particles and offer a clear signature for many interesting physics processes. CMS has a highly efficient and redundant muon system, which covers the tasks of muon identification,

momentum measurement and trigger. Three types of gas detectors are used. In the barrel region ($|\eta| < 1.2$), where neutron induced background is negligible, muon rate is low ($R(\mu) \lesssim Hz/cm^2$), and residual magnetic field is low, Drift Tube chambers (DT) are used. The endcap region, where muon rate as well as neutron and gamma background is high ($R(\mu) \lesssim 10$ kHz/cm^2, $R(n,\gamma) \lesssim 10$ kHz/cm^2), and the magnetic field is high as well, is instrumented with Cathode Strip Chambers (CSC), which cover up to $|\eta| < 2.4$. Finally, Resistive Plate Chambers (RPC), a dedicated trigger detector, are used in both barrel and endcaps, up to $|\eta| < 1.6$.

The CMS detector is a sophisticated and massive system: 7 different detector technologies, a high number of front-end electronic channels ($\sim 10^7$), an input rate of 10^9 interactions per second, a trigger able to reduce the frequency by a factor 10^5, and online computer farms with a storage capability rates of $\sim 10^2$ MB/s. CMS is foreseen to take data, with high efficiency, for over 15 years. Clearly, assuring pristine and stable behavior of each of its components is critical and delicate task.

The CMS collaboration designed and built, in tandem with detector commissioning, a high-level Data Quality Monitoring (DQM) system for the reliable certification of recorded data for physics analyses. DQM debugs hardware, monitors detector and trigger performance behavior, and highlight problems or malfunctioning by processing calibration and physics data.

The DQM system comprising tools for creation, filling, transport, archival, visualization, and retrieval of monitoring information. Data is harvested on a run-by-run basis, uploaded to a central Graphical User Interface, and stored to ROOT file. In the online environment, it provides current run information that can be used to overcome problems early on. During offline reconstruction, at Tier-0 and at the Tier-1s, more complex analysis of physics quantities is performed and results are used to assess the quality of reconstructed data. Offline DQM is also used to validate software releases, simulated data, and alignment/calibration results.

The DQM framework has been developed centrally by CMS and is based on the CMS reconstruction and physics analysis framework, CMSSW. Thus, it is flexible and easily customizable so to be used within different monitoring environments: online/offline DQM and private analysis code. Each subdetector and subsystem has developed its own DQM application closely following the requirements of its specific detector, electronics and trigger.

Definition of the requirements, design, and development of the RPC DQM system, as well as its use to study detector and trigger performance, have been the focus of this doctoral thesis work.

RPC data certification procedures are based on a set of well-understood physics parameters. Results provide important knowledge about the value of the data and how it can best be used. More than 3.2×10^4 histograms are produced per run. Summary layouts are provided to facilitate navigation

through the bulk of information.

It is a known fact, high levels of automation in monitoring processes reduce human errors and optimize recovery procedures. To this purpose, the Quality State Machine, a highly performing algorithm modeling detector behavior, was developed. It consists of a series of subsequent quality and statistical tests performed on a limited set of histograms. On the basis of these tests, chambers are grouped in a finite number of detector states: Good, Off, Dead, Partially Dead, Noisy Strips, Noisy Roll, Bad Occupancy Shape. Output of the Quality State Machine are 23 summary histograms, meaningful, not overwhelmed with information, and easy to interpret even by non-experts.

A new and complementary monitoring tool, History plotting tool for Data Quality Monitoring (HDQM), completes the RPC DQM system. HDQM allows to follow the evolution of RPC performance in time and across different runs, by extracting and analyzing summary information obtained from the run-based DQM histograms.

This doctoral thesis is structured as follows. Chapter 1 introduces the theoretical framework of the Standard Model and few of its possible extensions. Also, the LHC physics program is outlined. In chapter 2, the LHC accelerator design and operation are described, as well as the experimental setup of the CMS detector. The latter comprises the subdetectors, the data acquisition system, and the online event selection. A detailed survey of the CMS RPC system is given in chapter 3. A brief history of gas detectors, leading to the invention of RPCs, opens the chapter. Avalanche growth and signal formation are introduced. Subsequently, RPC design and operational parameters are defined. Special attention is given to conditions and requirements dictated by CMS. Finally, the use of RPCs as a dedicated muon trigger element in CMS is exploited. Chapter 4 concerns the DQM system, main topic of this thesis. Firstly, the framework used is concisely described. RPC monitoring requirements are reported, before presenting the structure of the RPC DQM systems. The Quality State Machine algorithm, used to asses detector conditions, is described thoroughly. Data certification procedures are listed. Results from 2009/2010 collision runs are given. HDQM for RPCs is here described for the first time. Numerous examples are shown of standard distributions and possible deviations. In the final chapter, DQM tools are used to study detector and trigger performance. RPCs are studied in terms of efficiency, cluster size, noise, and signal synchronization. 7 TeV collision data, recorded by CMS during 2010, are analyzed. Results with cosmic muons are also shown for comparison.

Contents

Chapter 1

Physics at Hadron Colliders

Current knowledge of elementary particle physics is the result of about a century of worldwide theoretical and experimental research. Its origins date as far back as 1895, with the discovery of X-rays by W.C. Röntgen. Since then, it has been a succession of brilliant theoretical predictions and revolutionary discoveries, starting from Curie's studies of radioactivity and culminating with the most recent discoveries of the top quark (1993) and neutrino oscillations (1998).

Today, elementary particles and their interactions are described by the Standard Model (SM), a field theory which combines special relativity and quantum mechanics. This description agrees extraordinary well with experimental observations. In fact, after about 35 years of extensive testing, its basic principles still hold. From the theoretical side, on the other hand, strong arguments support the interpretation of the SM as only an effective low-energy limit of some more profound theory. A number of equally possible models have been formulated by theoretical physicists to resolve the deficiencies and shortcoming of the SM.

Experimental verification or falsification of these theories requires the exploration of physics at the TeV energy scale. Hopefully an answer will arrive from the Large Hadron Collider (LHC), a proton-proton accelerator operating at the CERN laboratories in Geneva, Switzerland. The LHC has a design center-of-mass energy of 14 TeV and a luminosity of 10^{34} cm^{-2}s^{-2}. This challenging new collider offers the possibility to study a multitude of research topics, reaching from SM precision measurements, electro-weak symmetry breaking mechanism, Beyond Standard Model phenomena, to B-physics and quark-gluon plasma studies.

In section 1.1 the SM is reviewed. Emphasis is put on the conceptual description of interactions and on the theoretical and experimental endeavors to understand the origin of electro-weak symmetry breaking. In section 1.2, the need for new physics beyond the SM is exploited. Supersymmetry, Technicolor, and Extra-dimensions are introduced as appealing extensions.

Finally, the LHC physics program is introduced. A description of the accelerator is given in chapter 2.

1.1 Standard Model of Particle Physics

The Standard Model (SM) [1] of particle physics is a relativistic quantum field theory that describes the fundamental building blocks of matter and their interaction (with the exception of gravity). It combines the electroweak theory proposed by Glashow, Salam, and Weinberg [2, 3] to describe electromagnetic and weak interactions, based on the gauge symmetry group $SU(2)_L \times U(1)_Y$, with Quantum ChromoDynamics (QCD), which is the theory of strong interactions based on the $SU(3)_C$ symmetry group.

Within the SM, all constituents of matter are spin-1/2 particles, *fermions*. Interactions between fermions happen through the exchange of spin-1 particles, called *gauge bosons*, which are understood to arise from invariance of the theory under gauge symmetries. Fermions are divided into *quarks* and *leptons*, which come paired into three *generations*. No experimental evidence has been found so far for the existence of a fourth generation [4, 5, 6, 7].

$\begin{pmatrix} u \\ d \end{pmatrix}$	$\begin{pmatrix} c \\ s \end{pmatrix}$	$\begin{pmatrix} t \\ b \end{pmatrix}$
$\begin{pmatrix} \nu_e \\ e \end{pmatrix}$	$\begin{pmatrix} \nu_\mu \\ \mu \end{pmatrix}$	$\begin{pmatrix} \nu_\tau \\ \tau \end{pmatrix}$
1^{st} *generation*	2^{nd} *generation*	3^{rd} *generation*

There are 6 quarks, namely *up (u), down (d), charm (c), strange (s), top (t), and bottom (b).* Each lepton generation, instead, is formed by a electrically charged lepton and an associated *neutrino*, namely ν_e, ν_μ, and ν_τ for the *electron* (e), *muon* (μ) and *tau* (τ) respectively. All stable matter observed in the universe is made from the first generation of fermions. For each fermion, there exists a corresponding anti-particle with exactly same coupling, but with opposite quantum numbers.

Three types of fundamental interactions among fermions have been experimentally observed. Electromagnetic interactions are mediated by massless photons (γ), weak interactions by massive $W^\pm$ and Z bosons, while strong interactions are carried by massless *gluons*. Each different interaction is modeled by an independent gauge group. In its complexity, the SM is based on the local symmetry groups $SU(3)_C \times SU(2)_L \times U(1)_Y$. The fourth known fundamental interaction, gravity, is very difficult to observe

at sub-millimeter distances. Since the electromagnetic attraction between an electron and a proton is about 36 orders of magnitude larger than the corresponding gravitational attraction, gravity is negligible compared to the other interactions in today's particle physics experiments.

A comprehensive description of the SM is beyond the scope of this work. Only its main features are reviewed in the following sections.

1.1.1 Local Gauge Invariance in the SM

In the SM, a free fermion with mass m is described by Dirac's Lagrangian,

$$\mathcal{L} = i\bar{\psi}\gamma^{\mu}\partial_{\mu}\psi - m\bar{\psi}\psi, \tag{1.1}$$

as a spinor ψ, i.e. a 4-component complex field. Requiring $\mathcal{L}$ to be invariant under local phase transformations with rotation parameters $\vec{\epsilon}(x)$ in an internal space represented by the generators $\vec{\tau}$, as

$$\psi \to \psi' = U\psi = e^{i\vec{\epsilon}(x)\cdot\frac{\vec{\tau}}{2}}\psi, \tag{1.2}$$

introduces the substitution,

$$\partial_{\mu} \to \mathcal{D}_{\mu} = \partial_{\mu} - ig\frac{\vec{\tau}}{2}\vec{A}_{\mu}. \tag{1.3}$$

$\mathcal{D}_{\mu}$ is a covariant derivative, $\vec{A}_{\mu}$ is a vector field, and g is an arbitrary parameter that determines the interaction strength associated to the field. By demanding

$$\mathcal{D}_{\mu}\psi \to \mathcal{D'}_{\mu}\psi' = U(\mathcal{D}_{\mu}\psi), \tag{1.4}$$

to that the Lagrangian is invariant under 1.2, transformation relations for $\vec{A}_{\mu}$ may be easily derived.

It is found that the requirement of a theory to be invariant under gauge transformations entails the introduction of associated vector fields, called gauge fields. These fields imply the existence of spin-1 particles, the gauge bosons, that couple to the fermions. In addition, gauge bosons in a Yang-Mills theory, i.e. a theory with a local non-Abelian phase invariance, exhibit also self-interactions.

To describe experimental knowledge of elementary particles and their interactions at the quantum level, three symmetries are found to be necessary and sufficient in the SM: a local $U(1)$ phase invariance whose gauge field is traditionally denoted B_μ, an invariance under a set of non-Abelian transformations that form an SU(2) group leading to the introduction of three W_μ^i fields (i = 1,2,3), one for each of the three generators of SU(2), and a third invariance, also non-Abelian, under a set of transformations forming an SU(3) group, requiring the introduction of eight gauge fields, G_μ^a (a = 1, ... , 8). The covariant derivative, which ensures invariance under all three gauge transformations, takes the form

$$\mathcal{D}_\mu = \partial_\mu - ig_1\frac{Y}{2}B_\mu - ig_2\frac{\tau^i}{2}W_\mu^i - ig_3\frac{\lambda^a}{2}G_\mu^a, \tag{1.5}$$

where the scalar Y and the matrices τ^i and λ^a serve as a generators of the $U(1)_Y$ *hypercharge*, the $SU(2)_L$ *weak isospin*, and the $SU(3)_C$ *color* spaces.

The $SU(3)_C$ color charges are only present for quarks, which appear as triplets under $SU(3)_C$ transformations, while leptons are color singlets. There are three types of color charge: *red*, *blue* and *green*. Three quarks with different color charges bind together to make colorless *baryon*, and quark and anti-quarks, which carry opposite color charges, combine themselves to form colorless *mesons*. Finally, gluons transform as color octets.

In the framework of SU(2) gauge transformations, it is convenient to project Dirac spinors into left- and right-handed Weyl spinors ψ_L and ψ_R as

$$\psi = \begin{pmatrix} \psi_L \\ \psi_R \end{pmatrix}. \tag{1.6}$$

ψ_L and ψ_R have distinct chirality[1] and may be treated separately as long as fermions are taken to be massless. Any mass term, of the form

$$m\bar{\psi}\psi = m(\bar{\psi_R}\psi_L + \bar{\psi_L}\psi_R), \tag{1.7}$$

would inevitably mix the two components and, moreover, manifestly violate $SU(2)$ gauge invariance. Therefore, at this point, fermion mass terms must be excluded from the theory.

Weak-isospin charge turns out to be different for particles with different chirality. Left-handed fermions transform as isospin doublets within the

[1]For massless fermions, chirality corresponds to helicity,

lepton and quark families, while the right-handed counterparts transform as singlets with zero isospin and hence do not interact with $SU(2)$ gauge bosons. The W gauge bosons themselves appear as a triplet. The relevant quantum number for the particles is the third component, T_3, of the weak isospin T.

Finally, U(1) hypercharge is non-zero for all fermions except for right-handed neutrinos. As a convention, the corresponding quantum number Y is chosen equal to -1 for left-handed leptons. Since right-handed neutrinos do not couple to any of the introduced interactions, they are sterile, and do not form a part of the theory. Recent observations of neutrino oscillations, however, require an extension of the presented SM to include right-handed neutrinos [8].

Unlike strong and the $SU(3)_C$ interaction, $U(1)_Y$ and $SU(2)_L$ gauge interactions cannot be identified directly with the electromagnetic and weak interactions respectively. Instead, observed interactions are a manifestation of the combined electroweak $U(1)_Y \times SU(2)_L$ gauge group. This implies, among other things, that $Y = 2(Q - T_3)$, where Q is the observable electromagnetic charge. Physical fields A_μ, Z_μ and $W^\pm_\mu$, for the photon, the Z and the $W^\pm$ bosons respectively, arise as combinations of the gauge fields:

$$A_\mu = B_\mu cos\theta_W + W^3_\mu sin\theta_W, \tag{1.8}$$

$$Z_\mu = -B_\mu sin\theta_W + W^3_\mu cos\theta_W, \tag{1.9}$$

and

$$W^\pm_\mu = \sqrt{\frac{1}{2}} \left(W^1_\mu \pm W^2_\mu\right), \tag{1.10}$$

with θ_W being the *Weinberg angle*.

In Table 1.1 fermions and their main quantum numbers are summarized. Although right-handed neutrinos are not considered as part of the SM, they are mentioned for completeness.

1.1.2 The Origin of Mass: Higgs Sector

In the purely symmetric gauge theory presented above all particles are massless. Gauge invariance, and therefore renormalizability, does not allow mass terms in the Lagrangian. Fermionic mass terms would violate $SU(2)$ invariance. Also bosonic mass terms, of the form $-m^2 A_\mu A^\mu$ for the W and Z

Particle	Y	T	T_3	Q
$(\nu_{e,\mu,\tau})_L$	-1	1/2	+1/2	0
$(e,\ \mu,\ \tau)_L$	-1	1/2	-1/2	-1
$(\nu_{e,\mu,\tau})_R$	0	0	0	0
$(e,\ \mu,\ \tau)_R$	-2	0	0	-1
$(u,\ c,\ t)_L$	+1/3	1/2	+1/2	+2/3
$(d,\ s,\ b)_L$	+1/3	1/2	-1/2	-1/3
$(u,\ c,\ t)_R$	+4/3	0	0	+2/3
$(d,\ s,\ b)_R$	-2/3	0	0	-1/3

Table 1.1: Overview of the main quantum numbers for SM fermions.

bosons cannot be added without breaking gauge invariance. Massless gauge bosons would implies that associated forces have long range. This does non hold true for weak interactions. Hence gauge invariance must be broken and broken *spontaneously* to preserve renormalizability: the Lagrangian is kept invariant under gauge transformations, while the gauge symmetry of the vacuum is removed [9, 10, 11, 12].

In the SM, spontaneous symmetry breaking is achieved through the Higgs mechanism. A scalar field, that is a doublet in SU(2) space, carries non-zero U(1) hypercharge and is a singlet in SU(3) color space, is introduced. This field is known as the Higgs field ϕ:

$$\phi = \begin{pmatrix} \phi^+ \\ \phi^0 \end{pmatrix}, \tag{1.11}$$

with ϕ^+ and ϕ^0 complex fields. The invariant Lagrangian for this field can be written as:

$$\mathcal{L}_H = (D^\mu\phi)^\dagger(D_\mu\phi) - V(\phi) = (D^\mu\phi)^\dagger(D_\mu\phi) - \mu^2\phi^\dagger\phi - \lambda(\phi^\dagger\phi)^2, \tag{1.12}$$

where μ^2 is a mass parameter and $\lambda > 0$ is the Higgs field self-interaction strength. When $\mu^2 > 0$, the potential $V(\phi)$ has a global minimum for $\phi = 0$. Whereas, if $\mu^2 < 0$, $V(\phi)$ has non-vanishing degenerate minima for:

$$\phi^\dagger\phi = \frac{-\mu^2}{2\lambda} \equiv \frac{v^2}{2}. \tag{1.13}$$

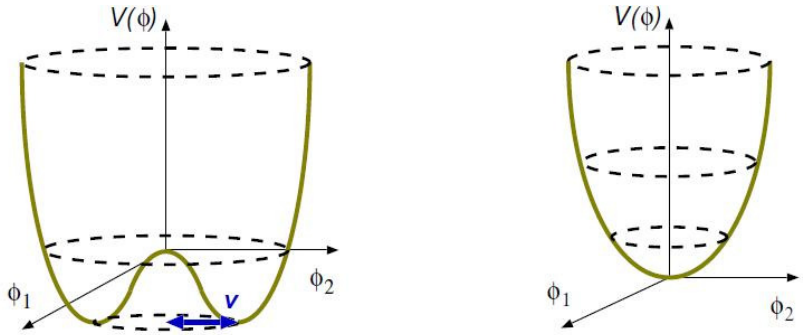

(a) $\mu^2 < 0$ (b) $\mu^2 > 0$

Figure 1.1: Two-dimensional representation of the Higgs potential in the case (a) of spontaneous symmetry breaking ($\mu^2 < 0$) and in the case (b) of an unbroken theory ($\mu^2 > 0$).

where v is the vacuum expectation value of ϕ. In two-dimensional representation, these degenerate vacua lie on a circle, as illustrated in figure 1.1 (a). The case $\mu^2 > 0$ is shown in figure 1.1 (b).

Choosing a particular value of ϕ for the ground state leads to spontaneous symmetry breaking. Without any loss of generality,

$$\phi = \frac{1}{\sqrt{2}} \begin{pmatrix} 0 \\ v + H(x) \end{pmatrix}, \tag{1.14}$$

where $H(x)$ is a real field. By inserting 1.14 in the Lagrangian, mass terms for the W and Z gauge bosons are generated,

$$m_W = \tfrac{1}{2} g v \quad m_Z = \tfrac{m_W}{2 cos\theta_W}, \tag{1.15}$$

while leaving the photon field massless. W and Z bosons were discovered at CERN by the UA1 [13] and UA2 [14] collaborations in 1983. Subsequent measurements of their masses and other properties have been in excellent agreement with the standard model expectations. The current values are [15]:

$$m_W = 80.399 \pm 0.023 \text{ GeV}; \quad m_Z = 91.1876 \pm 0.0021 \text{ GeV}. \tag{1.16}$$

On the other side, fermions acquire mass through Yukawa-like coupling terms added "by hand" to the Lagrangian. In other words, This difference in

treatment between gauge bosons and fermions has important consequences: fermion masses are free parameters within the theory.

The Higgs mechanism provides a remarkably simple and successful solution to electro-weak symmetry breaking problem. However the Higgs mass, $m_H = \sqrt{2\lambda}v$, can not be predicted by the theory. In fact, while $v = 246$ GeV can be inferred by equations 1.16 and by the measured value of m_W, λ is a free parameter of the theory. Nevertheless, theoretical constrains can be inferred by requiring perturbative consistency of the theory up to a scale Λ. An upper limit is obtained requiring λ to remain finite up to Λ (*triviality bound*). An accurate numerical analysis has been performed in [16], where for $\Lambda = 10^{19}$ GeV:

$$m_H[GeV] < 180 \pm 4(\text{th.}) \pm 5(\text{exp.}). \tag{1.17}$$

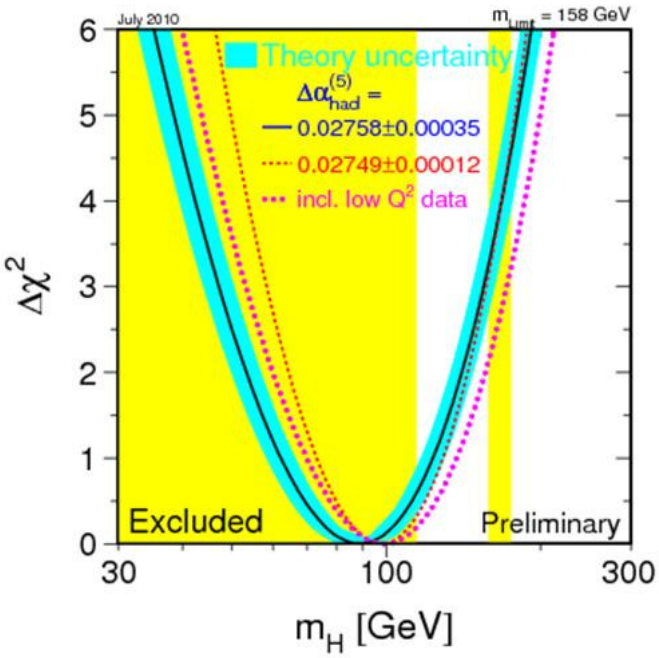

Figure 1.2: $\Delta\chi^2$ curve obtained from high-Q^2 precision electroweak measurements, performed at LEP and by SLD, CDF, and D$\emptyset$, as a function of the Higgs boson mass, assuming the Standard Model to be the correct theory of nature [22]

Instead, a lower limit is found by imposing $\lambda > 0$ after the inclusion of radiative corrections, at least up to Λ. This implies that Higgs potential is bounded from below, i.e. the minimum of the potential is absolute (*vacuum*

stability). A looser constraint is found by requiring such minimum to be local, instead of absolute (*metastability*). Numerical analysis, always for $\Lambda = 10^{19}$ GeV can be found in [17, 18]. Results can be summarized as [19]:

$$\begin{aligned} &\text{(stability)} && m_H[\text{GeV}] > 130.2 \pm 3\ \text{(th.)} \pm 4.3\ \text{(exp.)}, \\ &\text{(metastability)} && m_H[\text{GeV}] > 122 \pm 3\ \text{(th.)} \pm 5.1\ \text{(exp.)}. \end{aligned} \tag{1.18}$$

From an experimental point of view instead, present bounds on the SM Higgs mass are based on direct searches at LEP [20] and Tevatron [21], and on precision electroweak measurements, i.e. indirect searches. Figure 1.2 shows the $\Delta\chi^2$ curve obtained from high-Q^2 precision electroweak measurements, performed at LEP and by SLD, CDF, and D$\emptyset$, as a function of the Higgs boson mass, assuming the Standard Model to be the correct theory of nature [22]. Precision electroweak measurements suggest that the mass of the SM Higgs boson is lower than about 158 GeV (one-sided 95% confidence level upper limit derived from $\Delta\chi^2 = 2.7$ for the blue band, thus including both the experimental and the theoretical uncertainty). When LEP-2 direct search limit of ~ 114 GeV is included, this limit increases to 185 GeV. In fact, non-observation at LEP-2 in the process $e^+e^- \to ZH$ imposes the lower bound $m_H > 114.4$ GeV at 95% confidence level.

Also Tevatron experiments, CDF and D$\emptyset$, search for the SM Higgs boson. Their most recent combined result (July 2010) exclude the mass range 158 - 175 GeV at 95% confidence level [23].

1.2 Beyond the Standard Model

The SM is at once totally successful and manifestly incomplete. Despite its impressive experimental success, there is a general consensus it is not the ultimate description of nature. There are, in fact, a number of theoretical and phenomenological problems and shortcoming that do not find an explanation within the pure SM: why are there apparently only three generations of quarks and leptons, how can values of quark and lepton masses and mixing angles be explained, why is the strong CP-violating parameter so small, and what is the explanation of baryon asymmetry. Some other major arguments for new physics beyond the SM are summarized below.

Non-observation of the Higgs boson The Higgs mechanism is surely an appealing concept, thanks to its simplicity and conciseness. Nevertheless, unlike gauge interactions, which arise from an invariance principle, there is no conceptual foundation to the rather technical addition of the Higgs field to the theory. Plus, its non-observation leaves open the possibility that the Higgs boson is not responsible for electro-weak symmetry breaking.

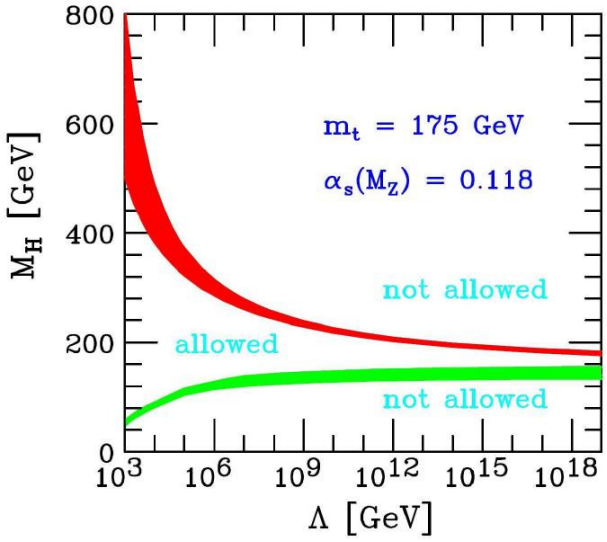

Figure 1.3: Theoretical constraints on the Higgs-boson mass, as a function of the SM energy cut-off, Λ [24].

From the theoretical side, as already explained in section 1.1, upper and lower bounds can be derived on the Higgs boson mass by requiring the SM to be self-consistent. In figure 1.3 these bounds on the SM Higgs boson mass are shown as a function of the cut-off scale Λ at which the SM is to be replaced by a higher energy theory [24].

In the region below the lower curve, called the vacuum-stability bound, the quartic Higgs boson coupling becomes negative and the potential is unbounded from below. The region above the upper curve, the triviality bound, is forbidden because it leads to a divergent Higgs boson self-coupling, causing a loss of perturbativity. The bound widths reflect the uncertainties in the determination of the Higgs boson mass limits. Additionally, if the validity of the SM is assumed up to the Planck mass scale, $m_P = 10^{19}$ GeV, the allowed Higgs boson mass range is between 130 and 190 GeV. Non-observation of a Higgs boson, or its observation outside these bounds, implies the existence of non-Standard Model physics at a energies below the Planck scale.

The hierarchy problem A typical scale for electro-weak physics is found to be of the order of $m_Z \sim 10^2$ GeV. The fundamental scale of gravity, however, the Planck mass scale $m_P \sim 10^{19}$ GeV, is much larger. In the SM, no new physics is expected between these scales, since all fundamental interactions, but the gravitational one, are already accounted for. This large discrepancy between both scales gives rise to

a difficulty referred to as the hierarchy problem.

In the SM the Higgs boson mass is not naturally small but tends to become heavy as the heaviest mass scale of the theory, which is the Plank scale ($m_P \sim 10^{19}$ GeV). In fact, the Higgs mass receives enormous quantum corrections from every particle that couples to the Higgs field. At one-loop level, these corrections are proportional to Λ^2, the square of the cut-off scale of the theory. Problem arises when Λ is of the order of m_P, because the quantum corrections are 34 orders of magnitude larger than the actual value m_H^2. Since fermion and boson loop corrections have different signs, they could cancel each other out. However, this cancellation would require a fine tuning, which is mathematically no problem, but rises doubts on the naturalness of the theory.

Unification of the coupling constants The success of the unified description of electromagnetism and weak interaction has led to the hope that all fundamental interactions can be described by a single symmetry group. If the Standard Model theory is expected to be self-consistent, running couplings, with two-loop corrections taken into account, are proved not to converge to a single value. Therefore, unification of the coupling constants is only expected with new physics at higher energies.

Gravity The SM does not describe gravitational interactions, and as such is incomplete. Attempts have been made to describe gravity as a quantum field theory, with the interaction mediated by a spin-2 boson, the *graviton*, associated to the gravitational tensor field. Such extensions of the SM, however, also require an adapted description of the SM itself, because of non-renormalizability problems.

Cosmological problems Astrophysical observations point towards the existence of a significant amount of neutral, non-baryonic matter, referred to as *dark matter*. Measurements from the cosmic microwave background shows the presence of six times more dark than baryonic matter in the universe [25]. The SM is rather silent when confronted with such issue. It can not provide a neutral, massive dark matter candidate whose relic density would be compatible with measurements.

Another cosmology related issue is the asymmetry between matter and antimatter experimentally constrained by the non-observation of antimatter in primordial cosmic rays. Theories of baryogenesis that try to explain this asymmetry, require CP violation at a level not allowed by the Standard Model. Such models also require baryon-number violation which is exactly conserved in the SM.

At this point, it is obvious the SM is incomplete and a more comprehensive theory is required. Over the years, scientific imagination has introduced many candidate theoretical models, but none have received yet experimental validation. Almost all predict the appearance of new phenomena in the energy region of the order of $\mathcal{O}(1\text{TeV})$. Some of the most promising candidate scenarios for physics beyond are briefly illustrated here.

1.2.1 Supersymmetry

SUperSYmmetry [26] is the most popular extension of the SM. It is based on the assumption that another symmetry exists in nature, which associates a bosonic state to a fermionic state, and vice versa. It can be shown that the operator Q, which generates such transformations, commutes with all space-time operators and also with generators of gauge transformations. Therefore particles in the same so-called *supermultiplet*, have the same mass and must have the same electric charge, weak isospin, and color charge. An inspection of SM particles and their quantum numbers shows the impossibility to find supersymmetric partners, *superpartners*, among known particles. Therefore supersymmetric models predict at least a doubling of the number of particles compared to the SM.

Since no superpartners of SM particles have been yet discovered, SUSY must be broken. Unfortunately, no simple mechanism exists for supersymmetry breaking, forcing physicist to treat the problem phenomenologically by adding terms to the Lagrangian that violate supersymmetry. It can be shown that the largest mass scale associated to these correction terms, must be of the order of $\mathcal{O}(1\text{TeV})$, which predicts supersymmetric particle within the LHC experimental reach.

Postulating the existence of a boson superpartner for each fermion and vice versa, naturally solves the hierarchy problem. Moreover, the running of coupling constants for all interactions now leads to converge in a single point, provided that the supersymmetric particle, *sparticle*, have masses of the order $\mathcal{O}(1\text{TeV})$.

In supersymmetric models, a new multiplicative quantum number, R-parity, is introduced. It is defined as follows:

$$P_R = (-1)^{3(B-L)+2S}, \tag{1.19}$$

where B is the baryon number, L the lepton number and S the the spin of the particle. This quantum number yields +1 for a SM particle and -1 for the superpartners. Its conservations implies that the Lightest Supersymmetric Particle (LSP) is stable and, therefore, a good candidate for dark matter.

Finally, SUSY elegantly incorporates gravity by allowing spin-2 particles, such as gravitons, to be introduced into the quantum theory of particle interactions.

The simplest supersymmetric model, called Minimal Supersymmetric Standard Model (MSSM), requires two Higgs doublets, corresponding to five Higgs particles: two charged bosons, $H^{\pm}$, two scalar bosons, h and H, and one pseudo-scalar, A.

1.2.2 Alternative SM Extensions

Several alternative ideas exist to mend some shortcomings of the SM in a different way than with supersymmetry. For example, introducing *extra space-time dimensions* in the theory can help to solve the hierarchy problem and to integrate gravity in the model at the quantum level. Instead of trying to cancel the divergences, the Planck scale is brought down to the TeV scale. As a consequence, at short distances ($\sim$ 2 mm in the case of two extra space dimensions) Newton's $1/r^2$ gravity law no longer holds. Since not much is known yet about gravity at short distances, these scenarios are not excluded by observations. *String theory*, which treat particles as extended objects, require extra dimensions along with supersymmetry.

Depending on the physical mechanism invoked to hide the extra dimensions from current observation, there is a large range of possible energy or length scales at which these new dimensions may start to appear. Nevertheless, even in the absence of a completely rigorous theoretical framework, phenomenological consequences can be explored. Many extra dimension scenarios predict that new particles like *radions* and *gravitons* can be produced at the TeV scale.

Other exotic scenarios have been proposed as alternatives beyond the SM. Grand Unified Theories (GUT) try to embed the SM gauge groups into one global symmetry group, hence unifying interactions and reducing the number of parameters in the model. In general new matter fields are needed in such scenarios. The *technicolour* approach postulates a new large gauge group, involving gauge interactions between new massless *technifermions*, which condensate into *technimesons* due to a strong QCD-like technicolor interaction. W and Z bosons acquire mass through interactions with the *technipions*, providing a dynamical nature to electro-weak symmetry breaking.

Recently, *little Higgs models* have been introduced that contain an alternative method for electro-weak symmetry breaking with new global symmetries which are both explicitly and spontaneously broken. Overviews of many of these models and scenarios can be found in [27, 28, 29, 30, 31].

1.3 LHC Physics Program

Several open issues in particle physics have been presented in the previous sections. Hopefully, an answers on the nature of electro-weak symmetry breaking and quest for Beyond Standard Model phenomena will come from

the Large Hadron Collider (LHC) [32], a challenging ($\mathcal{L} = 10^{34}\text{cm}^{-2}\text{s}^{-1}$ and $\sqrt{s} = 14$ TeV) new proton-proton accelerator built and operating at the CERN. Its design, described in the following chapter, has been driven by the goal to explore physics at the TeV scale. New phenomena are predicted at this scale, which follow from theoretical attempts to address the shortcomings of the SM. Here the main points of its rich physics program are given.

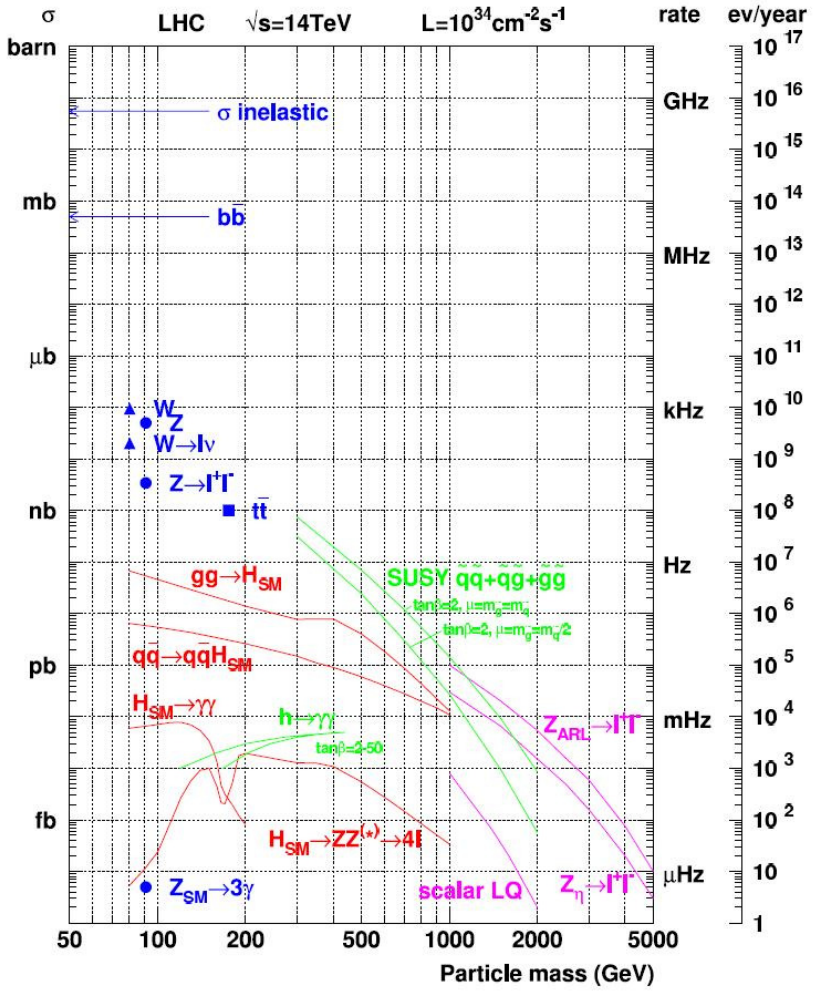

Figure 1.4: Overview of the cross sections of some major processes at the LHC as a function of the mass of the produced particle of interest.

The large increase in energy and luminosity at the LHC, compared to previous accelerators, opens a window to rare processes and objects of large mass and energy. In figure 1.4 an overview is given of the cross sections of

some major processes as a function of the mass of the produced particle. Also shown are the corresponding rates and number of events per year for the high-luminosity regime of the LHC.

Four main experiments take place at each LHC interaction point: two with general purpose detectors, ATLAS [34] and CMS [35], and two with dedicated detectors, ALICE [36] and LHC-b [37] which will study heavy ion physics and B-physics respectively. The bulk of the physics program will be conducted at the general purpose CMS and ATLAS detectors and can be subdivided in the three categories below. More detailed information on these topics can be found in [38, 39, 40, 41].

Higgs Searches The main processes contributing to the Higgs boson production at a hadron collider are represented by the Feynman diagrams in figure 1.5. Corresponding cross sections for a center-of-mass energy of $\sqrt{s} = 14$ TeV, which is the design value at LHC, are shown in figure 1.6. Gluon fusion is the dominant process over the whole Higgs boson mass spectrum. Boson fusion becomes comparable only for $m_H \gtrsim$ 800 GeV, but it offers an excellent signature with two forward jets in the final state. Also associated production processes, despite their low cross section, allow an easy background suppression. All the cross sections are of the order of a few picobarns. At LHC design luminosity this means an event rate of 10^2 Hz.

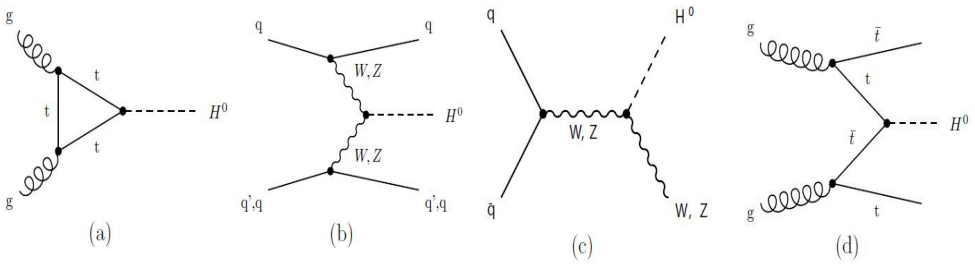

Figure 1.5: Higgs boson production mechanisms at tree level in proton-proton collisions: (a) gluon-gluon fusion; (b) vector boson fusion; (c) W and Z associated production (or Higgsstrahlung); (d) $\bar{t}t$ associated production.

Figure 1.7 shows the branching ratio for dominate decay modes as a function of m_H. For $m_H < 130$ GeV, the channel $H \to b\bar{b}$ dominant. However, the QCD jet background is so high at LHC that it will be almost impossible to observe this decay (except maybe by exploiting associated $t\bar{t}H$ or WH production.) The most promising channel is $H \to \gamma\gamma$, which despite the very low branching ratio ($\sim 10^{-3}$) has a very clean signature. For this channel, electromagnetic calorimetry

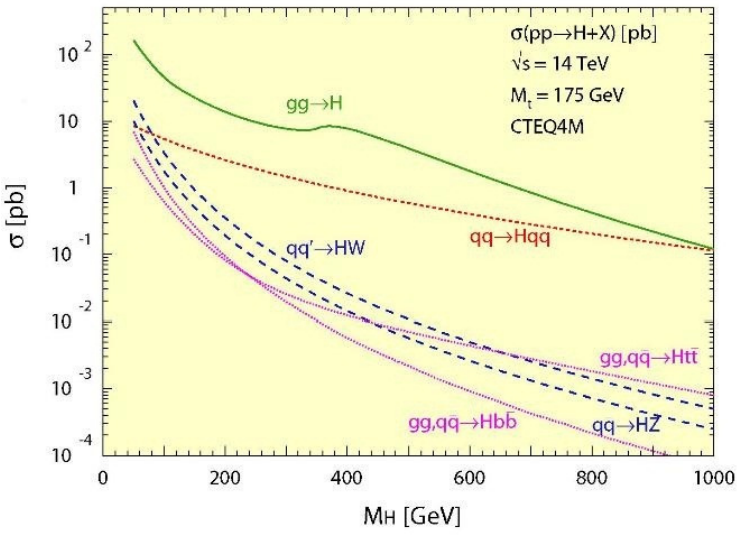

Figure 1.6: Higgs boson production cross sections at $\sqrt{s} = 14$ TeV as a function of the Higgs boson mass. [42]

with excellent granularity and energy resolution is needed, such that the small and narrow Higgs boson mass peak can be resolved on the exponentially decreasing background spectrum.

For a mass value $130 \leq m_H < 2m_Z$, the Higgs boson decays into $WW^{(*)}$ and ZZ^* quickly become dominant. The best discovery channels in this mass region are $H \to WW^{(*)} \to 2l2\nu$ and $H \to ZZ^* \to 4l$.

The branching ratio of $H \to WW^{(*)}$ is higher, because of the higher coupling of the Higgs boson to charged current with respect to neutral current. Moreover, this decay mode becomes particularly important in the mass region between $2m_W$ and $2m_Z$, where the Higgs boson can decay into two real W's. Unfortunately, the presence of neutrinos in the final state does not allow to reconstructed the Higgs mass.

The decay $ZZ^* \to 4l$, despite its lower branching ratio, offers a very clear experimental signature and high signal to background ratio. Furthermore, it allows to reconstruct the Higgs boson mass with high precision.

Finally, for higher mass values, the "golden decay channel" is still $H \to ZZ \to 4l$, but with both vector bosons on-shell. The upper mass limit for detecting the Higgs boson in this decay channel is given by the reduced production rate and the increased decay width of the Higgs boson. Semi-leptonic channels ($H \to ZZ \to lljj$ and $H \to WW \to l\nu jj$), that have a higher branching ratio compared to purely leptonic

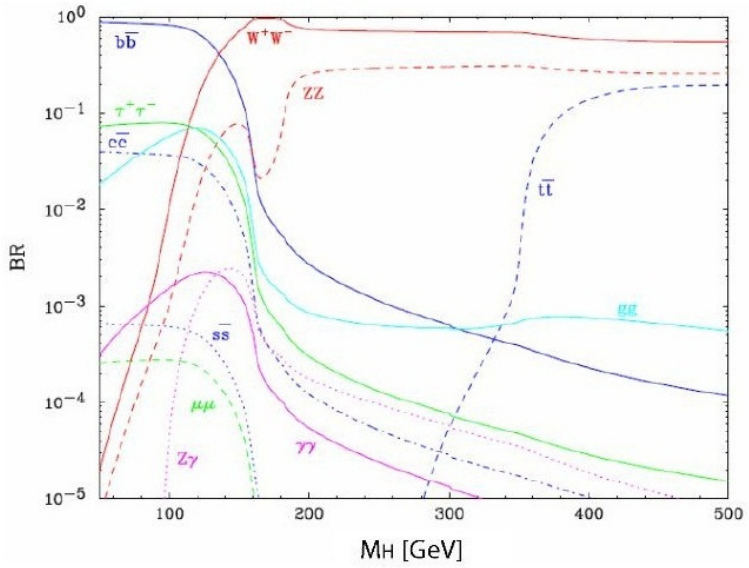

Figure 1.7: Branching ratios for dominant Higgs boson decay modes as a function of the Higgs boson mass. [42]

decays modes, must be used.

For supersymmetric Higgs bosons, signatures can deviate significantly from SM expectations, depending on the parameters of the investigated model. In the MSSM, the lightest Higgs boson h decays predominantly in τ and b quark pairs, except close to its upper mass limit, where it behaves like the SM Higgs boson. Also the H and A bosons decay mainly to b quarks and τ leptons, except for low tanβ, i.e. the ratio of the vacuum expectation values of the 2 Higgs doublets. Additionally, they are often produced in association with b quarks. Hence, good tracking capabilities are required to efficiently identify hadronic τ lepton and b quark decays.

Beyond Standard Model Phenomena Apart from an extended Higgs sector in the MSSM, many other supersymmetric signals can be searched for at the LHC. Since squarks and gluinos are colored particles, they are produced via strong interactions with relatively high cross sections. Assuming conservation of R-parity, defined in section 1.2.1, all decay chains of supersymmetric particles must end at the stable LSP, giving rise to signals of significant missing energy. Depending on sparticle mass hierarchy, also an abundance of leptons and quarks is expected in the final state, especially τ leptons and b quarks. Another possible signature is an excess of same-charged lepton pairs. Hence signals

from supersymmetry need a good lepton identification, hermetic energy measurements for missing energy determination, and an efficient τ and b identification.

A long list of other exotic models will be studied at the LHC, as Technicolor, Extra-dimensions, and Little Higgs, all with characteristic decay modes and signatures that can be searched for. Among the predicted final states are gravitons escaping into the extra dimensions, leading to hard single quarks or photons and large missing energy. Other models produce Drell-Yan-like graviton resonances or heavy vector bosons, with decays in very energetic electron, muon, photon, or quark pairs. To study the resulting energetic lepton signatures, sufficiently good track momentum resolution, particularly for muons, is needed.

Standard Model Physics A large part of the physics program of the LHC experiments will consist of SM physics. The main goal at start-up is the rediscovery of the W and Z bosons and the top quark. Because of their copious production, these particles can then be used as standard candles for calibration purposes. Once the detector performance is understood to an acceptable level, searches for physics beyond the SM will look for deviations from the SM expectations. In order to claim possible signals, the SM background will need to be well understood.

A list of precision measurements can be performed to further test the consistency of the SM. Electro-weak measurements can be taken into a yet unexplored energy domain. Measurements of the W and Z total and differential cross sections, and especially the study of multi-boson production and triple-gauge couplings, allow to further test the electro-weak gauge theory. The top quark sector of the SM provides a particularly rich environment for a multitude of analyses. For example, electro-weak production of single top quarks is of particular interest, since it has not been observed yet. Additionally, top quarks may decay through several rare decay modes involving flavor-changing neutral currents, not accessible with current experiments.

The LHC **b-physics** program is partly covered by CMS and ATLAS, but for its main part is explored by the dedicated LHCb experiment. In the field of b-physics, LHC benefits from a very large $b\bar{b}$ production cross section. The main interest is the study of the neutral B meson, and in particular, CP-violation in the $B_d^0 - \bar{B}_d^0$ and $B_s^0 - \bar{B}_s^0$ systems. In fact, CP-violation is one of an intriguing issue in particle physics. It was first discovered in the kaon system in 1964 and recently observed in neutral B decays [43].

Present experimental measurements confirm, within uncertainties, the CP-violation predicted by the SM, which is a consequence of the quark mass generation and of a phase in the quark-mixing matrix. However, this

amount of CP-violation is insufficient to explain baryogenesis and the ensuing matter-antimatter asymmetry in the universe, which calls for additional contributions from new physics. The task of present and future b-physics experiments is therefore to clarify this puzzle, by performing precise and redundant studies of CP-violating effects in the B-system, which should test the internal coherence of the SM, shed some light on the origin of CP-violation, and probe the existence of new physics.

Finally, the ALICE experiment aims to study properties of quark-gluon plasma with collisions of heavy ions. In fact, at the LHC it is also possible to collide lead ion beams at a center-of-mass energy of 1148 TeV. These collisions allow the study of strongly interacting matter in unprecedent conditions of energy and temperature, where a phase transition from ordinary hadronic matter to a plasma of deconfined quarks and gluons is supposed to take place. Since it is believed that the opposite transition occurred $\sim$ 10 μs after the Big Bang, these studies should shed light on the evolution of the early universe. Also, they should address the fundamental questions of quark confinement and approximate chiral-symmetry restoration.

Chapter 2

The Large Hadron Collider and the Compact Muon Solenoid

In the present chapter a concise overview of the Large Hadron Collider (LHC) design and operation is presented. Special attention is given to the Compact Muon Solenoid detector, one of the four main experiments that take place at the LHC.

2.1 The Large Hadron Collider

The Large Hadron Collider (LHC) [32], at the CERN laboratories [33] outside Geneva (Switzerland), is the largest and highest-energy particle accelerator and collider ever built. Designed to collide opposing particle beams of protons (p) at a center-of-mass energy of 14 TeV and a luminosity[1] of $\mathcal{L} = 10^{34}\text{cm}^{-2}\text{s}^{-1}$, it is located in a 27 km circular tunnel about 100 m beneath the French-Swiss border as shown in figure 2.1. In addition, during some dedicated runs, the LHC will collide heavy ion ($^{208}\text{Pb}^{82+}$) beams at energies of 2.76 TeV/nucleon, yielding a total center-of-mass energy of 1.148 PeV and a nominal luminosity of $\mathcal{L} = 10^{27}\text{cm}^{-2}\text{s}^{-1}$.

Four main experiments take place at each LHC interaction point: two with general purpose detectors, ATLAS [34] and CMS [35], and two with dedicated detectors, ALICE [36] and LHC-b [37] which will study heavy ion

[1] Luminosity is the number of collisions per unit time and cross-sectional area of the beams. It depends only on collider parameters. For circular accelerators, colliding bunches of n_1 and n_2 particles at a frequency f, the luminosity reads:

$$\mathcal{L} = f \frac{n_1 n_2}{4\pi\sigma_x\sigma_y} \ ,$$

where σ_x and σ_y characterize the Gaussian transverse beam profiles in the horizontal and vertical directions.

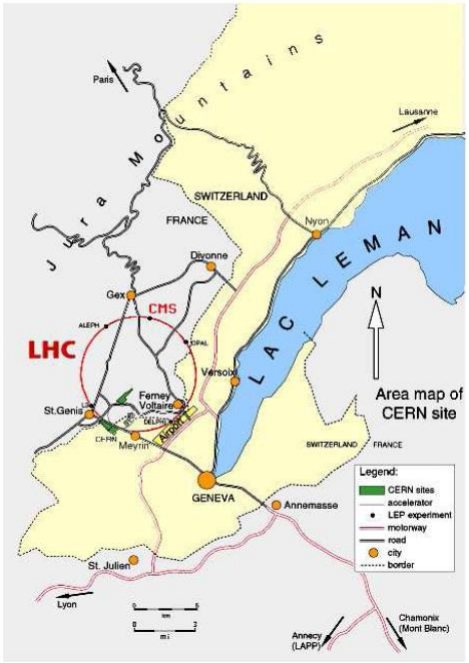

Figure 2.1: Geographical location of the Large Hadron Collider.

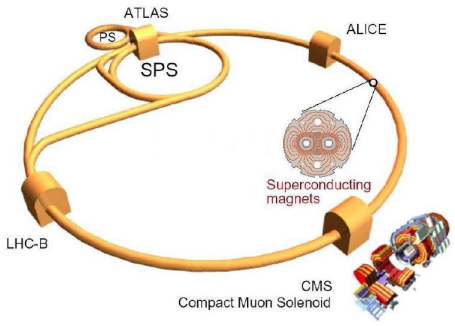

Figure 2.2: The four main experiments located in the various interaction points of the Large Hadron Collider.

physics and B-physics respectively. Figure 2.2 shows the four experimental sites along the LHC ring; the CMS experiment is highlighted.

2.1.1 Design and Operation

The physics goals described in the previous chapter have deeply influenced machine design. Design parameters for LHC are given in table 2.1 for both proton and lead beams.

The LHC is a proton-proton (p-p) collider. With respect to leptonic machine, it is easier to accelerate protons to high energy since energy lost for synchrotron radiation, inversely proportional to the fourth power of the particles mass, is much lower than for the electrons. With respect to a proton-antiproton machine, it is easier to accumulate high intensity beam of protons.

Figure 2.3 shows cross sections and production rates of some interesting processes as a function of the center-of-mass energy. Particularly, the Higgs cross section increases steeply with increasing energy, while the total cross section remains almost constant. Therefore the highest center-of-mass energy should be used. However, the size of the tunnel ($\sim$ 27 km) limits the center-of-mass energy to 14 TeV, since the beams must be bent by dipole magnets whose maximum field is currently limited at about 8 T. On the

Parameter	p-p	Pb-Pb
Center-of-mass energy (TeV)	14	1148
Number of particles per bunch	1.1×10^{11}	$\sim 8 \times 10^{7}$
Number of bunches	2808	608
Design Luminosity ($cm^{-2}s^{-1}$)	10^{34}	2×10^{27}
Bunch length (mm)	53	75
Beam radius at interaction point (μm)	15	15
Time between collisions (ns)	~ 25	124.75×10^{3}
Bunch crossing rate (MHz)	40.08	0.008
Circumference (km)	26.659	26.659
Dipole field (T)	8.3	8.3

Table 2.1: LHC parameters for p-p and Pb-Pb collisions.

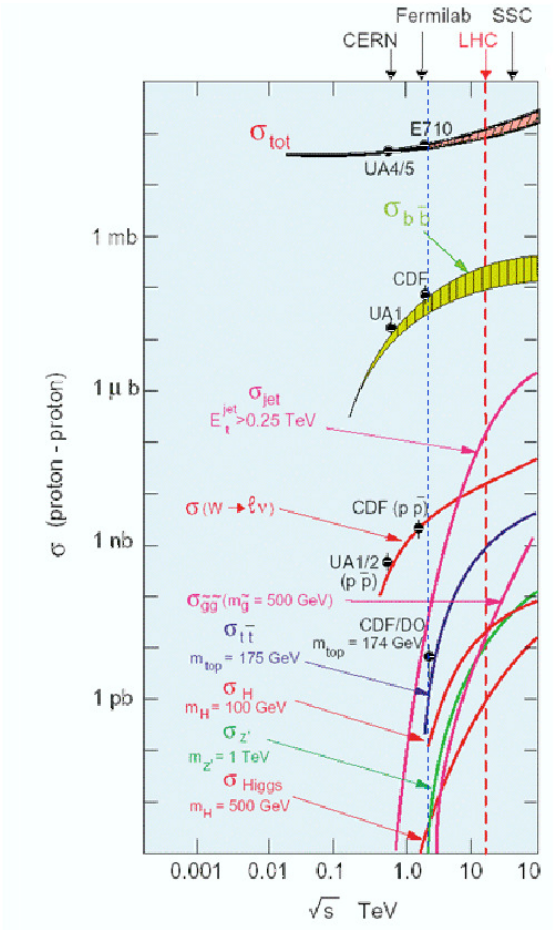

Figure 2.3: Cross sections as a function of the center-of-mass energy.

other hand, in hadron colliders the true participants in the scattering are the partons which carry a variable fraction of the beam's fourmomentum. Incoming partons carry momentum fractions x_1, $x_2 \sim 0.15$ - 0.20 of the incoming protons momenta, yielding a partonic center-of-mass energy $\sqrt{\hat{s}} = \sqrt{x_1 x_2 s} = 1$ - 2 TeV. Exactly the energy range to be explored.

To compensate for the low cross sections of interesting processes the LHC must have a very high luminosity: foreseen peak luminosity is 10^{34} cm^{-2}s^{-1} = 10 nb^{-1}s^{-1}. This corresponds to 100 fb^{-1}/year, considering 250 days of running and 12 h of run time per day. As a consequence of high luminosity, on average several interactions will happen during the same bunch crossing. For $\mathcal{L} = 10^{34}$cm^{-2}s^{-1} around 22 collisions, with about 50 charged tracks per interaction, are expected to overlap every bunch crossing [2]. The bunch structure is such that only about 80% of the bunches will be filled, i.e. 2808/3564 [44]. High event rate and pile-up of several events in the same bunch crossing dictate strict requirements on the design of LHC detectors. This is especially true for time response and readout electronics, which must be radiation-hard. Due to the presence of pile-up, high granularity is also required to avoid the overlap of particles in the same sensitive elements. High granularity means a large number of electronics channels, and therefore high cost. Additional requirements apply to the online trigger selection, that has to deal with a background rate several orders of magnitude higher than signal rate.

The CERN accelerator complex prepares beams before their injection in the LHC, as shown in figure 2.4: Linear Accelerator (LINAC2), Proton Synchrotron Booster (PSB), Proton Synchrotron (PS), and Super Proton Synchrotron (SPS). The protons produced at 92 keV are collected as an input to LINAC2, which increases their energy up to 50 MeV. In the next step, the PSB increases beam energy to 1.4 GeV. Protons are then accelerated up to 25 GeV by the PS, which builds up the proton bunches with a $\sim$ 25 ns separation and less than 4 ns time extension. Subsequently the SPS pushes particle energy up to 450 GeV and injects the beam into the LHC pipes. Inside the LHC accelerator, particles circulate in opposite directions in two separate beam pipes. 1232 superconducting dipoles and more than 2500 other magnets guide and squeeze the beams to a diameter of $\sim$ 16 μm. By design, bunches of 10^{11} protons will collide every 25 ns with an instantaneous luminosity $\mathcal{L} = 10^{34}$cm^{-2}s^{-1} and a center-of-mass energy of 14 TeV.

Lead ions, instead, start from a source of vaporized lead and enter LINAC3 before being collected and accelerated in the Low Energy Ion Ring

[2] In general, collision rate per bunch crossing (bx), for any process with cross section σ, may be evaluated by:
collisions/bx = $\sigma \cdot \mathcal{L}\cdot$ Bunch separation $\cdot$ Fraction filled bunches.
For LHC:
collisions/bx = 70×10^{-27} cm^{-2} $\cdot$ 10^{34} cm^{-2}s^{-1} $\cdot$ 25×10^{-9}s $\cdot$ 2808/3564 $\sim$ 22.

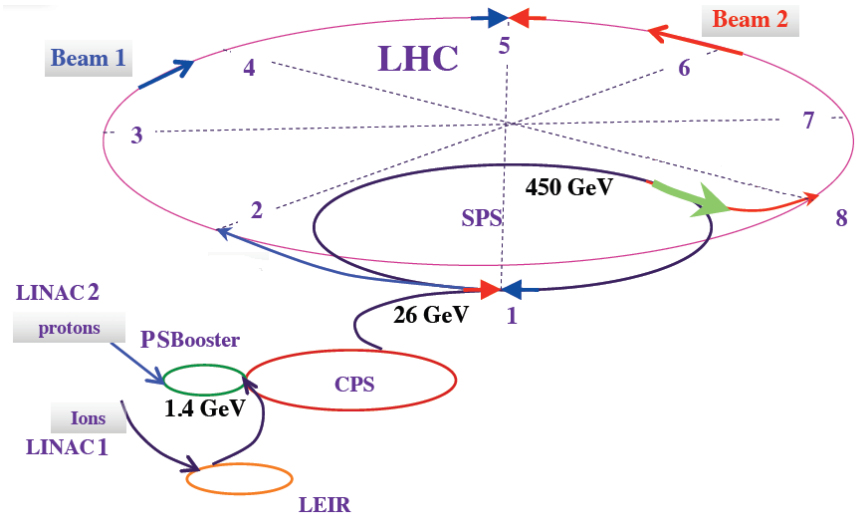

Figure 2.4: Schema of the CERN accelerator complex.

(LEIR). They then follow the same route to maximum acceleration as the protons.

On September 10^{th} 2008, proton beams were successfully circulated in the LHC for the first time. Exactly nine days later, operations were halted due to a serious incident with faulty electronic connection between two superconducting bending magnets. Repairing resulting damage and installing additional safety features took over a year. On November 20^{th} 2009 proton beams were successfully circulated again and only three days after, the first proton-proton collisions were recorded, at the injection energy of 450 GeV per particle. Beam energy was systematically increased until March 30^{th} 2010 when the first planned collisions took place between two 3.5 TeV beams, which set a new world record for the highest energy man-made particle collisions.

During 2010, LHC has delivered to the CMS experiment an integrated luminosity of 47.03 pb^{-1} with stable proton beams at 7 TeV center-of-mass energy, as shown in figure 2.5 [45]. The highest recorded instantaneous luminosity was 204.78 $\mu\text{b}^{-1}\text{s}^{-1}$ (figure 2.6).

On the 4^{th} of November 2010, commissioning of the accelerator for heavy ions began. Only four days later Alice, CMS, and Atlas recorded Pb-Pb collisions at a center-of-mass energy of 2.76 Tev per nucleon. This is 14 times higher than previously achieved by the Relativistic Heavy Ion Collider (RHIC) at Brookhaven National Laboratories, USA [46].

In 2012/2013 the LHC will be shut down for the upgrades necessary to bring it to its full design energy and luminosity. Upgrade operations are foreseen to last one year.

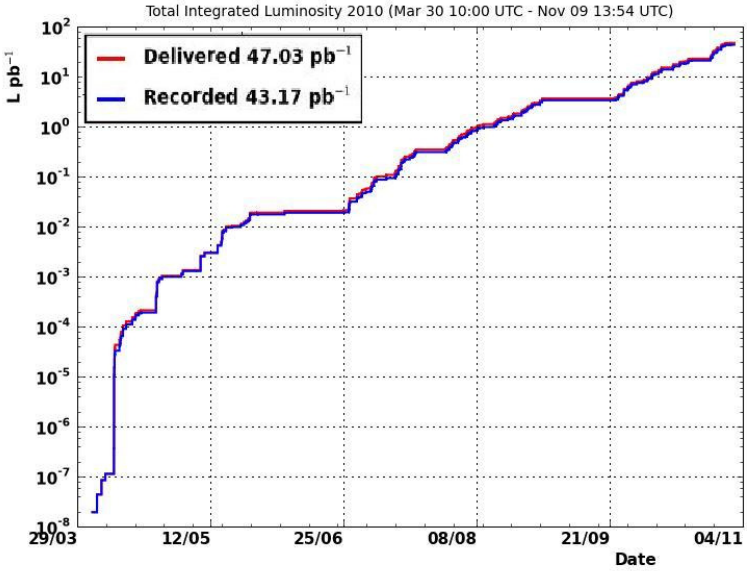

Figure 2.5: Integrated luminosity versus time delivered to (red), and recorded by CMS (blue) during stable beams at 7 TeV centre-of-mass energy [45].

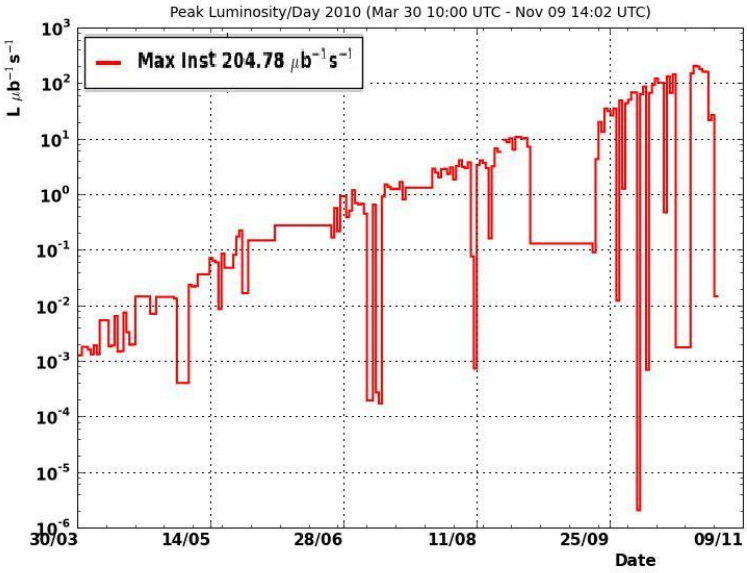

Figure 2.6: Maximum instantaneous luminosity per day delivered to CMS during stable beams at 7 TeV centre-of-mass energy [45].

2.2 The Compact Muon Solenoid

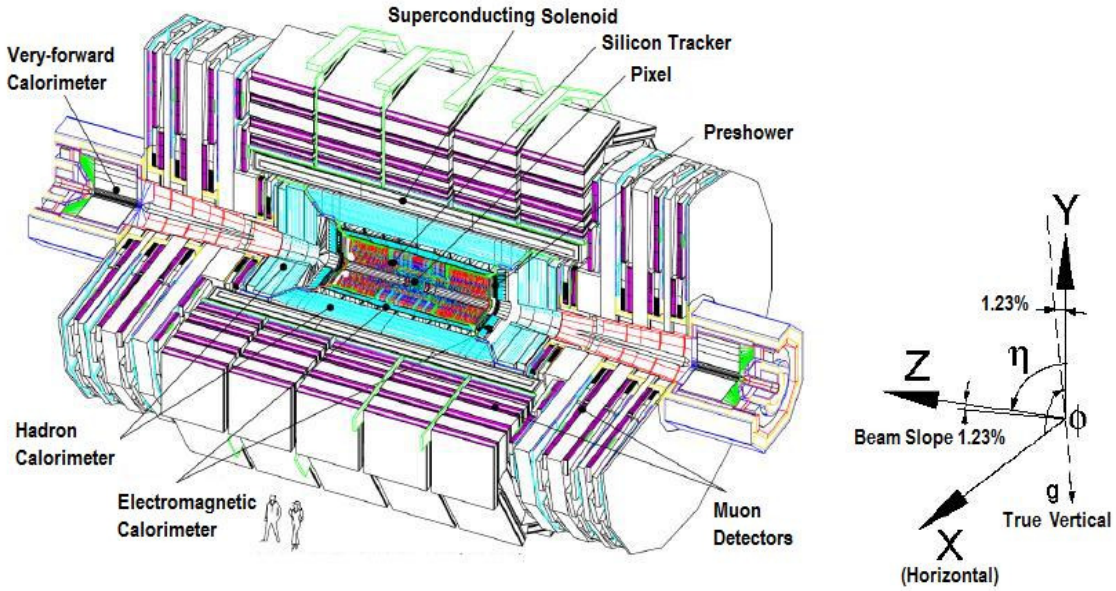

Figure 2.7: Prospective view of the CMS detector.

The Compact Muon Solenoid (CMS) [35] is one of the two general purpose detectors at the LHC. About 183 institutions of 38 countries, with more than 3600 scientists and engineers take part in the Collaboration. The CMS is designed to detect the signatures of new physics by identifying and precisely measuring μ, e and γ over a large energy range. Detector requirements for CMS to meet the goals of the LHC physics program (section 1.3) can be summarized as follows:

- A highly performing muon system: good muon identification and momentum resolution over a wide range of momenta and angles.
- Good electromagnetic energy resolution and efficient photon and lepton isolation at high luminosities.
- Good charged particle momentum resolution and reconstruction efficiency in the inner tracker.
- A hermetic hadron calorimeter with a large geometric coverage and fine lateral segmentation.

The general structure of CMS and the different subdetectors it holds are shown in figure 2.7. The coordinate system is such that the x-axis points

radially inwards, towards the center of the LHC, the y-axis points upwards, and the z-axis runs along the beam direction. The center of the detector is taken as the origin of the coordinate system. The azimuthal angle ϕ is measured in the x-y plane and the polar angle θ is the angle of inclination from the beam axis, i.e. the z-axis. Often however, the polar angle is expressed in terms of the pseudorapidity, η, defined as:

$$\eta = -\ln\left[\tan\left(\frac{\theta}{2}\right)\right]. \tag{2.1}$$

The CMS detector has a cylindrical symmetry around the LHC beam, with a diameter of 15 m and a length of 21.6 m. The detector is divided in the z-direction into five dodecagonal wheels, which form the *barrel* region and six disk, which constitute the *positive* and *negative* endcaps, or *forward* regions. Weight of the wheels and disks goes from 400 tons for the lightest up to 1920 tons for the central wheel.

Due to the requirement of an unambiguous determination of the sign of muons with a momentum up to 1TeV, a powerful superconducting solenoid magnet was chosen. It has a length of 12.9 m, an inner diameter of 5.9 m and operates at a field strength of 3.8 T ($\sim$ 19.5 kA). The magnetic field configuration influences the entire detector design. The inner tracking system, which measures the momentum of charged particle, and the main calorimetry are hosted inside the solenoid, whereas the muon system is embedded in the flux-return yoke. The different subdetectors will be briefly described in the next sections.

2.2.1 Tracker

The innermost element of the CMS detector is the silicon tracking system (Tracker) [47, 48]. The Tracker surrounds the interaction point with a radius of 4 cm $\lesssim r \lesssim$ 120 cm and a length of 5.8 m. Its design purpose is the precise and efficient measurement of charged particle trajectories, as well as a precise reconstruction of secondary vertices. At LHC design energy and luminosity, each bunch crossing will create on average about 1000 particles hitting the Tracker. This leads to a hit rate density of $\sim$ 2 MHz/mm^2 at a radius of 4 cm, $\sim$ 65 kHz/mm^2 at a r = 22 cm and $\sim$ 2.5 kHz/mm^2 at r = 115 cm. In order to keep the occupancy at or below 1%, high granularity detector are needed. In the region $r < 10$ cm, silicon pixels, with size 100 $\times$ 150 μm^2 in $r-\phi$ and z, are used. Thus, occupancy is of the order 10^{-4} per pixel and LHC bunch crossing (4 kHz per pixel). At higher radii reduced particle rates allow the use of silicon micro-strip detectors with a minimum strip size of 10 cm $\times$ 80 μm, leading to an occupancy of about 1 kHz per strip.

A schematic drawing of the CMS tracker is shown in figure 2.8, with its division in five subsystems: Pixel, Tracker Inner Barrel (TIB) and Tracker

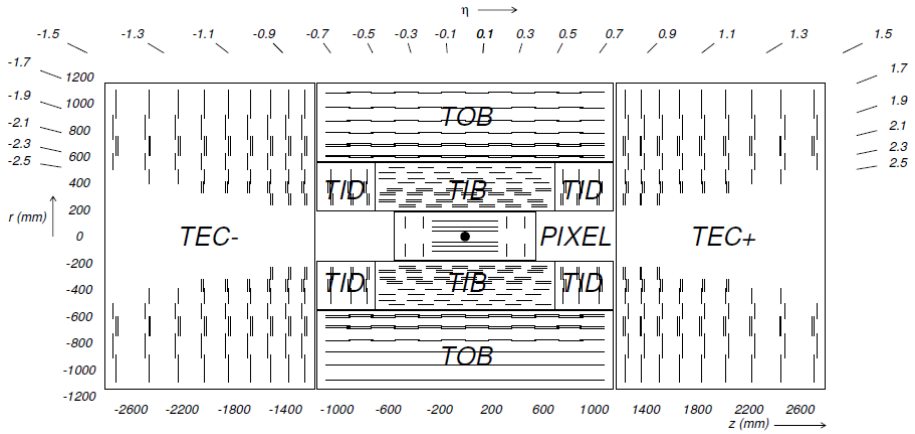

Figure 2.8: Schematic cross section of the CMS tracker with its division in subdetectors: Pixel, Tracker Inner Barrel (TIB) and Tracker Inner Disks (TID) Tracker Outer Barrel (TOB), and Tracker EndCaps (TEC+ and TEC-). Each line represents a detector module.

Inner Disks (TID), Tracker Outer Barrel (TOB), and Tracker EndCaps (TEC+ and TEC-). A total of 66 million pixel sensors cover an area of ~ 1 m^2. The silicon strip tracker instead features a total of 9.3 million strips and 198 m^2 of active silicon area. This detector layout ensures 3 high precision space points in the pixels and at least ~ 9 hits in the silicon strip tracker in the full range of $|\eta| < 2.4$. The ultimate acceptance of the tracker ends at $|\eta| \leq 2.5$. The achieved single point resolution is 230 μm^2 and 530 μm^2 in TIB and TOB respectively, and varies with pitch in TID and TEC.

2.2.2 Electromagnetic Calorimeter

CMS has chosen a very compact homogeneous scintillating crystal Electromagnetic Calorimeter (ECAL) [49, 50], designed for precision measurements of electron and photon energies and positions. Reconstruction of rare physics processes, such as the di-photon decay of the Standard Model Higgs boson as well as the identification of electrons from vector boson and τ-lepton related channels impose strict requirements on its performance.

Energy resolution (σ) of the electromagnetic calorimeter has been studied in dedicated test beams and can be parameterized as:

$$\left(\frac{\sigma}{\mathrm{E}}\right)^2 = \left(\frac{2.8\%}{\sqrt{\mathrm{E}}}\right)^2 + \left(\frac{0.12}{\mathrm{E}}\right)^2 + (0.30\%)^2\,, \tag{2.2}$$

where the first term on the right side of the equation is the stochastic term (event by event fluctuations, fluctuations in energy deposition, etc.), the sec-

ond is the noise term, and the third is a constant term related to calibration errors. E is the energy of the electromagnetic shower expressed in GeV.

The ECAL is positioned just outside the tracking system. Therefore it must cope with high hit rate density. High position resolution is achieved by using materials that provide small lateral and longitudinal spread of the electromagnetic shower. Lead tungstate ($PbWO_4$) crystals are used as scintillation material. $PbWO_4$ is characterized by small Molière radius[3] ($R_M = 2.2$ cm), high density (8.28 g/cm^3), short radiation length[4] ($X_0 = 0.89$ cm), fast response (80% of the light is emitted in the first 25 ns), and radiation hardness, thus realizing a very compact, high performing ECAL (e.g. with an energy resolution of 0.5% for 50 GeV particle). Light produced in the crystals is gathered with silicon avalanche photo-diodes.

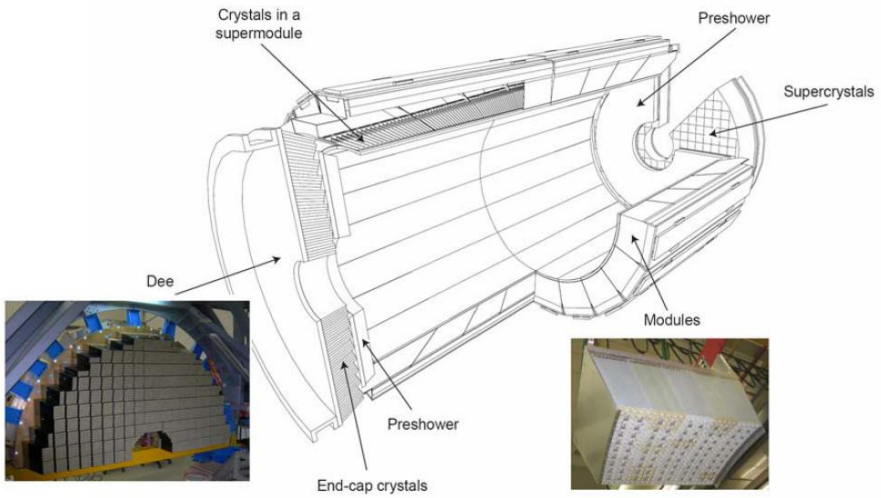

Figure 2.9: Schematic view of the CMS ECAL.

Similarly to other CMS subdetectors, the ECAL consists of a barrel and two endcap substructures, as illustrated in figure 2.9. The barrel (EB) covers the pseudorapidity range $|\eta| < 1.479$ and contains 61200 crystals assembled in 36 *supermodules*. Crystals are trapezoidal, with a front-face surface of 22×22 mm^2 translating in a 0.0174 rad coverage in η and ϕ. Crystal

[3]The Molière radius (R_M) of a material is defined as the radius of a cylinder containing on average 90% of the shower's energy deposition. It gives the scale of the transverse dimension of the fully contained electromagnetic showers initiated by an incident high energy electron or photon. A smaller Molière radius means better shower position resolution and better shower separation.

[4]By definition, the radiation length (X_0) of a material is the thickness of that material where pair production happens with a probability 1-e$^{-7/9}$ $\sim$ 54% for high energy photons. X_0 is related to R_M by the following approximated relation: $R_M = 0.0265X_0(Z+1.2)$. Z is the atomic number.

length is 23 cm corresponding to a radiation length of $25.8X_0$. All crystals point approximately toward the nominal interaction point with an offset of 3° in order to reduce energy loss for particles traversing exactly between two crystals. Total crystal volume amounts to 8.14 m^3, with an overall weight of 67.4 tons.

The endcaps (EE) cover the pseudorapidity range $1.479 < |\eta| < 3.0$. Each endcap is divided into 2 halves, or Dees. Each Dee holds 3662 crystals for an overall volume of 2.90 m^3 and a weight of 24.0 tons. Endcap crystals, compared to barrel ones, have a larger front face of 29 × 29 mm^2, but a shorter length of 22 cm corresponding to $\sim 25\ X_0$. They are arranged in a x - y grid in *supercrystals*, pointing approximately to the interaction point; crystal axes are tilted at 2° - 8° with respect to the direction pointing to the nominal vertex position.

Additionally, pre-shower detectors are inserted before each endcap. Their purpose is to identify neutral pions in the region $1.653 < |\eta| < 2.6$, help to identify of electrons against minimum ionizing particles, and improve position determination of electrons and photons. The pre-showers are sampling calorimeters formed by two layers: lead radiators initiate electromagnetic showers from incoming photons or electrons, while silicon strip sensors, placed after each radiator, measure energy deposits and transverse shower profiles. Total thickness of each pre-shower is 20 cm. Further details may be found in [51].

2.2.3 Hadron Calorimeter

The Hadron Calorimeter (HCAL) [52, 53, 54] plays a crucial role in the identification and measurement of quarks, gluons and neutrinos by measuring energy and direction of jets and missing transverse energy flow. The HCAL is made of copper layers interleaved with scintillator material. Its main features are good hermiticity, good transverse granularity, moderate energy resolution and sufficient depth for hadron shower containment.

Figure 2.10 is a longitudinal cut of a quarter of the hadron calorimeter. As seen from the interaction point, the hadron calorimeter barrel (HB) and endcaps (HE) are immediately behind the tracker and the electromagnetic calorimeter. Both HB and HE are sampling calorimeters with brass as the absorbing material and plastic scintillators as active elements. The scintillators are 4 mm thick tiles and are grouped in layers, called megatiles. Light emission from each tile is in the blue spectrum (λ = 410-425 nm).

HB is divided in 16 η sectors, resulting in a segmentation ($\Delta\eta$, $\Delta\phi$) = (0.087, 0.087), covering $|\eta| < 1.3$. It consists of 36 identical azimuthal wedges, which form the two half-barrels (HB+ and HB-). Each wedge is a 20 degree stack. The endcap calorimeters instead are attached to the muon endcaps and correspond to 10 interaction lengths. They are about 1.8 m thick, with an inner radius of 40 cm and outer radius of about 3 m. HE

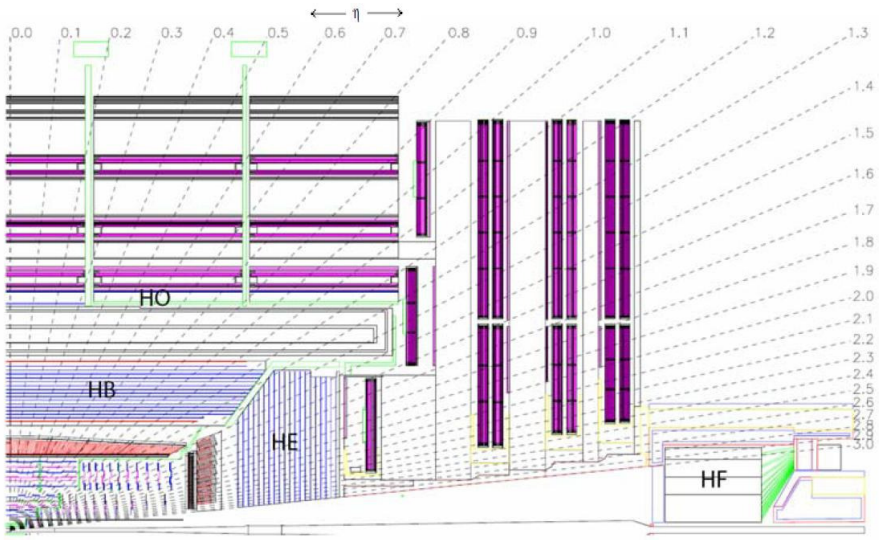

Figure 2.10: Schematic view of the CMS HCAL.

covers the $|\eta|$ range from 1.3 to 3.0. The energy resolution is $\frac{\sigma}{\mathrm{E}} \sim \frac{85\%}{\sqrt{\mathrm{E}}} \oplus 7.5\%$ for barrel and endcaps.

HB is radially restricted between the outer part of the electromagnetic calorimeter (r_{min} = 1.77 m) and the inner part of the magnet coil (r_{max} = 2.95 m). This constrains the total amount of material which can be put in to absorb hadronic showers. Therefore, an outer hadron calorimeter (HO), or tail catcher, is placed outside the solenoid complementing the barrel calorimeter. The very-forward hadron calorimeters (HF), placed at ±11.2 m from the interaction point, use a Cerenkov-based radiation-hard technology and extend the pseudorapidity coverage down to $|\eta| \sim 5.2$.

2.2.4 The Muon System

Muons are powerful tools to recognize signatures of interesting processes over the very high QCD background rate expected at LHC. A “gold plated” signal for Higgs detection is its decay in Z - $Z(^*) \rightarrow 4$ charged leptons. If the leptons are muons, the best 4-particle mass resolution can be achieved. Top and B-physics depends greatly on the ability to trigger on and identify muons. Also, many SUSY processes involve muons in the final state. It is therefore not surprising that great effort has been put in the design and construction of the CMS muon system.

The muon system has the tasks of muon identification, momentum measurement and triggering. Good transverse muon momentum resolution is enabled by the high magnetic field. The big amount of material and the flux-

return yoke serves as hadron absorber. Negligible punch-through reaches the system since the amount of material in front of the muon system exceeds 16 interaction lengths.

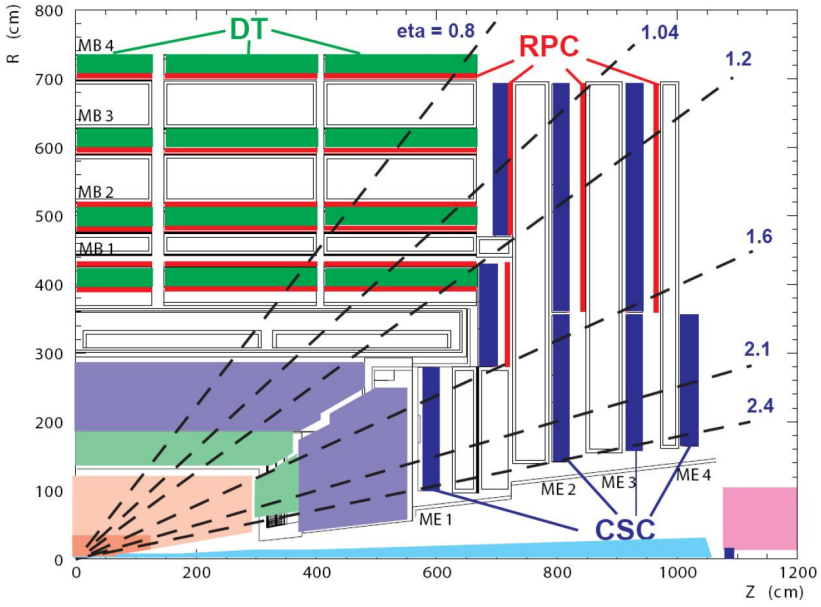

Figure 2.11: Longitudinal view of one quarter of the CMS muon system.

The muon system has a cylindrical *barrel* section and 2 planar *endcap* regions covering the full pseudorapidity interval $|\eta| < 2.4$ with no acceptance gaps. Figure 2.11 offers a schematic view of the muon system. In the barrel region, where neutron-induced background is small, the muon rate is low ($\lesssim$ Hz/cm^2) and the magnetic field is uniform ($\sim$ 1.8 T) and mostly contained in the steel yoke, **Drift Tubes** (DT) are used. DT chambers cover the pseudorapidity region $|\eta| < 1.2$ and are organized into 4 *muon stations* (MB1 - MB4) interleaved among the layers of the flux return plates. Each chamber holds 12 layers of contiguous standard rectangular drift cells, grouped in three SuperLayers (SL) with four staggered layers each. The innermost and outermost SLs are dedicated to hit measurement in the CMS bending plane (r - ϕ plane), while hits in the central SL are measured along the beam axis. The outermost station (MB4,) located outside the iron return yokes, has only two SLs measuring hit positions in the r - ϕ plane. Each cell has an area of 13 $\times$ 4.2 cm^2 where 4.2 cm is the distance between two consecutive anode wires. Cells are separated by 1 mm thick aluminium and have an offset of half cell, with respect to the upper and lower neighbor cell.

With this design, reconstruction efficiency is better than 95% for high p_T muon track in the pseudorapidity range covered by four stations ($|\eta| <$

0.8) and with momentum measurement delivered by the barrel muon system alone. The 100 μm target chamber resolution in r - ϕ plane is achieved by the 8 track points measured in the two SLs, the single wire resolution being better than 250 μm. The DT system consists of 130 chambers, 60 chambers located in the inner three wheel(W0,W$\pm$1) and 70 chambers in the outer ones(W$\pm$2), with about 172000 sensitive wires.

In the two endcap regions, where muon rates ($\lesssim$ kHz/cm^2) and background levels (comparable to muon rate) are high and the magnetic field is non-uniform (up to $\sim$ 3.5 T), **Cathode Strip Chambers** (CSC) are employed. CSCs are multiwire proportional chambers with fast response time, fine segmentation, and good radiation resistance. 6 anode wire planes interleaved among 7 cathode panels. The panels form 6 gas gaps planes of sensitive anode wires. Wires run azimuthally and define the track radial coordinate. Strips are milled on cathode panels and run lengthwise at constant $\Delta\phi$ width. Muon coordinate along the wires, the ϕ coordinate, is obtained by interpolating charges induced on the strips. An avalanche developed on a wire induces on the cathode plane a distributed charge of well known shape. Chamber orthogonal segmentation allows the calculation of two coordinates from a single plane.

There are 4 layers of CSCs in each endcap, called stations ME1, ME2, ME3, amd ME4. Station ME1 has three rings of chambers (ME1/1, ME1/2, ME1/3), while the other two stations are composed from two rings of chambers (MEn/1 and MEn/2, n = 2, 3, 4). At the time of the LHC start-up, 468 trapezoidal cathode strip chambers are installed in the muon endcap system, covering the region $0.9 < |\eta| < 2.4$. In the endcap-barrel overlap range, $0.9 < |\eta| < 1.2$, muons are detected by both the barrel DTs and endcap CSCs. The overall area covered by the sensitive planes of all chambers is about 5000 m^2, the gas volume is about 50 m^3, and the number of wires is about 2 million. The nominal gas mixture is 40%Ar + 50%CO_2 + 10%CF_4. Ar functions as the active component, CO_2 is a non-flammable quencher needed to achieve large gas gains, while the main function of the CF_4 is to prevent polymerization on wires.

Redundancy and robustness is insured by **Resistive Plate Chambers** (RPC) added in the barrel and both endcap regions. RPCs are gaseous parallel-plate detectors that combine adequate spatial resolution with a time resolution comparable to that of scintillators (order of ns). A total of 6 layers of RPCs are embedded in the barrel muon system, two (RB1in - RB1out, RB2in - RB2out) in each of the first two muon stations, and one (RB3 and RB4) in each of the last 2 stations. The redundancy in the first 2 stations allows trigger algorithms to work even for low-p_T tracks that may stop before reaching the outer 2 stations. There are 480 chambers in the barrel region, distributed equally among the 5 wheel (W-2, W-1, W0, W+1, W+2). Each wheel in divided in ϕ in 12 *sectors* (S01 - S12). S01 lays along the positive x-axis. Chambers are divided in η in 2 or 3 segments, or *rolls*, denoted:

Backward, Middle, and Forward.

The forward regions, instead, counts 756 chambers evenly spread over 6 disks (D-3, D-2, D-1, D+1, D+2, D+3): three on each side of the interaction point, denoted as *negative* and *positive* sides. Endcap disks stand parallel to the x-y plane and are divided in 60 ° sectors in ϕ. Chambers are trapezoidal, 10° in the azimuthal angle, and are arranged in two concentric *rings* (R2, R3). Within a ring, chambers are indicated as *segment* CH01 through CH36. Segment CH01 lays on the positive x-axis direction and the numbering proceeds anti-clockwise as seen from the interaction point. Endcap chambers are all divided in η in three roll (A, B, C).

Total detector coverage is presently $|\eta| < 1.6$, but original designs foresaw the installation of RPCs up to $\eta = \pm$ 2.1. Due to budget limitation this, along with the construction of a fourth endcap layer, has been postponed .

CMS RPC chambers have a double-gap design. Two separate gas gaps, referred as *up* and *down* gaps, are coupled together common pick-up readout strips in between. The total induced signal is the sum of the 2 single-gap signals. When an ionizing particle traverses a RPC, a cluster of electrons starts an avalanche multiplication. The drift of the charge towards the anode induces on the pick-up electrode a fast charge which represents the useful signal. The double-gaps configuration allows the single-gaps to operate at lower gas gain (lower high voltage) with an effective detector efficiency higher than for a single-gap. The pick-up strips run along the beam axis in the barrel and are radial in the endcaps. Their length and pitch vary with chamber position. A general description of RPC detectors is given the next chapter. Specific detector conditions and requirements imposed by CMS are discussed in section 3.4.

The DT/CSC and RPC systems have complementary characteristics and respond differently to the same background. DTs and CSCs are more vulnerable to radiation associated with muons at high p_T ($>$ 100GeV). This radiation is made of electromagnetic showers produced by e^+ - e^- pairs, bremsstrahlung or nuclear interactions. The effect is a poor local reconstruction. On the other hand, RPCs suffer from low energy backgrounds and intrinsic noise. Accidental multiple noise hits can be confused with a signal. This is less probable in DTs and CSCs where coincidence of many layers in a single station is used for particle reconstruction.

Finally, a sophisticated alignment system measures the positions of the muon detectors with respect to each other and to the inner tracker, in order to optimize muon momentum resolution. In fact, using only information from the muon system, p_T resolution (*standalone* resolution) has been measured to be $\frac{\Delta p_T}{p_T}$ = 8 - 15 % at 10 GeV and 20 - 40 % at 1 TeV. Adding tracker data, it (*global* resolution) improves to 1 - 1.5 % at 10 GeV and 6 - 17 % at 1 TeV.

2.2.5 Trigger and Data Acquisition System

The CMS Trigger and Data Acquisition System (TriDAS) is designed to analyze, select, and collect detector information at LHC bunch crossing frequency, 40 MHz. At the design luminosity of 10^{34} $cm^{-2}s^{-1}$, an average of 22 proton-proton events occur per bunch crossing. In other words, 10^9 interactions happen every second. Since the maximum rate present day data acquisition and data storage facilities can handle is 100 Hz, a reduction factor of 10^7 is required. In CMS, data reduction is achieved in two steps called trigger levels (figure 2.12): **Level-1 Trigger** (L1) and **High Level Trigger** (HLT).

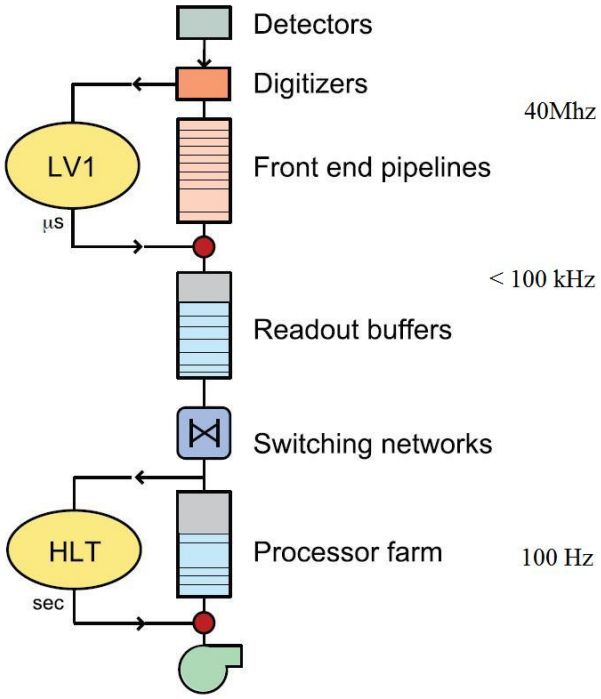

Figure 2.12: Schematic view of the CMS Trigger system, in which the different trigger levels and event rates are shown.

The L1 trigger is designed to reduce the incoming data rate to a maximum of 100 kHz, by processing fast coarsely segmented trigger information coming from the calorimeters and the muon chambers, and selecting events with interesting signatures. Decisions are taken on the presence of local objects such as photons, electrons, muons, and jets, using information from calorimeters, and muon systems in a given element of η - ϕ space, or *trigger towers*. It also employs global sums of E_T and missing E_T.

The L1 Trigger System is organized into three major subsystems (figure

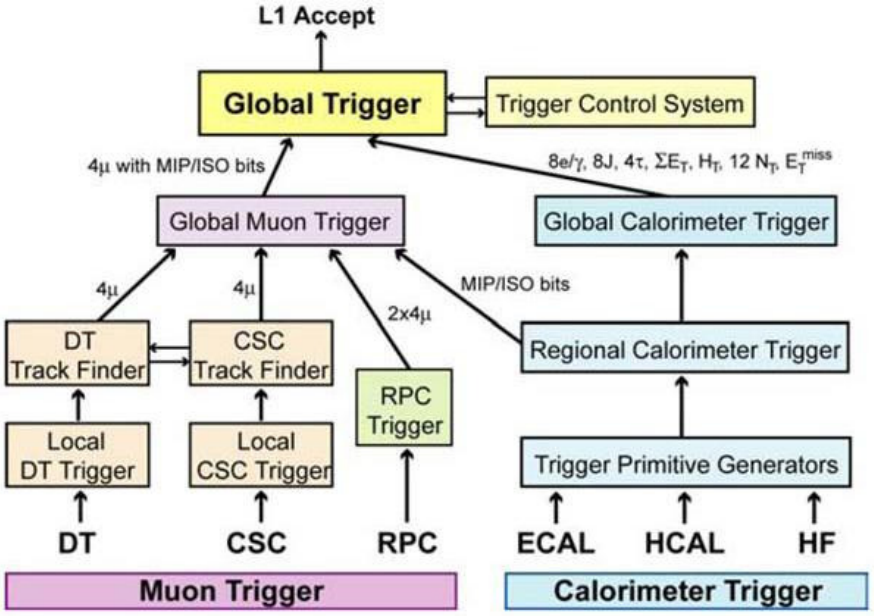

Figure 2.13: Architecture of the Level-1 Trigger.

2.13): the Calorimeter Trigger, the Muon Trigger, and the Global Trigger. The Calorimeter Trigger measures local energy sums formed by the ECAL, HCAL and HF upper level readout Trigger Primitive Generator (TPG) circuits. For the ECAL, these energies are accompanied by a bit indicating the transverse extent of the electromagnetic energy deposit. TPG information is transmitted over high speed copper links to the Regional Calorimeter Trigger (RCT), which finds candidate electrons, γs, τs, and jets and transmits them to the Global Calorimeter Trigger (GCT), along with sums of transverse energy. The GCT forwards the best 4 of each candidate type to the Global Trigger. The GCT also calculates total transverse energy and total missing energy vector. RCT also transmits an η - ϕ grid of quiet regions, where the energy deposit are below a programmable threshold, and MIP bits, i.e. energy deposits compatible with Minimum Ionizing Particle, to the Global Muon Trigger for muon isolation cuts.

The Muon Trigger is further organized into regional triggers representing the 3 different muon detector systems (DT, CSC, RPC). Barrel DT chambers provide local trigger information in the form of track segments in the ϕ-projection and hit patterns in the η-projection. On the other hand, endcap CSCs deliver 3-dimensional track segments. Additionally RPCs, with their excellent timing resolution, deliver their own track candidates based on regional hit patterns. Finally, the Global Muon Trigger (GMT) combines trigger information from all three systems and sends it to the L1 Global

Trigger (GT). More is said in chapter 3 on the architecture of the muon trigger, particularly on the role covered by the RPC regional trigger.

GCT and GMT determine the highest-rank calorimeter and muon objects across the entire experiment. The best 4 muons candidates, 4 non-isolated and 4 isolated e/γ, 4 central and 4 forward hadronic jets, 4 τ-jets, plus total E_T, and missing E_T are sent to the Global Trigger (GT) [57]. The GT works out the final trigger decision applying physics trigger requirements to those objects.

L1 trigger is based on custom made hardware. Trigger latency, between a given bunch crossing and distribution of the trigger decision to the detector front-end electronics, is 3.2 μs. This is imposed by the amount of data storage in the tracker and pre-shower front-end buffers

After the L1 accept signal, further event filtering is performed by the HLT. The HLT executes more complex physics selection algorithms on commercial computer, in order to accept only events with the most interesting physics content. The total processing time is ~ 1 s/event, after which the accepted rate reaches the desired 100 Hz. In order to optimize data flow, event selections are made in progressive stages by applying a series of filters. The initial decision is made on a subset of data, from detector components such as calorimeter and muon systems (Level-2). This avoids saturating system bandwidth by reading out the large volume of data from the Tracker detector. Final HLT algorithms are then applied to the complete event (Level-3) and accepted event are sent to mass storage.

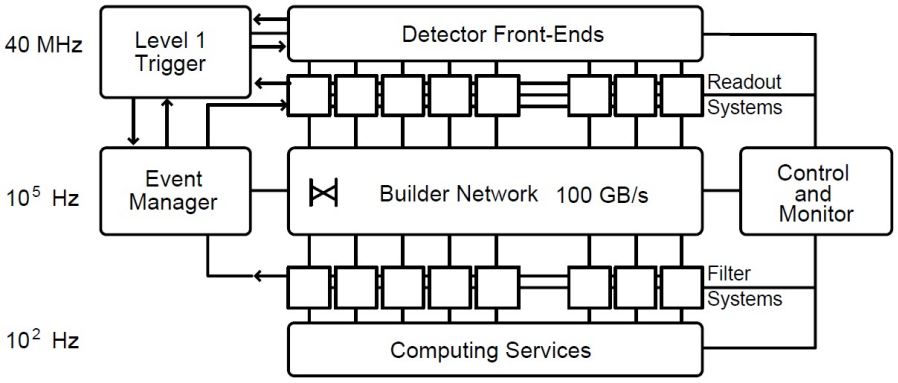

Figure 2.14: Overview of the general architecture of the CMS DAQ system.

L1 output is read by the **Data Acquisition** (DAQ) system [58], which merges event fragments from different front-end devices in a complete event, and passes events to the Event Filter Farm where HLT algorithms are performed. Figure 2.14 gives an overview of the general architecture of the CMS DAQ system. Digitized data from detector front-end electronics are stored

in the Detector Front-End modules upon reception of a L1 trigger accept signal. During the L1 trigger decision-making period, all high-resolution data are held in pipelined memories in the detector front-ends. Based on the result of the Level-1 trigger, data from the pipelined memories are transferred to front-end Readout Units (RU). The event manager coordinates the data flow in the RU builders and keeps track of the memory occupancy of the RUs. Fast access is provided by a Builder Network, capable of supplying 800 Gb/s throughput to the filter systems. The readout builder network is used to send event fragments from the RU to the builder units, where the event is defragmented, before being passed to the HLT.

At CMS, of the order of 10^8 channels have to be read out per bunch crossing and even after compacting data an event size of approximately 1 MB remains. Data from all different LHC experiments flows at a rate of around 700 MB/s, equivalent to a total amount of data of about 15×10^6 GB/year. This translates in severe requirements on analysis software, computing resources, and storage capacities, which cannot easily be accomplished by single institutions. The LHC computing Grid [59] provides a hierarchical tier structure with one Tier-0 center based at CERN and several Tier-1s and Tier-2s distributed all over the world. The CMS computing model [60] is based on these globally distributed computing and storage resources. The idea is that data will be distributed over the grid. Physicists can access them from their local institute and run their analysis directly on the hosting site. Each layer of the tier structure serves a particular computing tasks. Tier-0 collects raw collision data and performs a first reconstruction of desired physics objects at a rate of about 150 events/s. Copies are then distributed among the Tier-1 sites, where re-reconstructions due to improved or changed reconstruction algorithms are run. Calibration and alignment jobs, as well as filtering of smaller datasets matching particular needs of certain physics groups, also belong to the Tier-1 site duties. Resources of subsequent layer (Tier-2 sites) are divided between local institute members and the CMS community. They provide storage capacities for smaller group datasets and simulated MC datasets and support offline calibration and alignment tasks. The final layer of Tier-3 sites provide additional resources for local user community and are mainly used for interactive analysis and software development.

Chapter 3

Resistive Plate Chambers and Muon Trigger

Muons play a key role in the search for the Higgs boson and for new physics (e.g., $Z' \rightarrow \mu\mu$). The ability to trigger on and reconstruct muons at the highest luminosities is central to the concept of CMS. As described in chapter 2, the CMS muon system has a redundant and complementary trigger capability over nearly the entire rapidity range. A dedicated trigger element, the Resistive Plate Chamber, guarantees fast, highly segmented triggers with a sharp p_T threshold.

In the present chapter, after a brief introduction to gas detectors, the main features of RPC detector and trigger system are reviewed.

3.1 Gas Detectors

In 1908 Rutherford and Geiger, investigating the charge and nature of α-particles, devised an instrument to detect and count these particles. The instrument consisted of a tube containing gas with a wire at high voltage along the axis. Particles passing through the gas caused ionization and initiated a brief discharge. This marked the birth of gas detectors in nuclear and particle physics [61].

The base physics principle behind gas detectors may be easily summarized as follows. A particle incident on a gas volume causes excitation and ionization within it. Primary [1] electron-ion pairs act like free charges and are accelerated by an external electric field. Electrons may thus gain enough energy to cause secondary ionization and initiate a charge multiplication mechanism. Also, secondary charge avalanches can start from photons emitted in recombination events. The amount of liberated charge determines the operation mode of the detector. Figure 3.1 shows the amplification factor,

[1] The charge liberated by the ionizing particle is called primary.

or gas gain [2] as a function of the applied voltage [62]. Five regions can be isolated:

- I- Primary electron-ion pair recombine before having the time to produce secondary ionization.
- II- Ionization charge is entirely collected on the electrodes. The amplification factor remains constant even if the voltage is increased.
- III- Charge produced in the avalanche is proportional to the primary ionization and the collected charge increases strongly with applied voltage.
- IV- This is a region of limited proportionality. Once the amplification factor exceeds 10^8 the avalanche degenerates in a streamer, a plasma of ions and electrons.
- V- Streamers eventually connect the electrodes producing a visible spark. Geiger-Müller counters and spark chambers work in these conditions.

At higher voltages, discharges appear even in absence of ionizing particles. This may cause detector damage.

Studying charge multiplication mechanisms in gases, Geiger and his collaborators developed a cylindrical proportional counter to detect α-particles. They immediately realized radial symmetry imposed sever limitations on time resolution, typically of the order of microseconds. In fact, in a cylindrical detector the electric field is non-uniform resulting in fluctuations in electron drift time. Primary electrons, produced at different position in the gas volume, must drift for a finite distance towards the cathode where the field is intense enough to trigger charge multiplication processes. Wavering in electron drift time introduces significant uncertainties on the detection time of incident particles.

Better time resolution can be obtained by using planar geometry and uniform electric fields. With plane electrodes, the amplification region is extended to the whole gas gap. Thus the uncertainty due to electron drift is significantly reduced. First studies on gas detector with planar and parallel electrodes were performed by Keuffel in the late '40s [63]. The Parallel Plate Counter (PPC) designed by Keuffel had 35 cm^2 circular copper electrodes separated by 2.5 mm of an argon - xylene ($C_6H_4(CH_3)_2$) based gas mixture at 500 bar. A voltage difference of 1 - 3 kV insured the formation of a spark at the passage of a ionizing particle. To extinguish the spark a external circuit switched off the voltage for 0.01 - 0.05 s. Such mechanism improved detector rate capabilities.

[2] The amplification factor, also called gas gain, is the ratio between the total charge produced in the avalanche and the primary ionization charge.

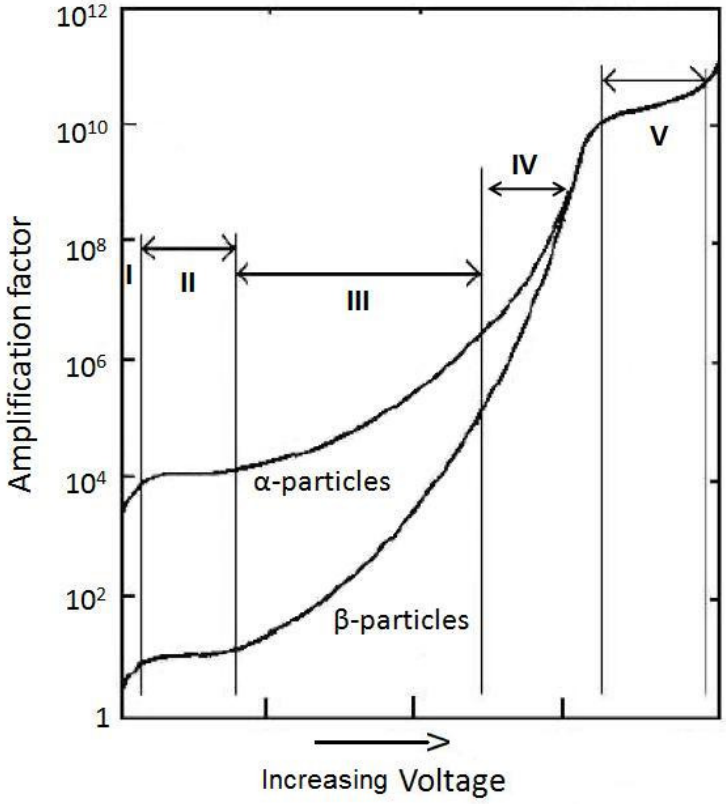

Figure 3.1: Amplification factor versus high voltage.

After this first prototype, numerous detectors with planar and parallel electrodes were developed [64, 65], differing in design, materials, and operation mode. A turning-point was reached in the late '70s when resistive electrodes were introduce in place of the conductive ones used until then. The movement of charge in the gas gap induces a voltage drop between the electrodes. The intensity of the electric field falls beneath the minimum threshold to initiate charge multiplication mechanisms and the avalanche, streamer, or spark stops. This principle was used by Petrov in the design of the Planar Spark Chamber [66], which had a single resistive glass electrode, and by Santonico, in the early '80s, for the realization of Resistive Plate Chambers [67, 68].

3.2 Resistive Plate Chambers

In the last 30 years Resistive Plate Chambers (RPC) have been chosen for many cosmic-ray and accelerator-based high energy physics experiments. The main characteristics that make RPC so appealing are: high gain, good time and spatial resolution, simple design, and low cost. Schematically (figure 3.2), RPCs are made by two resistive electrodes with a conductive coating, like graphite. Electrodes are generally made from phenolic resins, like bakelite, with a bulk resistivity of $\rho = 10^{10-12}$ Ωcm. For electrical and mechanical stability, these electrodes are mounted on rectangular plastic frames and kept at constant distance from each other by means of small plastic separators. The gap between the electrodes is fluxed with a gas mixture usually containing an organic gas with high UV absorption capability to reduce secondary avalanches and a strongly electronegative gas to control charge multiplication (see section 3.3). A voltage difference is placed across the electrode. When a ionizing particle crosses the active volume, free charges are accelerated by the external field and start an avalanche. Signal pick-up is realized by conductive strips, usually aluminum or copper, laying on top of the graphite coating and insulated by a mylar foil [3].

Traditionally, RPCs have been operated in streamer mode, i.e. the electric field inside the gap was kept intense enough to generate limited discharges. With this configuration, charge developed within the gas gap at the passage of a ionizing particle is $\sim$100 pC. The use of resistive electrodes and a well thought gas mixture [4] limited the region interested in the discharge to an area of $\sim$ 0.1 cm^2. Thus the detector could withstand an incident flux of about 100 Hz/cm^2 (assuming a dead time of the order milliseconds).

[3] Mylar is the trade name for films made from stretched polyethylene terephthalate (PET)

[4] The gas mixture used in an RPC operated in streamer mode contains a nobile gas as active element, a hydrocarbon gas with high UV absorption capability to reduce secondary avalanches, and a gas with high electronegativity such as Freon to control charge multiplication.

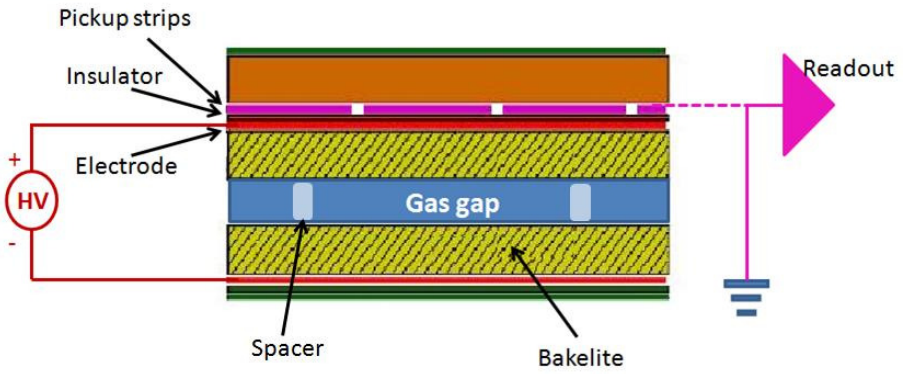

Figure 3.2: Schematic representation of a Resistive Plate Chamber.

This mode of operation is suitable for low-rate experiments and therefore inadequate for LHC environment. To increase rate capability, a possibility is to work in avalanche mode, i.e. keep the gas gain factor lower than 10^8. In this case the avalanche grows to a maximum of $\sim$ 25 pC allowing a incident rate of the order kHz [69], but requiring robust signal amplification electronics. The substantial reduction of charge produced improves the rate capability by more than an order of magnitude, allowing the application of RPCs in experiments such as CMS at LHC.

3.3 Avalanche Growth and Signal Formation in RPCs

When a relativistic particle goes through matter, in particular a gas, it loses energy by interacting with the medium's molecules. This energy loss is regulated by the well known Bethe-Bloch [70] formula:

$$-\frac{dE}{dx} = \frac{4\pi N_A}{m_e c^2}\rho\frac{Zz^2}{A\beta^2}\left[\ln(\frac{2m_e\gamma^2c^2\beta^2}{\bar{I}}) - \beta^2 - \frac{\delta}{2} - \frac{C}{Z}\right], \qquad (3.1)$$

where

- N_A is the number of Avogadro and m_e is the electron's mass;
- ρ, Z, A are the density, the atomic number and mass of the medium respectively;
- z is the charge and βc is the velocity of the incident particle;
- $\bar{I}$ is the ionization potential of the medium. Its value is determined experimentally;

- the term $-\delta/2$ takes in account polarization effects in the medium;
- while $-C/Z$ accounts for the inner electrons screening effect.

The energy lost causes excitation and ionization of the medium. A relativistic particle produces an average of 100 electron-ion pairs in 1 cm of gas at normal conditions, too few for an useful electrical signal [71]. Instead, if an external electrical field is applied, liberated charges are accelerated and may yield secondary ionization. An external electric field $\mathbf{E}$ transmits an overall motion to the free charges, that move along the field's direction with a drift velocity $v_d = \mu\mathbf{E}/p$. p is the gas pressure and μ is a coefficient that takes the name of *mobility*. Electrons have ∼100 times higher mobility than ions.

When the external field is large enough (∼kV/cm) a significant number of primary electrons, accelerated towards the anode, gains enough energy to produce secondary ionization, so starting an avalanche. Drift velocity of positive ions is about 100 time smaller than that of electrons (typically of the order of 10^4 cm/s). This gives a drop-like shape to the charge distribution. Figure 3.3 is a schematic illustration of an avalanche profile. The avalanche continues to grow until the field due to the spacial charge, $\mathbf{E}_s$, is comparable with the external field. At this point, ion-electron recombination probability increases, with subsequent photon production. These photons start secondary avalanches, mainly along the axis of the primary avalanche where the field is stronger ($\mathbf{E}_{total}$=$\mathbf{E}$+$\mathbf{E}_s$). The avalanche degenerates into a streamer, a plasma of ions and electrons, which eventually connects the electrodes producing a visible spark.

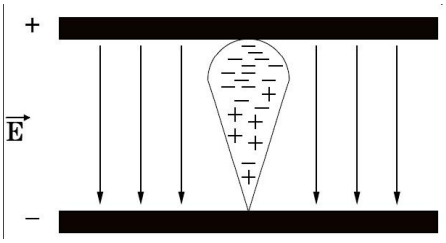

Figure 3.3: Schematic illustration of an avalanche formation in a gaseous detector.

Let us now consider the passage of an ionizing particle specifically in an RPC detector (sketched in fig. 3.4) and let us suppose it interacts with the gas at x_0 producing a *cluster* of n_0 ion-electron pairs. The average behavior of the avalanche growth in a gas mixture is ruled by the first Townsend coefficient α [72], defined as the average number of ionizations per unit length, or the inverse of the free mean path, and by the attachment coefficient β, i.e. the average number of electrons captured per unit length.

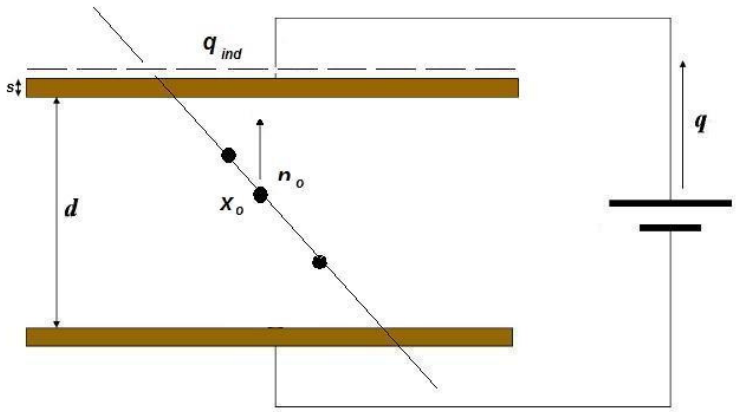

Figure 3.4: Charge formation in a planar resistive gas detector.

The average number of free electrons (dn_e) in an interval dx can be written as [73]

$$dn_e = n_e(\alpha - \beta)dx = n_e\eta dx. \tag{3.2}$$

η is the effective ionizing coefficient and does not depend on x since the electric field in the gas gap is uniform. Integrating this equation in the interval $[x_0, x]$, one easily obtains the total number of electrons produced and the total developed charge:

$$n_e(x) = n_0 e^{\eta(x-x_0)} \Rightarrow q_e(x) = q_{ele} n_0 e^{\eta(x-x_0)}, \tag{3.3}$$

where q_{ele} stands for the electrons charge. The factor $M = e^{\eta(x-x_0)}$ is the gas gain. When M exceeds the phenomenological limit of $\sim 5 \times 10^8$ ($\eta x \sim 20$), known as the Raether condition, streamer mode is set on.

Up to this point, only a single cluster has been considered. However the incident particle may likely have multiple interactions in the gas, so to produce $n_{cl} \geq 1$ clusters. Equations 3.3 may be rewritten as:

$$n_e(x) = \sum_{j=1}^{n_{cl}} n_{0j} e^{\eta(x-x_{0j})} \tag{3.4}$$

$$q_e(x) = q_{ele} \sum_{j=1}^{n_{cl}} n_{0j} e^{\eta(x-x_{0j})}. \tag{3.5}$$

For a better understanding of avalanche formation in a gas volume, fluctuation of the above variable must be included. The number of primary clusters, initial cluster position, and gas gain are random processes governed by probability density functions. Number and size of primary clusters follow a Poisson distribution while the gas gain fluctuation has a more complicated description. A common approach is to use a Polya probability distribution for the total number of free electrons at a given point and simply rewrite equation 3.5 as [74]:

$$q_e(x) = q_{ele} \sum_{j=0}^{N} n_{0j} F_j e^{\eta(x-x_{0j})}. \tag{3.6}$$

The factors F_j are extracted from the Ploya distribution.

Charge movement in the gas gap induces a signal on external pick-up strips. The fast component of this current, which constitutes the useful signal, is due to electron drift. Magnitude of the current can be calculated from:

$$i(t) = q_e(x) E_w v_d, \tag{3.7}$$

where E_w is the normalized weighted field as calculated by Radeka [75]. E_w can be experimentally measured by applying a unitary voltage to one pick-up electrode and putting the others to zero. Theoretically it can be evaluated by using the electrical model of an RPC chambers. Assuming that the signal formation time is much smaller than any circuit time constant, we can neglect the effect of neighboring regions and consider only the volume, or *cell*, interested by the avalanche. The electronic equivalent of an RPC cell is shown in figure 3.5. C_g and C_b represent respectively equivalent capacitors of the gas gap and of the bakelite. If d is the gap width, s the bakelite thickness, ρ its resistivity and ϵ_r its relative dielectric constant, then:

$$C_g = \epsilon_0 \frac{S}{d}, C_b = \epsilon_r \epsilon_0 \frac{S}{s}, \tag{3.8}$$

where S is the bakelite area affected by the avalanche. Bakelite resistance, instead, is given by

$$R_b = \rho \frac{s}{S}. \tag{3.9}$$

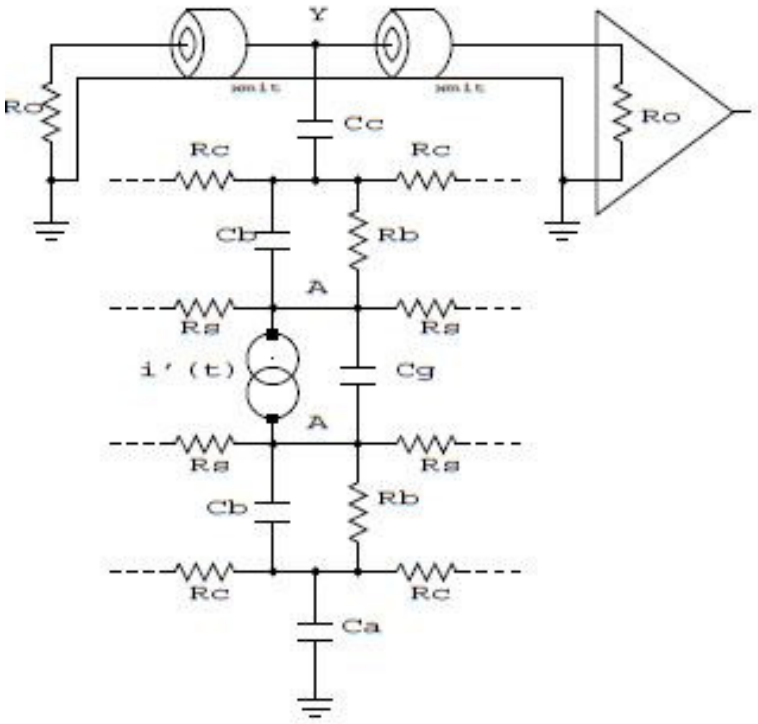

Figure 3.5: Electronic equivalent of an RPC cell.

R_c is the graphite layer resistance ($\sim$ 100 k$\Omega/\Box$) and R_s is the bakelite surface resistance. The coaxial cables represent pick-up electrodes, which act like transmission lines terminated by resistances R_o; C_a, C_c are coupling parasitic capacitances and their value is typically $\gg C_g$.

Finally, the weighted field E_w is simply:

$$E_w = - \bigtriangledown V_g = k/d, \tag{3.10}$$

where V_g is the potential function in C_g. The factor k takes in account geometrical factors and is given by [76]:

$$k = \frac{C_b}{C_b + C_g} = \frac{\epsilon_r \frac{d}{s}}{\epsilon \frac{d}{s} + 2}, \tag{3.11}$$

RPCs at CMS (see section 3.4) are made of two single 2 mm gaps. Signals are extracted from a plane of pick-up strips located between the gaps (common mode readout). Electrode width is $d = 2$ mm and $\epsilon_r \sim 5$. Therefore, each single gap must be reduced by the factor $k \sim 0.7$ and the total induced signal is the sum of the two [5].

Equations 3.10 and 3.6 can be used to rewrite equation 3.7 as:

$$i = v_d q_{ele} \frac{k}{d} \sum_{j=0}^{N} n_{0j} F_j [e^{\eta(d - x_{0j})} - 1]. \tag{3.12}$$

After the passage of a ionizing particle, current in the gas gap discharges the capacitor C_g and all the voltage difference is moved on C_b. The external field is momentarily switched off. The time needed for the interested area S to recover and be ready for yet another incident particle is simply:

$$\tau = R_b \left(C_g + 2C_b \right) = \rho \varepsilon_0 \left(\varepsilon_r + 2 \frac{s}{d} \right), \tag{3.13}$$

where ε_r is the bakelite's dielectric constant. For RPCs at CMS, ρ is of the order of 10^{10} Ωcm, ε_r $\sim$5, $\frac{s}{d} \sim 1$ mm, therefore τ is about 31 ms. This is a much bigger value compared to the duration of the discharge (few nanoseconds). So the electrodes act as isolators and the avalanche growth is interrupted.

[5] If the pick-up strips were put externally and not in common mode readout, k would be given by: $k(n_g) = \frac{C_b}{n_g C_b + (n_g + 1) C_g}$, where n_g is equal to the number of gaps.

3.4 RPCs at CMS

RPC chambers [77] at the CMS detector are made by parallel resistive plates of phenolic resin (bakelite) treated with linseed oil [78] and separated by a gas gap of a few millimeters. Mechanical stability is insured by mounting the electrodes on a rigid plastic frame and by using Poly-Vinyl Chloride (PVC) spacers to keep width constant throughout the gap. The plates are coated on the outer surface with graphite paint to form HV and ground electrodes. Read-out is performed by means of conductive strips separated from the graphite coating by an insulating Poly-Ethylene Terephthalate (PET) film. A higher rate capability compared to traditional RPCs is achieved by operating in avalanche mode rather than streamer mode: the electric field and consequently the gas multiplication is reduced requiring an improved electronic signal amplification. In order to increase the signal on the read-out strips, a double-gap design is used in CMS, with two (figure 3.6) gas gaps of 2 mm width being read out by one set of strips in the middle. The RPCs are operated at 9.3 - 9.5 kV with a gas mixture of 95% $C_2H_2F_4$ and 5% i-C_4H_{10}. A rate capability of 1 kHz/cm^2 can be achieved.

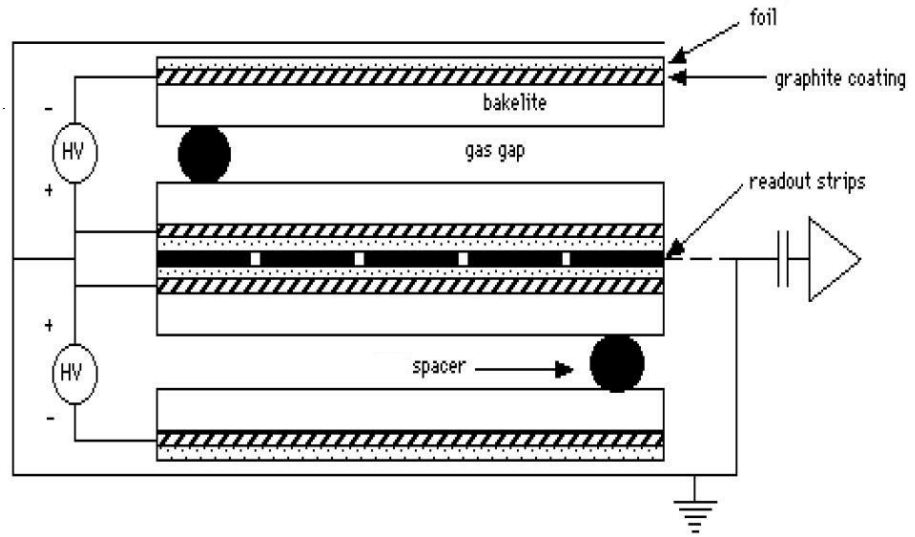

Figure 3.6: Schematic layout of the double gap RPCs.

3.4.1 Conditions and Requirements

RPCs should fulfill some basic requirements [55]: good timing, low cluster size (i.e. the number of contiguous strips which give signals at the crossing of an ionizing particle), and good rate capability, high intrinsic efficiency, and withstand long term operation in high background conditions.

RPC Layer	Strip Pitch (cm)	Average Cluster size
$RB1_{in}$	2.3	1.52
$RB1_{out}$	2.5	1.46
$RB2_{in}$	2.8	1.41
$RB2_{out}$	3.0	1.38
RB3	3.5	1.31
RB4	4.1	1.25

Table 3.1: Strip pitch and average cluster size estimated considering only cosmic muons pointing to the nominal interaction point (operating voltage = 9.2 kV - electronic threshold = 230 mV).

Good time performance is crucial for triggering with high efficiency. The trigger must identify muon candidates within a 25 ns window. This requires a time resolution of only a few nanoseconds.

Cluster size should be small ($\lesssim 2$) in order to achieve the required momentum resolution and minimize the number of possible ghost-hit associations. Results obtained for the barrel only in a month-long data-taking exercise, known as the Cosmic Run At Four Tesla (CRAFT), between October and November 2008 are summarized in table 3.1

Finally, rate capability is required to reach 1 kHz/cm^2 with a detector efficiency of $\epsilon > 95\%$. In fact, background hit rate is comparable to incident muon rate in high η regions. Therefore, 1 kHz/cm^2 is a reasonably safe estimate of the highest rate at which the RPCs are expected to operate.

Detector and trigger performance studies are the main topic of this thesis. Results obtained using the RPC Data Quality Monitoring system (see chapter 4) with both cosmic and early LHC collision data are given in chapter 5. In this section only relevant detector parameters and material specifications are reviewed.

Electrode Resistivity

Electrode bulk resistivity ρ strongly influences detector rate capabilities. Two main effects may be identified: the time constant $\tau \propto \rho$ of the RPC region involved in an avalanche process decreases with ρ, as seen in section 3.3; moreover, at very high rates, the current flowing through the bakelite plates becomes important and produces a non-negligible voltage drop, V_d, across them [79]. This second effect translates in a lower effective voltage applied to the gas gap and a lower gas amplification. V_d can be estimated as:

$$\mathrm{V_d} = 2 \langle \mathrm{q_e} \rangle \, \mathrm{rs}\rho, \tag{3.14}$$

where r is the rate and s is the electrode thickness. Assuming $\langle q_e \rangle$=25 pC and r = 10^3 Hz/cm^2, a value of $\rho \sim 10^{10}$ Ωcm should be used to limit V_d to few tens of volts. A larger voltage drop would reduce rate capability and influence the pulse delay due to changes in drift velocity, which decreases with the effective voltage. This value of ρ yields $\tau \sim 31$ ms.

Gas Mixture

For a given ηd, gas cluster density λ should be as large as possible, to maximize the useful signal and achieve high efficiency. Usual gas mixtures employed in RPCs have values of λ contained between 2 and 8 clusters/mm. Lower values would give rise to high inefficiency, due to lack of primary pairs.

Total RPC gas volume, at CMS, is 10 m^3 for the barrel and 6 m^3 for both endcaps. All chambers operate on a non-flammable gas mixture of 96.2% $C_2H_2F_4$ (freon), 3.5% i-C_4H_{10}, and 0.3% SF_6 [81]. For this variety of freon [82] $\lambda \sim 5$. The effective ionizing coefficient, η, is ~ 18. Freon acts as a strong quencher on the discharge, keeping the detector in avalanche mode. Isobutane instead is used to absorb photons and reduce the region interested by the discharge. Finally, it has been seen that a very small percentage of SF_6 added to a binary mixture ($C_2H_2F_4$, i-C_4H_{10}) suppresses streamer probability. A percentage of SF_6 equal to 0.3% is enough to widen the operating plateau of almost 200 V [83].

Gas gain and streamer probability in CMS are constantly monitored by the Gas Gain Monitoring system (GGM) [84]. RPC operating plateau is defined as the range in the operating voltage where chamber efficiency is $> 90\%$ and streamer probability is $< 10\%$. Figure 3.7 shows efficiency and streamer curves as a function of the effective high voltage, V_{eff}. V_{eff} is a function of the environmental pressure (P) and temperature (T) as:

$$V_{eff} = V_{nominal} \frac{T}{P} \frac{P_0}{T_0}, \tag{3.15}$$

where P_0 and T_0 are reference pressure and temperature values respectively [85]. For values of V_{eff} up to 9.9 kV clean avalanche mode is observed, while at $V_{eff} = 10.7$ kV streamer contribution becomes relevant ($> 10\%$). For $V_{eff} = 11$ kV and higher discharges occur even without the presence of trigger. Both efficiency and avalanche plateau are in good agreement with previous results [86].

Gap Width

Gap width influences detector time resolution. Figure 3.8 shows the simulated achievable time resolution as a function of the gap width. Also the full width at the base (FWAB), defined as the time interval containing 95%

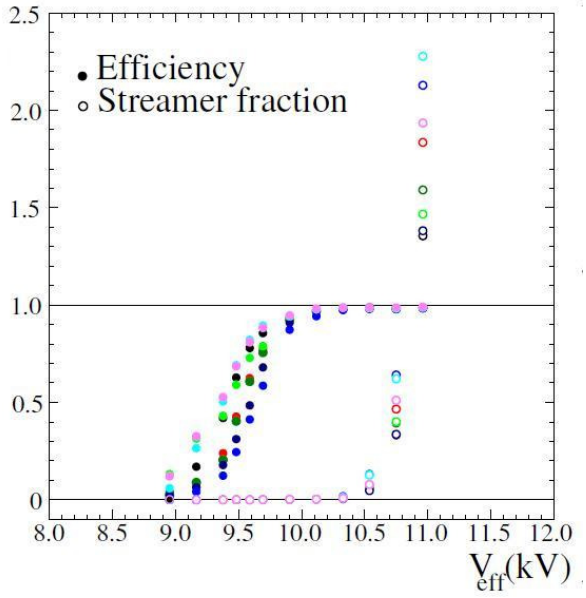

Figure 3.7: Efficiency and streamer curves as a function of the effective high voltage V_{eff}. Eight chambers (corresponding to the eight colors in the plot) have been used for the study. Each point corresponds to a total of 10000 entries. [84]

of the events, is given. The performance, as expected, becomes poorer at wider gaps, due to the larger fluctuations present during the avalanche development. Unfortunately, in narrow gas gaps total charge collected at the electrodes is lower compared to wider gaps and stronger signal amplification is needed. A 2 mm gap width seems best compromise.

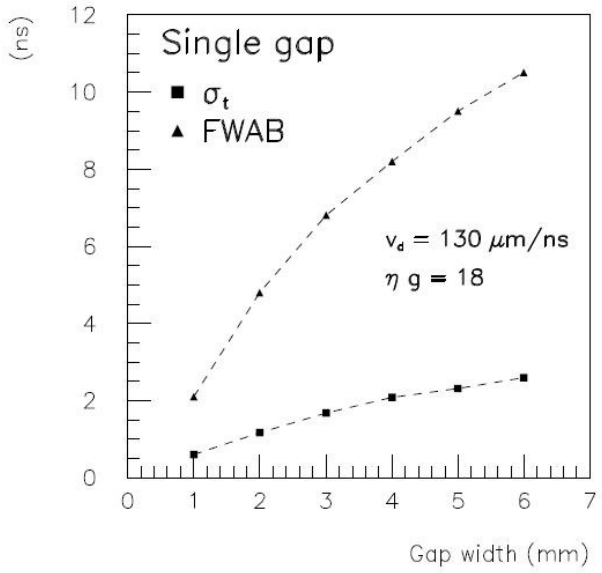

Figure 3.8: Simulated time resolution as a function of the gap width [55]. The full width at base (FWAB), that is the time interval containing 95% of the events, is also given.

Pick-up Strips

At CMS, charged particle tracks are bent in the r-ϕ plane, perpendicular to the beam line. Therefore, muon tracks must be measured in such plane with high granularity to insure good transverse momentum resolution. Precise determination of the η coordinates is not required. Above requirements define layout and segmentation of the RPC chambers and strips [87, 88].

Nominal strip angular width is to be $\frac{5}{16}°$ in the r-ϕ plane. Barrel chamber strips run parallelly to the z-axis with 2.2 - 4.1 cm pitch. Endcap strips are radially arranged and are trapezoidal in shape. All endcap roll count 32 strip (96 strips per chamber), while barrel, due to geometrical constrains rolls have a number of strips that varies among 36, 42, 48, 60, 84, and 90.

Good timing is crucial for triggering with high efficiency. Muon identification within a 25 ns window requires not only a few nanoseconds resolution, but also that the tails of the signal time distribution stay within the window. This implies that the time walk due to the propagation of the signals

along the strips should be kept within 4 - 5 ns. Assuming signal propagation velocity is $\frac{2}{3}$c, a maximum strip length of about 1 m is allowed. In CMS, long strips, raging from 80 - 100 cm, are used in the barrel region where rate effects are negligible. Instead, in the endcap, where the rate problem is more severe, strips are only 25 to 80 cm long.

Double Gap

CMS RPCs use a double-gap configuration, shown in figure 3.9. Two single gaps are mechanically coupled and signals are extracted from a plane of strips located in the middle. This allows to operate each single gap at lower gas gain with an effective efficiency that is the OR of the two single gap efficiencies. It also maximizes the induced signal which is the analogue sum of the two independent signals developed in each chamber. Figure 3.10 shows the simulated and experimental charge spectra for both single and double gap configurations. Figure 3.10 shows that higher thresholds can

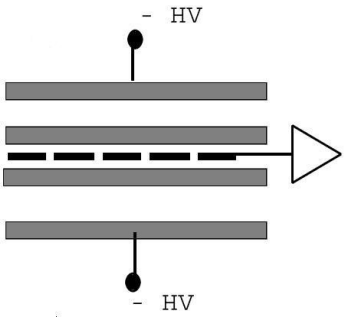

Figure 3.9: Simplified layout of the double gap RPCs.

be used without loss of efficiency.

Also the time resolution is believed to improve, as it can be seen in figure 3.11. A lower limit of 1.4 ns can be achieved; electronic noise and local field variation must be considered for the real experimental time resolution.

3.5 The Muon Trigger

The CMS Trigger system has been already presented in section 2.2.5 and a detailed description can be found in [89]. In the following, only the main features of the Muon Trigger system are reported. Particular attention is given to the RPC Trigger.

3.5.1 Requirements

Goal of the L1 Muon Trigger [90] is to identify high-p_T muons with high efficiency, reconstruct their position and transverse momentum, and

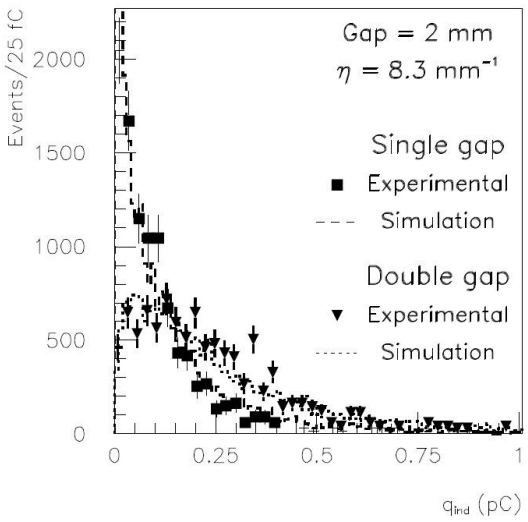

Figure 3.10: Simulated and experimental charge spectra for single and double gap RPCs [55].

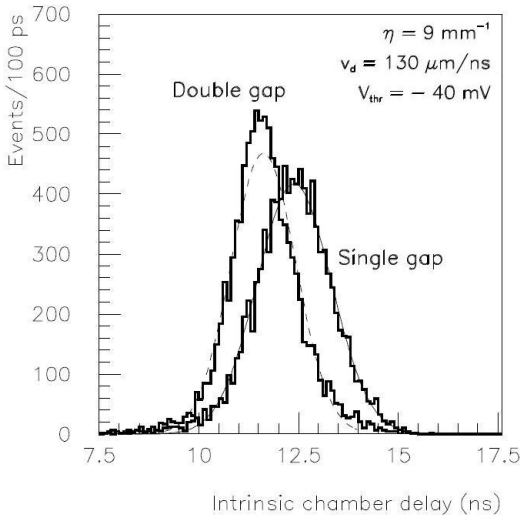

Figure 3.11: Simulated time distributions for single and double gap RPCs [55].

provide unambiguous bunch crossing assignment. High-p_T muons are in fact a signature of many interesting physics processes CMS hopes to observe. Important examples are:

- Standard Model Higgs: H $\rightarrow$ ZZ$^{(*)}$ $\rightarrow$ 4leptons (including 2 or 4 μ), m$_H$ = 130 -759 GeV/c^2
- Supersymmetric Higgs: h, H, A $\rightarrow \mu^+\mu^-$
- Supersymmetric particles: $\widetilde{q}, \widetilde{g} \rightarrow$ multi-lepton + multi-jet +E$_T^{miss}$
- Heavy neutral gauge bosons from theories beyond the Standard Model: Z' $\rightarrow \mu^+\mu^-$.

Expected event rates from the above processes are fractions of hertz. Therefore, selecting interesting events from the copious background of *prompt* muons from bottom, charm, and W/Z decays and *non-prompt* muons from pion, kaon decays is a difficult task. Generator-level inclusive integral rate of single muon triggers within the geometrical acceptance ($|\eta| < 2.1$) at $\mathcal{L}$ = 10^{34} cm$^{-2}s^{-1}$ is shown in fig. 3.12. Without any p_T cut, the integrated rate of events with at least one muon is about 10^6 H, much higher than the maximum acceptable rate (see section 2.2.5). To reduce the rate, cuts

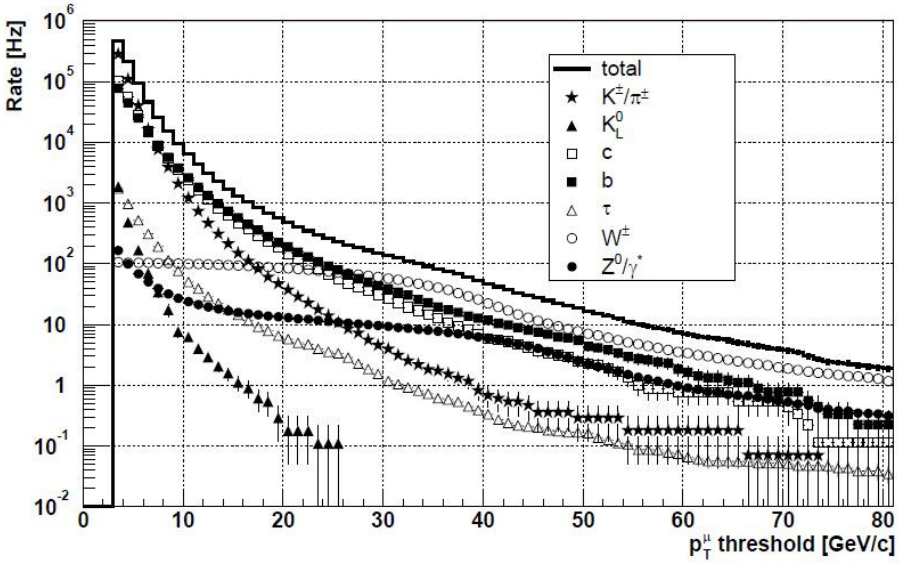

Figure 3.12: Inclusive integral rate of single muon triggers within the geometrical acceptance ($|\eta| < 2.1$) at $\mathcal{L}$ = 10^{34} cm$^{-2}s^{-1}$. Breakdown of the rate in different muon sources is also shown [91].

on muon p_T are applied. A precise measurement of muon transverse momentum is therefore essential. Furthermore, since muons kaons, pions, and

heavy quarks are produced inside jets, isolation criteria based on energy deposits in the calorimeters can help to reduced the background. Thus the muon trigger must accept information from the calorimeter trigger.

Another stratagem, used to increase trigger selection efficiency of potentially interesting events and reject background, is to search for multi-muon events. Firstly, this implies the ability to process information from more than one muon, even at low p_T. Secondly, excellent ghost events suppressed is required. Upper limit for tolerable ghosting probability is 0.5% [90].

3.5.2 Architecture

All three muon detectors (DT, CSC, and RPC) contribute to the Level-1 (L1) Muon Trigger, which benefits from their complementary features. DTs, with long drift time ($\sim$ 400 ns), and CSCs, with charge weighting, are more vulnerable to muon radiation for which RPC are much less sensitive. Excellent spatial precision of DTs [92] and CSCs [93] ensures sharp momentum thresholds. RPCs, on the other hand, have a superior timing resolution and allow precise beam crossing identification. In the DT/CSC case, a background hit or track segment can eliminate the right one and cause some inefficiency. The opposite is true in the RPC Trigger for all hits are processed simultaneously. This may lead to some rate increase. Accidental coincidence of three of four background hits can be recognized by the RPC Trigger as a real muon. This is very unlikely for DT/CSC as they look for coincidence of several planes in each station. Properly combining the information from both systems results in high efficiency and powerful background rejection. Another important advantage of the two component system is the possibility of crosschecks and cross calibration. Trigger data from the two components collected by the DAQ can be compared online. This enables quick discovery of possible problems and allows to take immediate action.

DT, CSC, and RPC Trigger systems identify muon candidates separately using different algorithms based on different detector technologies. Figure 3.13 is a schematic representation of the L1 Muon Trigger and the functional relations between its components. In DT and CSC Triggers, local track segments are reconstructed in the muon stations and then combined to tracks in the Track Finders. The RPC Trigger, on the other hand, uses PAttern Comparator methods (PAC) [94]. Hits are collected by the PAC Trigger, which looks for space and time correlation. Hits are matched with predefined patterns using a large look-up table to provide identification and estimate of p_T. Data are exchanged between DT and CSC in the overlap region ($0.8 < |\eta| < 1.2$). In this way the Barrel Track Finder covers $|\eta| < 1.0$, whereas the Endcap Track Finder covers $1.0 < |\eta| < 2.4$. Optionally, coarse RPC data can be sent to the CSC Trigger in order to help solve spatial and temporal ambiguities in multi-muon events. The RPC trigger works on a grid of $\Delta\eta \times \Delta\phi = 0.1 \times 2.5°$, which determines its two muon resolutions.

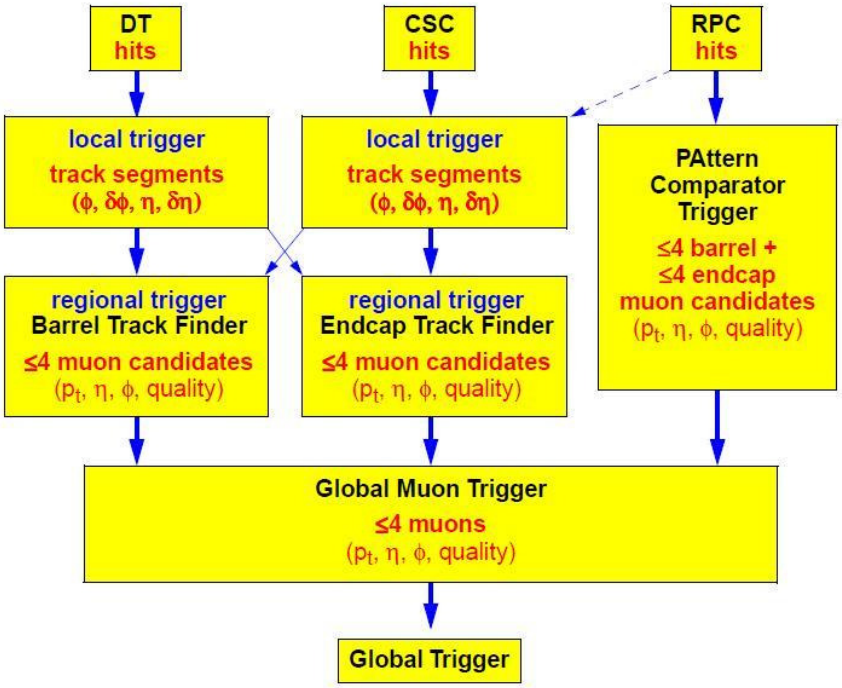

Figure 3.13: Schematic representation of the L1 Muon Trigger and the functional relations between its components.

DT and CSC triggers do not work on a fixed grid. η and ϕ coordinates are calculated with precision of 0.05 and 2.5° respectively.

Combining information from the different systems and from the calorimeters is carried out by the Global Muon Trigger (GMT). The GMT receives, at every bunch crossing, up to four muon candidates each from the DT and RPC Triggers, in the barrel, and up to four muon candidates each from the CSC and RPC Triggers, in the forward region. Candidates consist of measurements of transverse momentum (p_T), sign of charge, azimuthal angle (ϕ) and pseudorapidity (η), as well as a quality code. From the Global Calorimeter Trigger the GMT receives MIP and quiet bits for each of the 252 calorimeter regions measuring $\Delta\eta \times \Delta\phi = 0.35 \times 0.35$ rad. MIP bits denote compatibility of energy deposits in the calorimeters with the passage of a Minimum Ionizing Particle. Quiet bits indicate that the energy deposit in the region was below a certain threshold and are used for isolation studies.

Muon candidate matching is done in the GMT by comparing temporal and spacial coordinates (η, ϕ). Candidates are accepted if they are reconstructed by at least two systems, otherwise they are selected on the basis of their quality information. Low quality candidates from problematic η regions are discarded. If two candidates are matched, track parameters are chosen according to a programmable logic. The best four muon candidates are forwarded to the Global Trigger (GT) for further processing.

Redundancy of the muon system, together with the advanced GMT algorithms, assures better efficiency and purity in muons identification, and allows to fulfill the physic requirements. Performance results of the Muon Trigger are illustrated in figure 3.14, where the output rates of the single- and di-muon triggers are presented. Additionally, single muon efficiency on a sample of $W \rightarrow \mu\nu$ generate in the fiducial volume $|\eta| < 2.4$ with $p_T > 10$ GeV/c is 83%. The combined efficiency of single- and di- muon criteria on a $Z \rightarrow \mu\mu$ sample is 99%.

RPC Trigger

The RPC Pattern Comparator Trigger (PACT) is based on the spatial and temporal coincidence of hits in RPCs lying on the possible path of a muon coming from the interaction point. Such coincidences of hits are called *hit patterns* or *candidate tracks*. Due to energy loss fluctuations and multiple scattering, there are many possible hit patterns in the RPC muon stations for a muon track of definitive transverse momentum emitted in a certain direction. Therefore, the PACT should recognize many spatial patterns of hits for a given transverse momentum muon. Patterns allow to identify muons with at least four hits on six RPC layers in the barrel and three out of four in the endcaps (presently, the fourth RPC endcap stations are staged). Figure 3.15 illustrates pattern finding algorithms in the r - ϕ plane. A ghost suppression algorithm is applied to reduce the effect of accidental coincidences due to background hits.

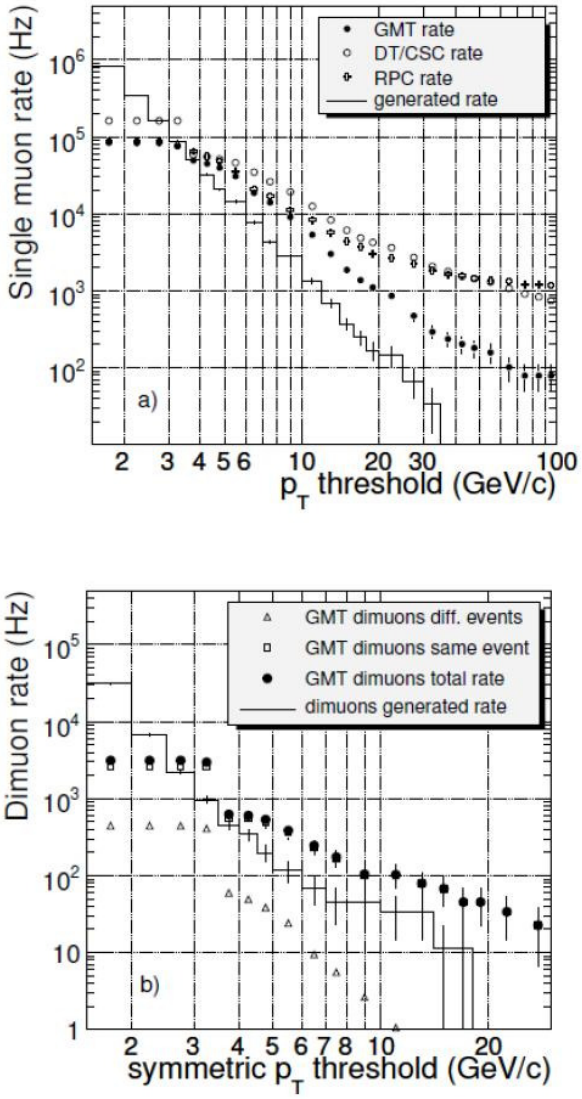

Figure 3.14: Level-1 trigger rate at $\mathcal{L} = 2 \times 10^{33}$ cm^{-2}s^{-1} as a function of pT threshold for single- (top) and di-muon trigger (bottom), at generator level (histogram) and from the Global Muon Trigger (dark circles with error bars). The single-muon rate plot also shows trigger rates that would occur if the RPC system or the combined DT/CSC system were operated standalone (crosses and open circles). The di-muon rate plot shows separately the contributions from the same (squares) and different (triangles) p-p collisions within one BX [3].

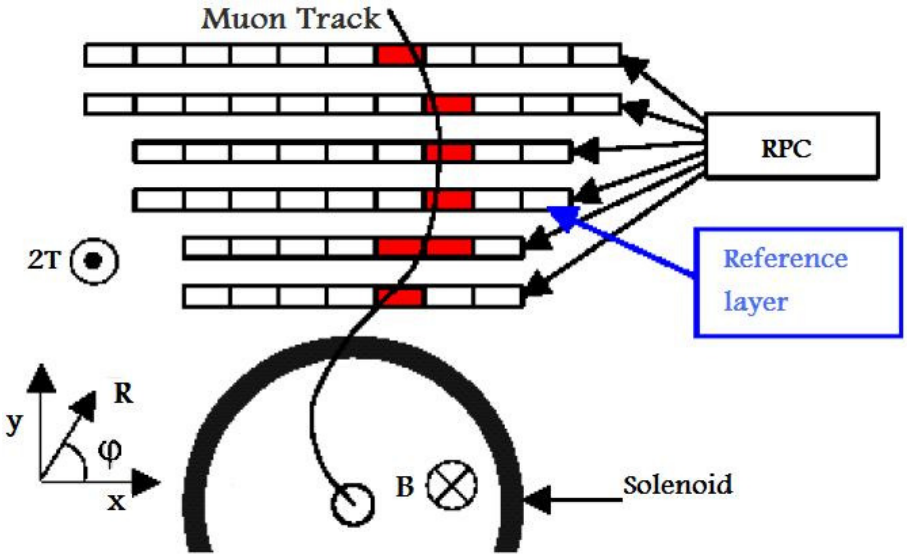

Figure 3.15: Schematic illustration of the RPC Pattern Comparator Trigger (PACT).

Tens of thousand of patterns are needed for the whole RPC system and were obtained from Monte Carlo simulations. Trigger electronics are based on Field Programmable Gate Array (FPGA) technology [98], which allows comparison of hits with all implemented patterns concurrently. This is the only viable solution, as only a few bunch crossings ($\sim$ 25 ns) can be devoted to this task. Patter shape (i.e. bending of the corresponding muon track) defines the transverse momentum of the muon and its sign. Because of energy loss fluctuations and multiple scattering there are many possible hit patterns for a muon track of definitive p_T emitted in a certain direction. Predefined patterns of hits have to be mutually exclusive with a unique transverse momentum assignment. Patterns are divided into classes with a sign and a code denoting the transverse momentum in the range 0 - 140 GeV ($p_T Code$ = 0, 1 ... 31) assigned to each of them. The four highest p_T muon candidates in the barrel and four from the endcaps combined are then sent to the GMT.

The segmentation of the RPC Muon Trigger in pseudorapidity is shown in figure 3.16. There are 33 *trigger towers* in η, each of them is subdivided in the azimuth angle ϕ into 144 logical units, called *segments*, corresponding to about 8 consecutive strips in the second muon station or $\Delta\phi = 2.5^\circ$.

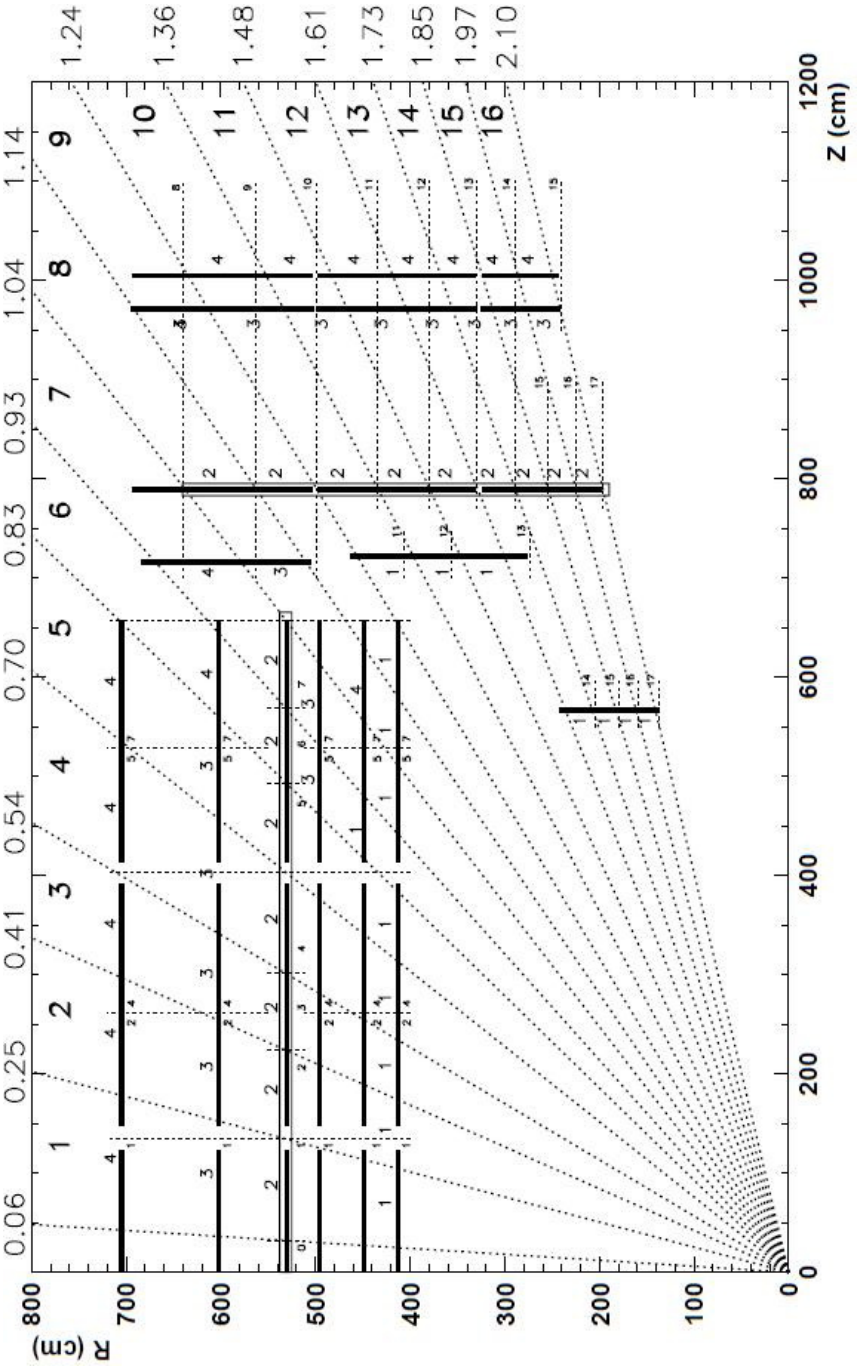

Figure 3.16: Segmentation of the RPC trigger into η-towers.

Chapter 4

Data Quality Monitoring

The RPC subdetector at CMS is a complex and massive system. About 110 000 electronic channel must be readout and data must be processed at a rate of 40 MHz. The critical tasks of monitoring detector and trigger performance, debugging hardware, and certifying recorded data are carried out by the Data Quality Monitoring (DQM) system. The CMS DQM framework provides tools for creation, filling, storage, and visualization of histograms and scalar elements. It also offers standardized algorithms for performing statistical tests and automated data certification. Within this framework, the RPC DQM system was developed. The latter is composed by a set of user defined algorithms and is intended to be used both online, during data taking, and offline, during reconstruction and re-reconstruction stages. Data monitoring applications may also be used in private analysis code. Run by run, the system measures detector level and physics quantities which are subsequently stored in a dedicated database. Here the structure, functionalities, and performance of the DQM applications for the CMS RPC detector are described.

4.1 DQM Architecture

Primary goal of the CMS Data Quality Monitoring (DQM) system [99] is to guarantee high quality physics data. To this end, it provides a homogeneous environment across various subdetector and trigger monitoring applications. The DQM infrastructure provides tools for creation, filling, storage, and visualization of histograms and scalar elements. 1D-, 2D-, and 3D-histograms, 1D- and 2D-profiles, integers, floats, and string messages can be booked, filled, and updated anywhere in the analysis code. The infrastructure also offers functionalities to perform statistical tests and automated certification. DQM is intended to be used both online, during data taking, and offline, during the reconstruction stage at Tier-0 and re-reconstruction at the Tier-1s (see section 2.2.5). The online system monitors detector,

trigger, and DAQ hardware statuses. While offline applications certify the quality of reconstructed data and validate calibration results, software releases, and simulated data.

4.1.1 Online monitoring

Online DQM applications are an integral part of the event data processing, as illustrated in figure 4.1(a). Each application, usually one per subsystem, receives event data through a dedicated Storage Manager event server[1]. A special stream of events is used to perform DQM operations [100]. The stream contains detector and trigger raw data, Level-1 and High Level Trigger (HLT) summary results, in addition to HLT by-products essential for monitoring trigger algorithms. Events are delivered to data quality applications on average at 10 - 15 Hz. Delivery speed strongly depends on the rate with which subsystem application process event data. There is no event sorting nor handling, and no guarantee parallel applications receive the same events.

Along with event data, the storage manager serves DQM applications with a limited number of histograms filled in the HLT filter units (FU), i.e. the logical nodes that compose the HLT processer farm. In the FUs event processing rate reaches 100 kHz and all events can be accessed, even those that have not passed any HLT filter. Thus trigger rates and rejection factors may be computed. Identical histograms produced across different FUs are summed and sent to the storage manager proxy, which saves them to files and delivers them to the DQM consumers.

In the online environment, DQM output, which includes histograms, alarm states and quality test results, is made available in real time to a central graphical user interface (GUI) [101], accessible form the web. Being web-based, this central GUI permits users all over the world to access the data and check results without installing experiment specific software. Monitoring data is also stored to ROOT files [102] periodically during the run. At the end run, final result files are uploaded to a large disk pool on the central GUI. Subsequently, files are merged to larger size and backed up to tape. Recent monitoring data (several months worth) are cached on disk for easy access. The GUI was custom built to fulfill the need of shifters and experts for efficient visualization and navigation of DQM results and not meant as a physics analysis tool.

Starting and stopping DQM online applications, as well as the storage manager proxy, is centrally managed by the CMS Run Control System [103], while the DQM GUI web server is completely independent.

[1]The Storage Managers (SM) are subcomponents of the HLT Filter Units, i.e. the logical nodes that compose the HLT processer farm. SMs handle the transfer of event data out of the FUs to the software layer above them.

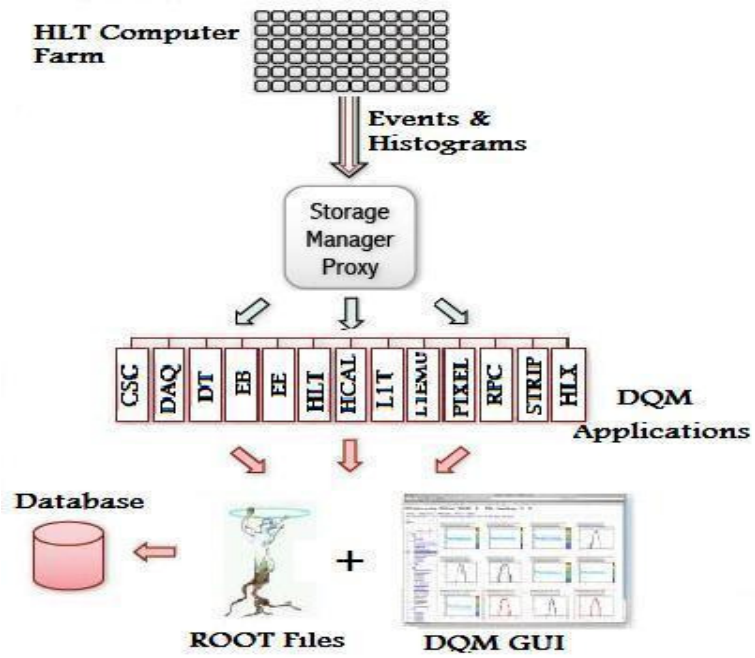

(a) Online DQM system.

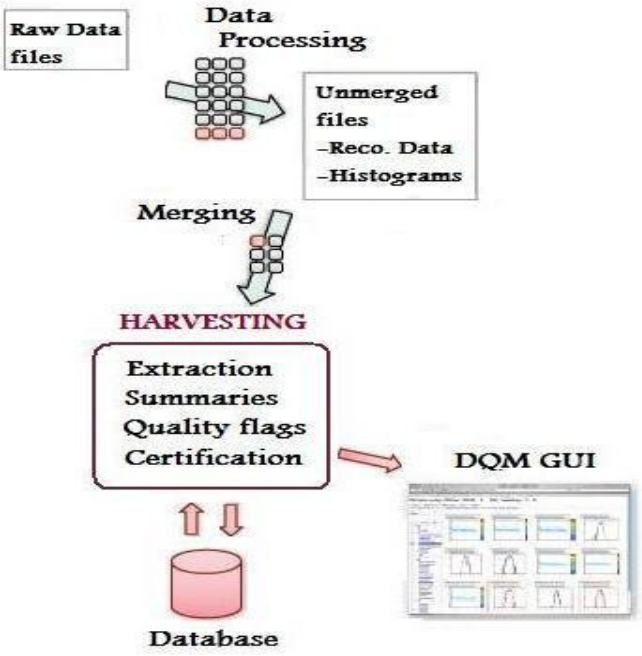

(b) Offline DQM system.

Figure 4.1: DQM workflows for online (a) and offline (b).

4.1.2 Offline monitoring

Offline DQM, schematically represented in figure 4.1(b), runs as part of the reconstruction process at Tier-0, of the re-reconstruction at the Tier-1s [60], and of the validation of software releases, simulated data, and alignment and calibration results. Despite the difference in location, data content and timing of these activities, offline monitoring is unique and formally divided into two steps. First, histograms are created and filled while data are processed event by event. Monitored information is stored along with normal event data files. The second step is called harvesting. During this step, histograms and monitoring information produced in step one are extracted and merged to yield full statistics. Efficiencies are calculated, summary plots are produced, and quality tests are performed. The automated data certification decision is taken here (see section 4.4 for more details).

The disadvantage of offline monitoring is the latency of reconstructed to raw data, which can be as long as a few days. Tier-0 has a time delay of one - two days at most, whereas Tier-1 re-processings take from days to weeks. Alignment and calibration quantities are validated with a latency of hours to few days. The validation cycle of simulated data depends entirely on sample production times, and varies anywhere from hours, for release validation, to weeks, on large data samples. On the other hand, the advantages are substantial. All reconstructed events can be monitored and high level quantities are available. This allows rare or slowly developing problems to be identified.

At the end of the offline DQM process, the output data file is uploaded to a large disk pool of the central DQM GUI server. There files are merged to larger size and backed up to tape; recent data is kept cached on disk for several months. Moreover, online and offline GUI servers provide a common look and feel and are linked together as one entity. Thus, the entire CMS collaboration can access DQM data at a single central location.

4.2 RPC DQM System

4.2.1 Requirements

The RPC DQM system [104] is composed by a set of dedicated tasks which debug hardware, monitor detector performance and assess data quality by monitoring detector level and physics quantities. The parameters the RPC DQM group has chosen to monitor are various. They include:

occupancy - Occupancy is defined as the distribution of single hits per channel. Figure 4.2(a) shows the occupancy of a given roll in the barrel region as computed by the online DQM during a run without collisions (noise run). The plot clearly shows a dead region, 8 strips wide, which corresponds to a non functioning chip in a front-end board of the RPC chamber. This is more clear, if compared to the occupancy distribution of a fully working neighboring roll (see figure 4.2(b)). Reasons for bad occupancy distributions are various: malfunctioning supply of readout electronics (fully dead roll), faulty or disconnected cables (group of 16 dead strips), non functioning front-end board or chip (group of 16 or 8 dead strips), wrong channel mapping, or problems in the gas flux system. In all cases, investigation by a detector expert is required.

multiplicity - Multiplicity, i.e. number of single hits per event within a same roll, is a fair indicator of uncorrelated noise problems. High levels of noise may lead to fake triggers and give problems during the reconstruction phase. It is therefore crucial to monitor this parameter at chamber level.

cluster size - A cluster is a group of consecutive strips within a same roll fired at the passage of a incident muon. The number of strips in a cluster is called cluster size. RPC cluster size depends on strip pitch, on working-point parameters (high voltage value and gas mixture), on muon impact point, and on muon track crossing angle, as shown in figure 4.3. The RPC system has been designed to have an average cluster size lower than 2.0 in order to achieve the required momentum resolution and minimize the number of possible ghost-hit associations. An average cluster size greater than 2.5 could indicate bad working-point parameter or very high correlated noise (electronic noise) .
In addition, it has been shown that a "low" cluster size (~ 1) may suggest the presence of one or more noisy strips. In other words, if a big percentages of clusters in a roll have size 1, these cluster are not likely produced by an incident muon. Instead, they might be a sign of noise and require detector expert attention. This argument is better explained in section 4.3, where the RPC Quality State Machine is introduced.

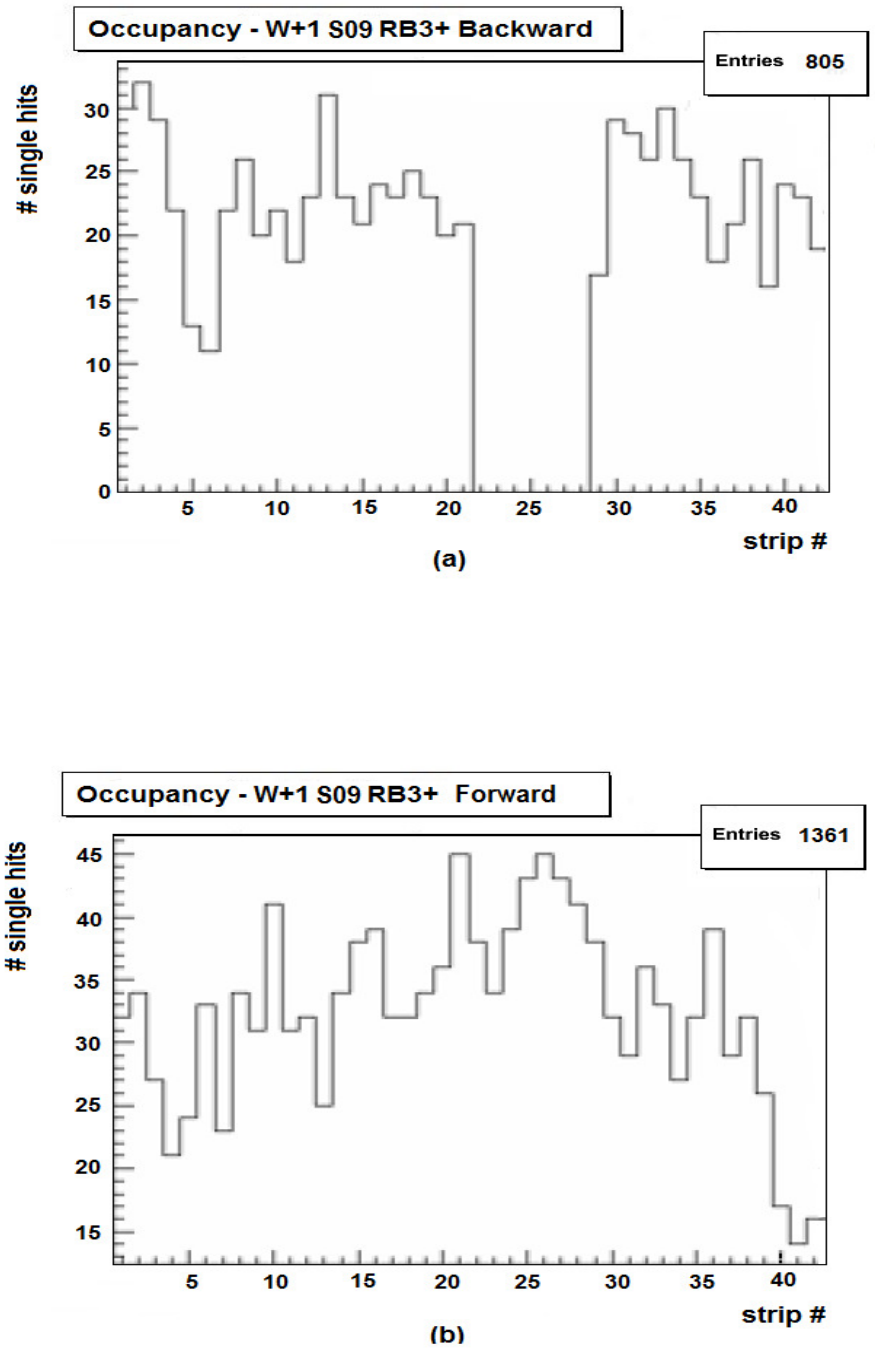

Figure 4.2: The figure (a) shows the occupancy plot for the given roll in the Barrel region. A dead region is clearly present. Plot (b) shows the occupancy of a fully functioning neighboring roll.

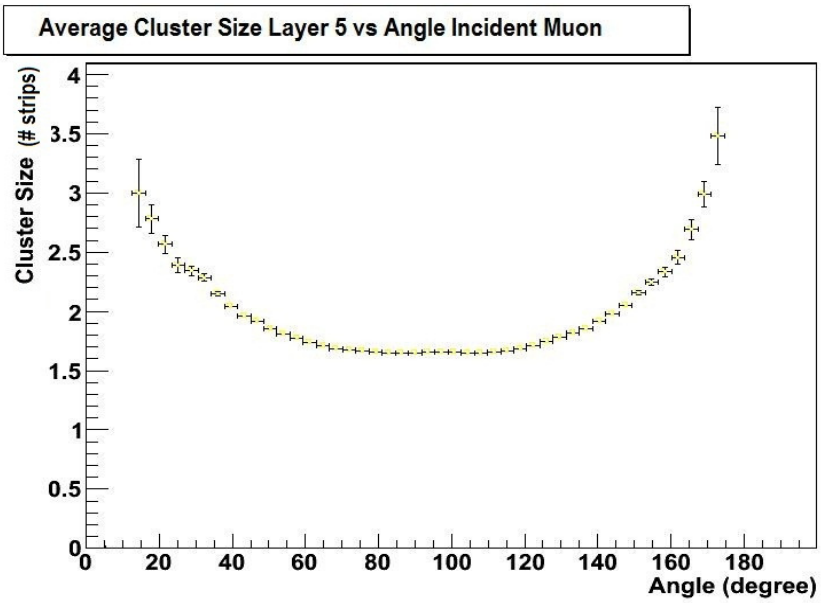

Figure 4.3: Average cluster size as a function of the angle between incident track direction and the strip plane for the fifth RPC barrel layer. As expected, minimum is reached around 90°.

data integrity - Inconsistencies in detector, readout channel, or electronic channel identification numbers are checked, as well as data size and data format. Presence of corrupted data is considered a fatal error that leads to stopping the run and flagging the data itself as not usable for analysis. For every event, data integrity must be checked and, in case of problem, immediate action must be taken to avoid wasting runtime. Figure 4.4 shows an example of how a problem in the integrity of collected data can be promptly spotted using DQM tools. A general 2D-histogram (figure 4.4(a)) shows the shifter the RPC Front End Drivers (FED) [105] are in warning state. The expert, once alerted, checks more detailed histograms. He or she confirms that one of the RPC FEDs, namely FED 790, is sending error messages at almost every event (non-zero entries in the first bin of figure 4.4(b)). Accessing more refined information allows to spot the nature of the problem and intervene accordingly. In this particular example, data contained invalid IDs from the RPC data acquisition system and the problem was solved resetting that particular FED.

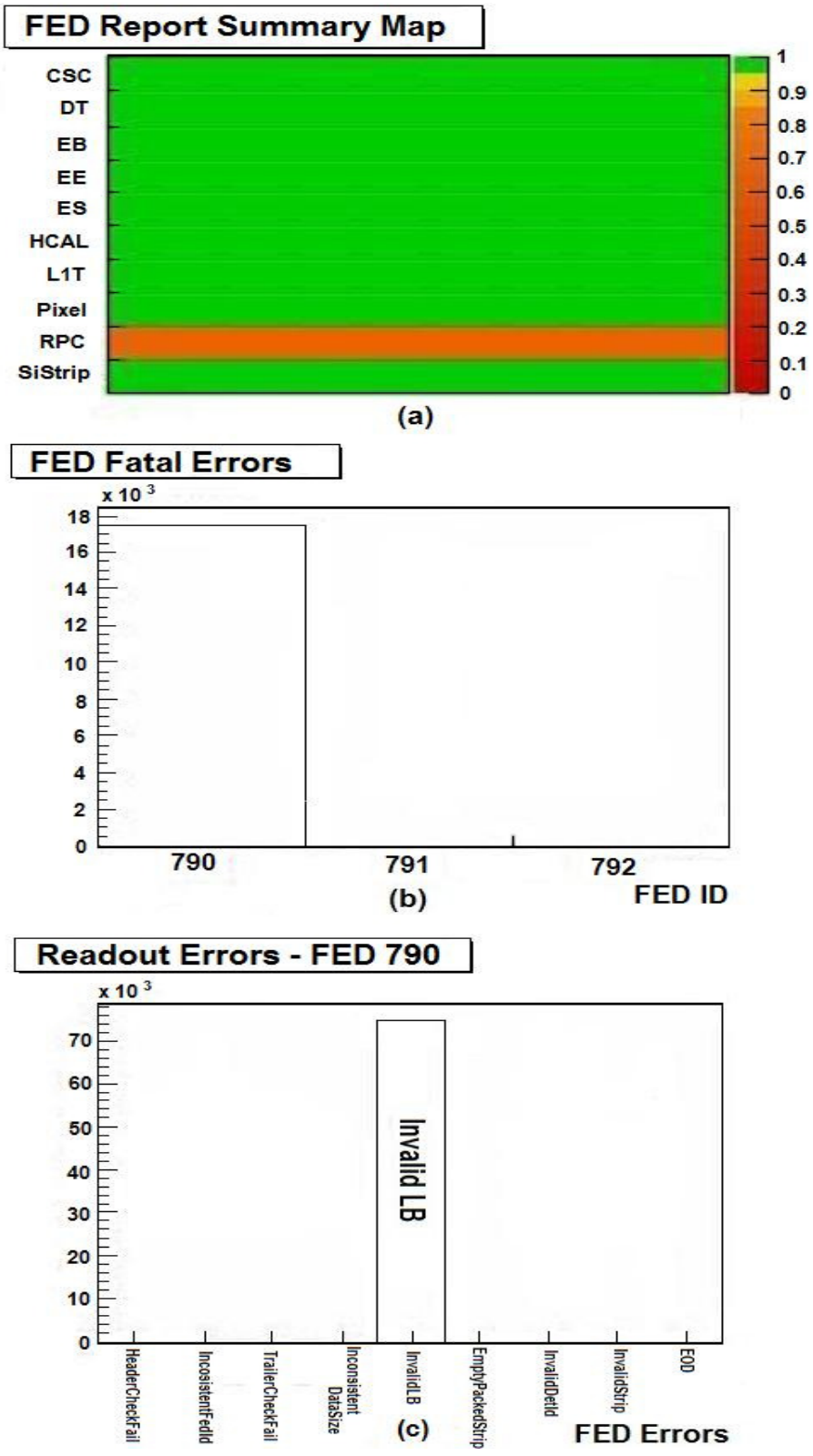

Figure 4.4: Examples of a FED error messages correctly detected by the DQM. The warning state is clearly visualized in the shifter summary plot (a). Non-zero entries in the first bin of (b) pin point the problem to FED 790. Figure (c) shows the nature of the problem.

synchronization - Possible sources of data misalignment are: variations in particle time of flight, signal formation and propagation within a detector, connections between various elements, set-up times, and jitters of digital electronics.
Good synchronization is crucial for the successful operation of the experiment. Detector and trigger inefficiencies may be caused by wrong timing.
For this reason, delay of RPC signals with respect to trigger signals is monitored by DQM applications. The delay is given in units of bunch crossings (25 ns). In addition, time alignment of hits due to a crossing muon is calculated. The spread in time is also given in units of bunch crossings.

noise - RPC noise rates must be carefully monitored. In fact, abnormal noise values may result in high fake muon trigger rates. Before data taking, dedicated calibration data are taken and analyzed to identify and mask, i.e. exclude from readout, channels with 100 Hz/cm^2 noise rate or more.
A dedicated RPC noise monitoring tool is used to measure noise values directly. In addition, careful studies of cosmic data have shown that cluster size and multiplicity distributions are good "indirect" indicators of noise. "Indirect noise" algorithms based on these two parameters are further explained in section 4.3. Their results are less precise, but faster and better performing.

efficiency - Detection efficiency is monitored only in the offline environment, where reconstructed objects, i.e. muons, are available. Efficiency, defined as the number of reconstructed hits over the number of expected ones, is measured for each roll. In order to estimate RPC muon detection efficiency, information from the Drift Tubes (DT), in the barrel, and Cathode Strip Chambers (CSC), in the endcaps, are used. DT/CSC segments, associated with a reconstructed muon, are linearly extrapolated to a neighboring RPC surface. RPC reconstructed hits are searched for in proximity ($\pm$ the equivalent distance of 2 strips) of the extrapolated point. A graphic representation of this so called *segment extrapolation* efficiency algorithm, is given in figure 4.5. Residuals, i.e. distance between the predicted impact point and the reconstructed RPC hit, are also measured. The central strip in the cluster is taken as an estimator of the position of the reconstructed hit.

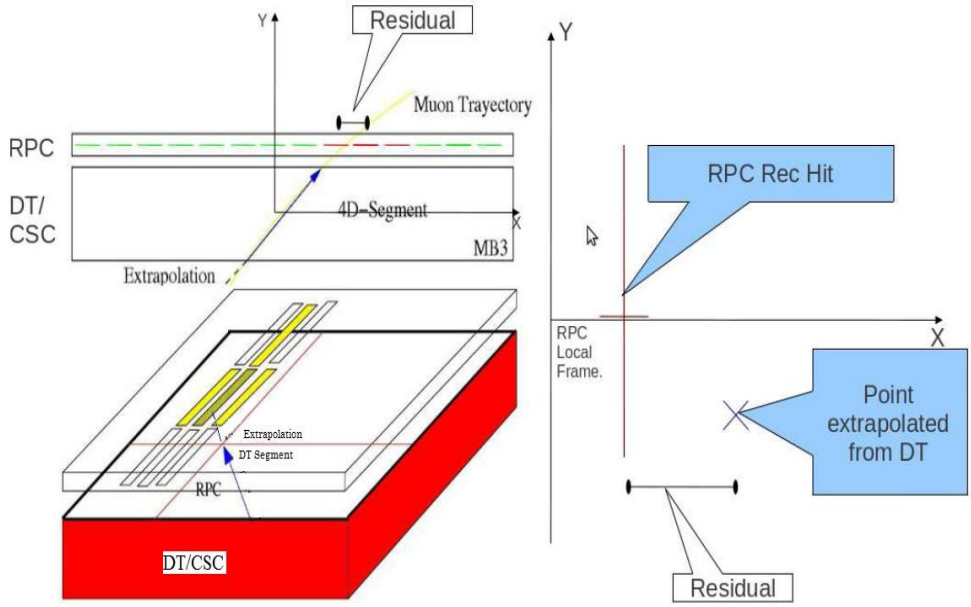

Figure 4.5: Graphic illustration of the *segment extrapolation* efficiency algorithm.

4.2.2 Structure

The RPC DQM system has been developed within the compass of the CMS reconstruction and physics analysis software framework, CMSSW and based on object-oriented programming languages: C++ [106] and Python [107]. It has been designed to be flexible and easily customizable so to be used within different monitoring environments: online/offline DQM and standalone programs for private analyses. Every data analysis and monitoring algorithm has been implemented in a separate module, completely independent from the others. Each module, called an *EDAnalyzer* within CMSSW, may be added or eliminated from the monitoring sequence at need. Different parameter configuration files allow to run on both detector and simulated date without requiring code changes nor re-compilation. The modules have been organized in a source/client structure, as schematically shown in figure 4.6.

Source modules access information from the events, define the quantities to be monitored, and fill histograms. Histograms are defined for each roll (chamber η partition) and for larger detector segments, such as sectors (60) and wheels (5) in the barrel and rings (12) and disks (6) in the forward regions. Event selection is performed at this level. In the online environment, the RPC DQM Group decided to accept all single and double muon trigger path and, for early data only, minimum bias events too. The selection is done upstream of all source modules and is externally configurable. Offline applications instead run on the full statistics of every dataset sample processed in Tier-0 and in the Tier-1s.

Client modules periodically access the histograms and perform analyses. Frequency of the access depends on the monitored quantity, varying from every luminosity section (23 s) to once a run. Clients have the tasks of: creating summary histograms, performing quality tests, calculating alarm levels, saving the output in ROOT files, and taking a preliminary data certification decision. In addition, summary plots are created by the clients by combining information from individual low level histograms to yield a general and fast overview on the entire RPC system.

Commissioning of the system during cosmic data taking and early collision data has shown that online algorithms can process data up to a rate of 40 Hz. The offline modules were successfully integrated in the official CMS software releases, proving to be stable, robust, and not CPU demanding.

A total of $\sim 1.7 \times 10^3$ histograms are produced in the online environment and $\sim 3 \times 10^4$ in the offline. All information is stored to a ROOT file, intended for expert use only. File dimensions are usually of the order of 20MB. Histograms are also uploaded to the central GUI. A screen shot of the web GUI with a selection of RPC DQM plots is shown in figure 4.7.

Histograms are organized in a hierarchical tree-like folder structure reproducing detector geometry, starting from the overall RPC detector down

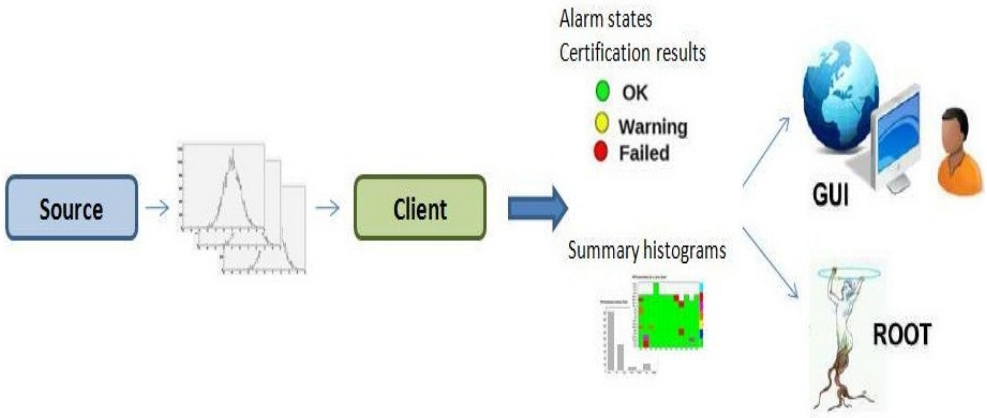

Figure 4.6: Illustration of the source/client structure of the RPC DQM.

to the single electronic channel. Since navigating through folders and several thousand histograms is complicated for non-experts, special layouts containing only summary histograms are prepared for both RPC and central DQM shifters. Purpose of shifter histograms is to allow the shift crew to quickly identify problems and take action. These histograms are meaningful, not overwhelmed with information and equipped with a clear set of instructions. Reference histograms may be superimposed and *Quality Tests* (QT) are applied. Checks are performed on the fraction of dead channels, the average cluster size for each chamber η-partition, synchronization, and eventual presence of Front End Driver (FED) errors[105]. The tests are repeated every 5 luminosity sections ($\sim$ 115 seconds) and alarm states are displayed on the GUI. Fast feedback is thus provided to the shift crew about the data quality in terms of warnings, alarms or error reports. In order to evaluate the validity of the monitoring data content in an automated and uniform way, QTs have been standardized and integrated within the CMS DQM framework. They include among others: comparison with reference histogram using ROOT χ^2 algorithm and ROOT Kolmogorov algorithm, check that histogram contents are between (Xmin,Xmax)/(Ymin,Ymax), evaluation of the fraction of bins whose content is above a threshold, compared to neighboring ones fraction of bins that passed the test, and test that the mean value is within expected range. All QTs return a float in the range $[0, 1]$ whose encoding depends on the specific test and all are configurable through the XML parser.

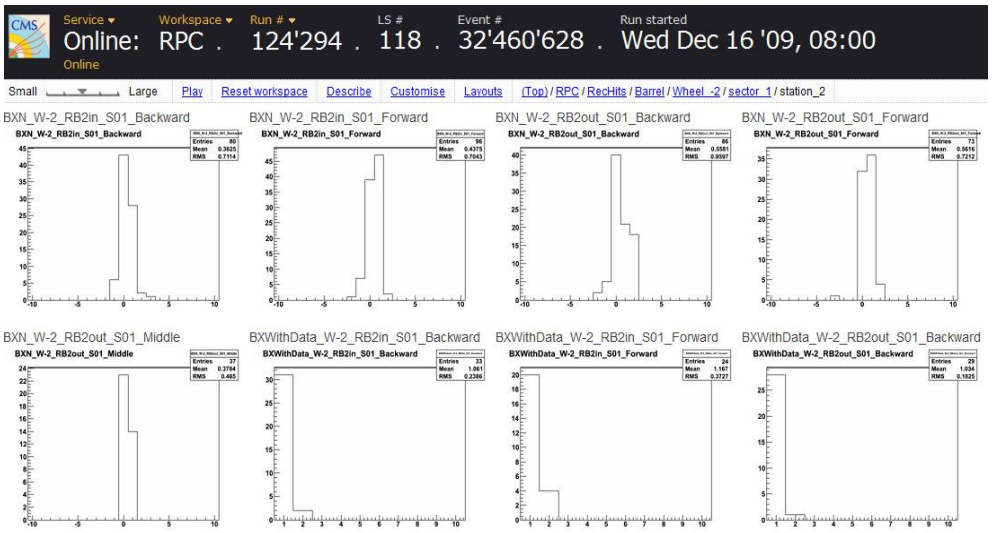

Figure 4.7: Screen shot of the DQM GUI showing a selection of RPC histograms.

4.3 Quality State Machine

Dimensions and complexity of the RPC system - it covers a surface of 2953 m^2 and counts about 11×10^4 electronic channels - demand a high level of automation in monitoring processes, to reduce human errors and optimize recovery procedures. But automation comes with the need to describe the behavior of the system in an accurate way. To this purpose, the RPC DQM Group analyzed detector performance during the Cosmic Run At Four Tesla (CRAFT08) exercise [108] in late 2008. CRAFT08 lasted one month during which CMS recorded around 300 million cosmic events with its magnet field reaching a maximum value of 3.8 T. These muons were used to understand the behavior of each chamber and of the RPC system as a whole. Later, the results obtain were confirmed, and where necessary refined, by subsequent studies using 2009 cosmic data and early LHC collision data in 2010. All plots shown in this section were produced using collisions events (center-of-mass energy = 7 TeV) recorded by CMS in the second half of 2010 and containing at least one reconstructed muon. RPC working point was set at 9.3 kV in the barrel and 9.5 kV in the endcaps, with a 220 mV threshold for all chambers.

A total of seven detector states were identified: Good, Off, Dead, Partially Dead, Noisy Strips, Noisy Roll, Bad Occupancy Shape. The first two states do not need explaining, while a few words must be spent on the following five.

Extended dead regions negatively affect detector and trigger efficiencies

and must be avoided. Studying the distributions of the fraction of dead channel in a roll (figure 4.8), two problematic areas were identified: between 0.5 and 0.8 and ≥ 0.8 of dead, i.e. non-responding, channels. Every electronic channel corresponds to a strip. The number of strips varies from 36 to 90 in the barrel region, while all endcap chambers have 32 strips per roll. Rolls falling in these two categories are defined as *Partially Dead* and *Dead* respectively.

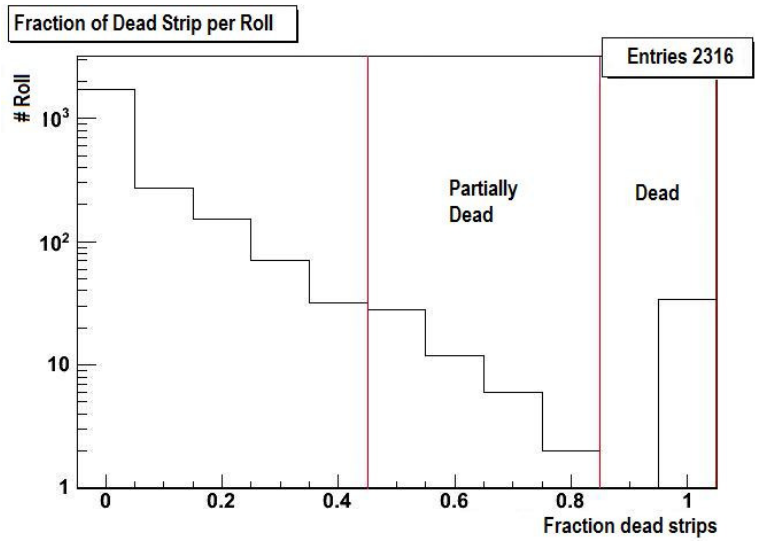

Figure 4.8: Distribution of the fraction of dead strips as computed by the offline DQM after 91214 muon events.

Monitoring noise levels is fundamental. Low noise rates are necessary for proper functioning of trigger algorithms and to limit the rate of fake triggers, which must not exceed 0.5% [55]. Evaluating noise rates within the DQM framework is tricky since DQM application access only a selection of events. A work-around to this problem has been found. Studying strip occupancies, it was noticed that noisy strips have an occupancy at least 3.5 times higher than the average strip occupancy for the same roll. Figure 4.9 shows the occupancy plot for a *Noisy Strip* roll. When a strip is declared noisy, experts take care of excluding it from readout before investigating the source of the noise itself. Furthermore, when a roll has one or more noisy strips, a large fraction of reconstructed hits have cluster size equal to one. In figure 4.10 the distribution of the fraction of hits with cluster size one in disk D+3 is given as an example. All rolls falling beyond the threshold of 0.88 have been investigated. All presented one or more noisy strips.

Continuing, rolls completely, or for large part, affected by noise where spotted. In this case the above analysis appears to be useless useless. Studying the average cluster size of such rolls it was found to be ≥ 6 in all cases.

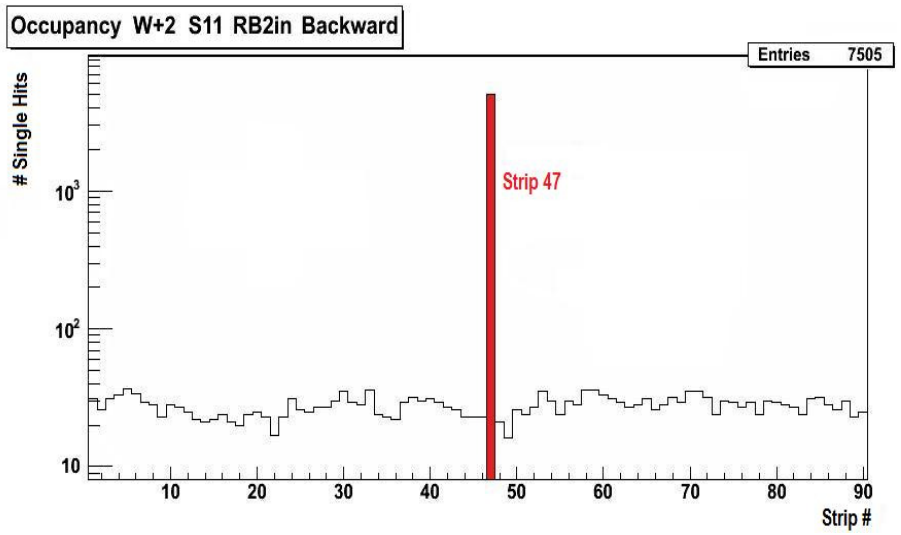

Figure 4.9: Occupancy distribution for roll RB2in_Backward of wheel W+2 sector S11. The noisy strip has been highlighted in red.

The average multiplicity distribution for the entire RPC system is shown in figure 4.11 for run 142317. Instead, figures 4.12 (a) and 4.12 (b) allows to compare the occupancy plot a *Noisy Roll* to a neighboring one that does not present this problem. Noise seem to affect only half roll. Multiplicity distribution for these rolls distributions also are shown. (4.13 (a) and 4.13 (b)).

Results obtained with this analysis are in good agreement with those found with the RPC Noise tool [109].

Finally, the seventh detector category identified contains rolls with asymmetric (with respect to the central strip) occupancy plots. As already explained in section 4.2.1, deviations from the expected occupancy distribution shape must be monitored since they may be a symptom of a variety of problems. They may be due, for example, to malfunctioning in the electronics, in the gas system, or in the readout. The percentage of asymmetry currently admitted is less than 30%. Figures 4.14 and 4.15 show the occupancy distribution of a *Bad Occupancy Shape* roll and its neighboring roll in the positive endcap region.

All parameters and threshold values used to define the different states were obtained by a fine analysis of detector performance using cosmic data collected in 2008 - 2009 and subsequently tuned on early LHC collision data. Only runs where detector conditions were known and the status of each chamber had been verified were used. All parameters are externally configurable and may changed at expert request.

Once all possible detector states had been clearly identified development

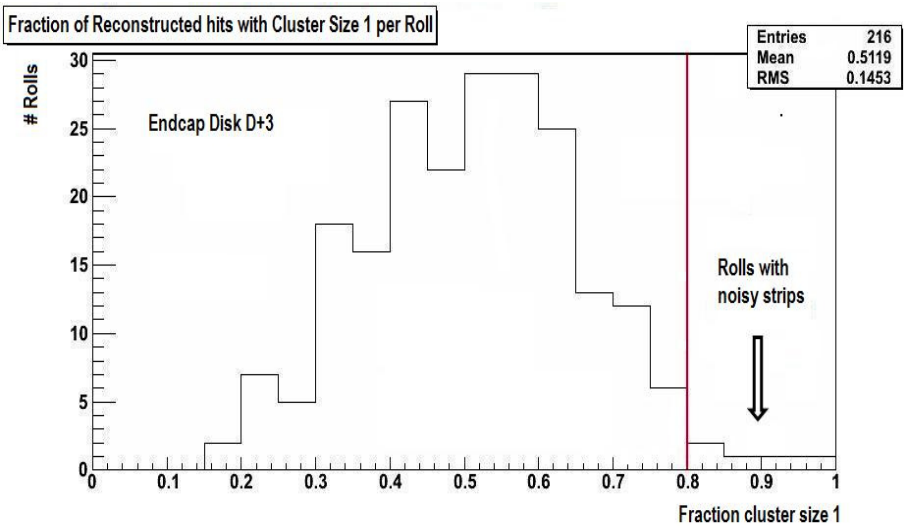

Figure 4.10: Distribution of the fraction of hits with cluster size one in disk D+3

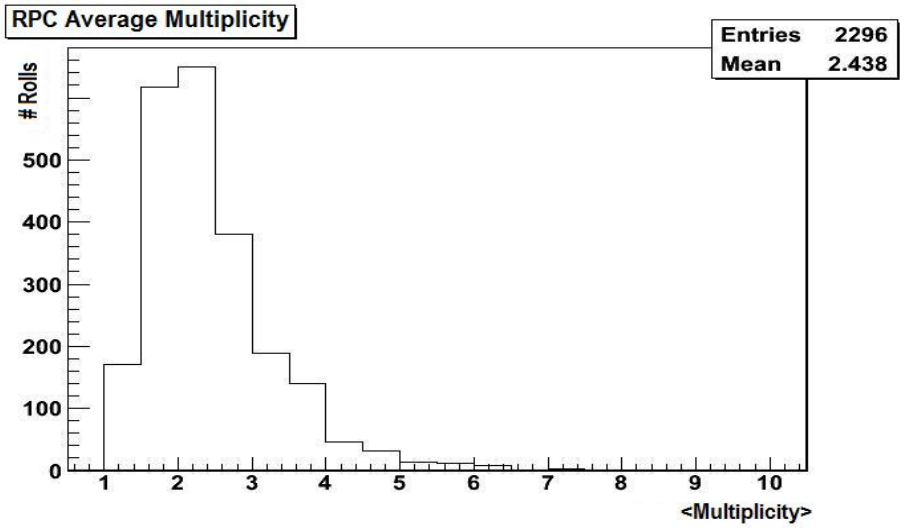

Figure 4.11: Average multiplicity distribution for the entire RPC system is shown in figure 4.11 for run 142317.

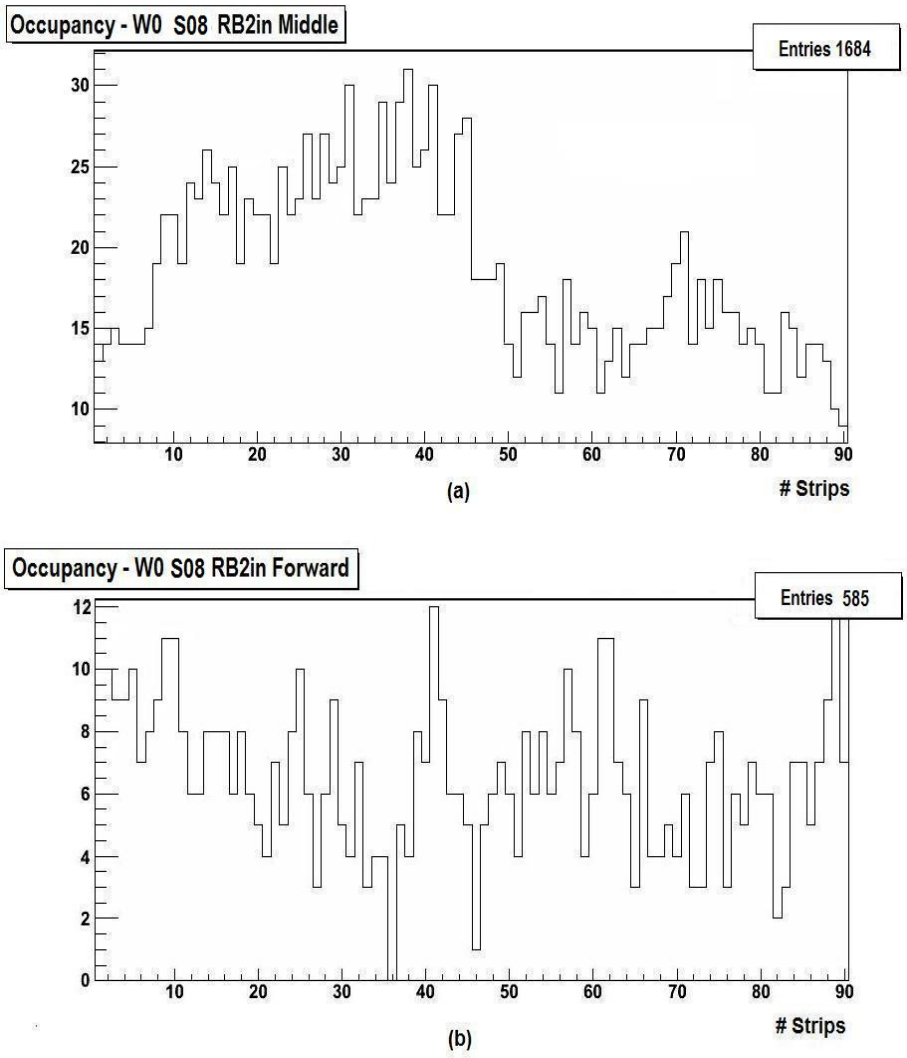

Figure 4.12: Occupancy plot of a *Noisy Roll* (a) compared to a neighboring one (b) that does not present this problem.

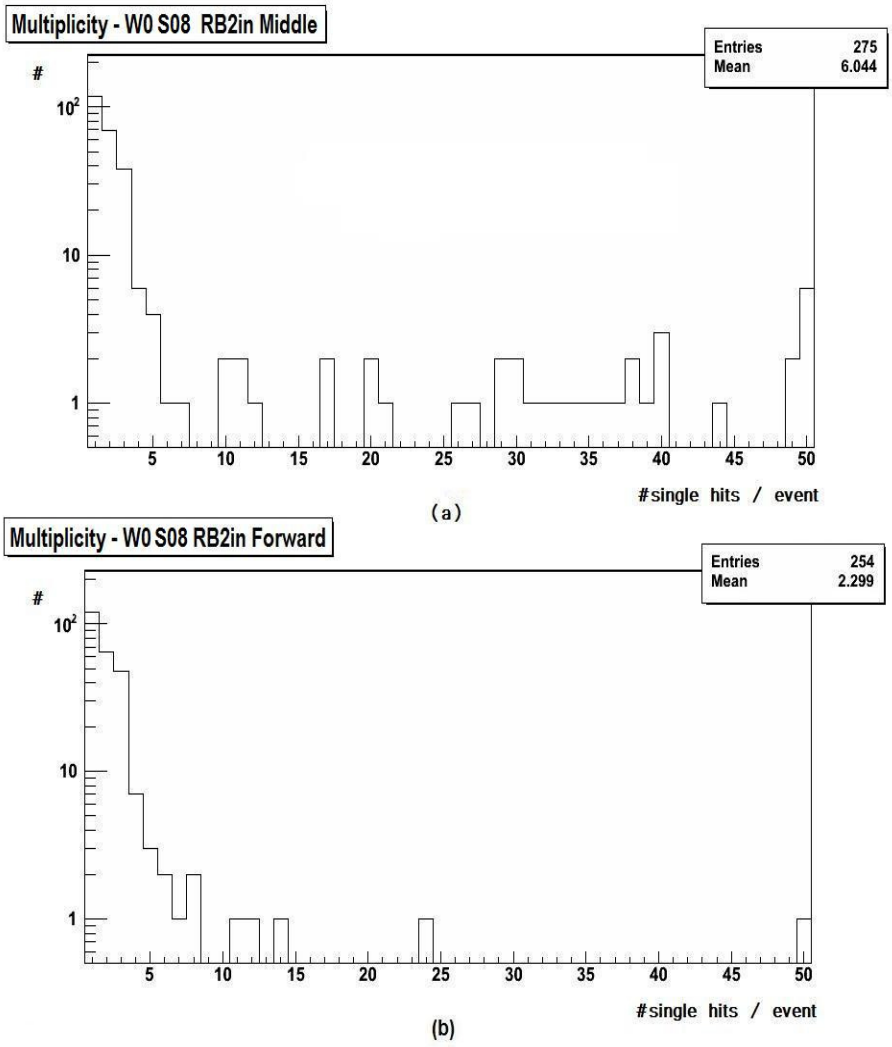

Figure 4.13: Multiplicity distribution of a *Noisy Roll* (a) compared to a neighboring one (b) that does not present this problem.

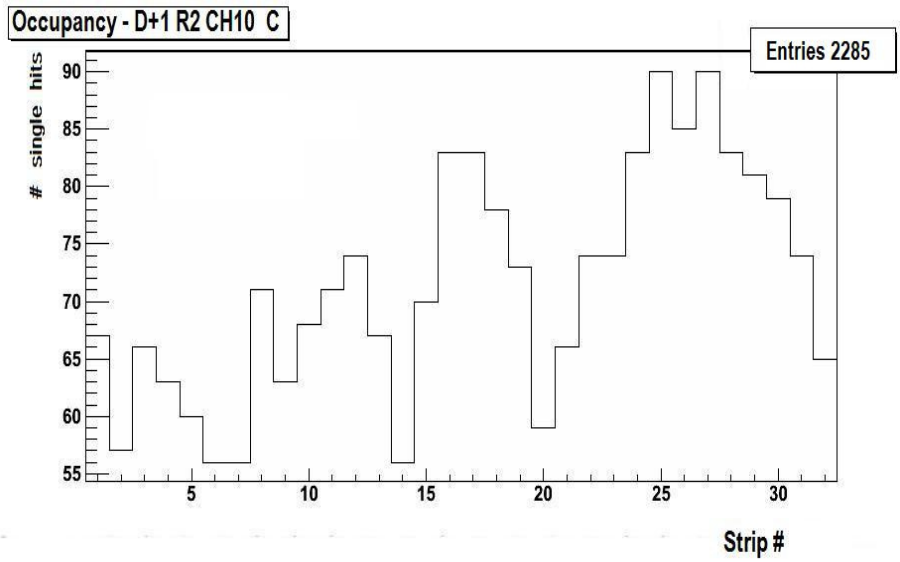

Figure 4.14: Example of asymmetric occupancy distribution.

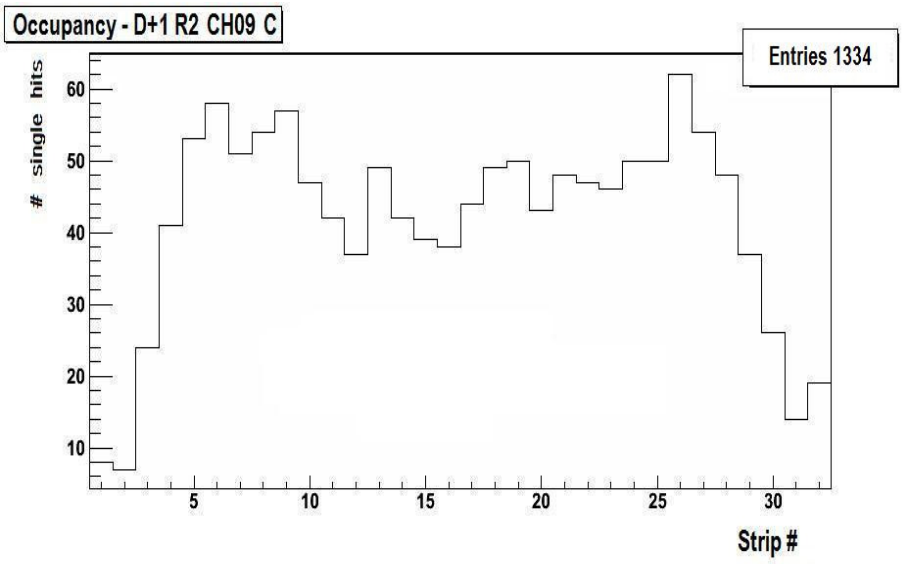

Figure 4.15: Example of a good occupancy distribution.

of the code started. The goal was to write a highly performing behavior model of the detector with a finite number of states and transactions among states. With these assumption, it was natural to direct all efforts towards Finite State Machines (FSM) based programming [110] techniques.

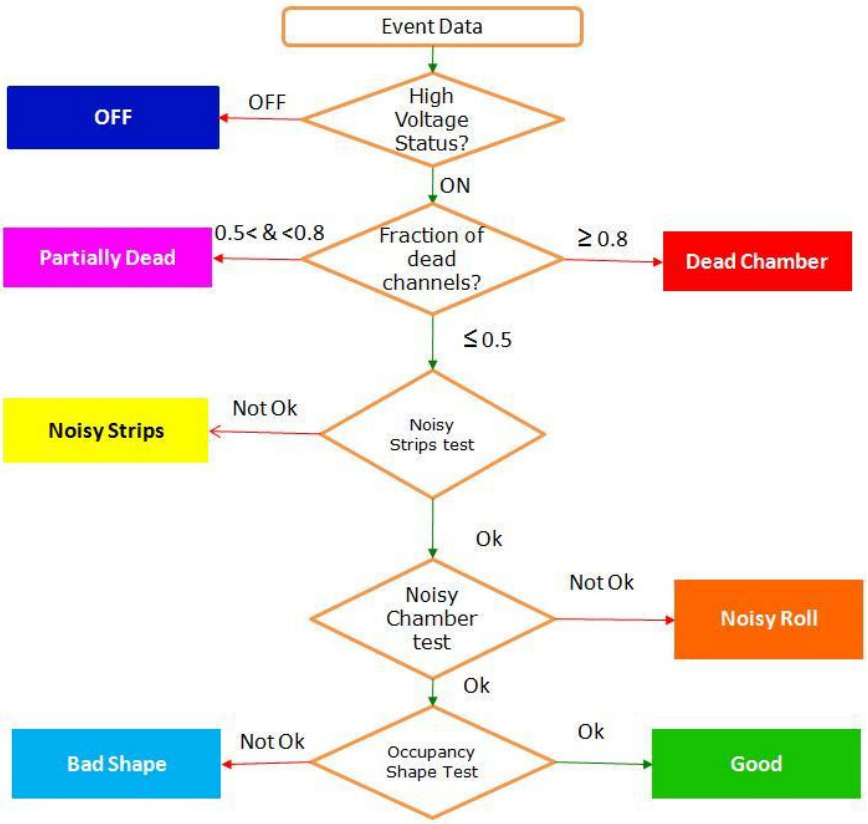

Figure 4.16: Workflow of the QSM algorithm.

The custom analysis algorithm developed, which has been named Quality State Machine (QSM), performs a series of subsequent tests (see figure 4.16) to determine each roll's status. Tests are performed in the order shown in the flowchart. When a roll is found to be in a given state, the algorithm exits and moves to the evaluation of the next roll. Thus, this analysis is light weight and respects time limits set for processing.

Quality results are displayed in eleven 2-D histograms representing major detector elements, as shown in the figure 4.17. Distributions of the number of rolls that fall in each of the seven categories are also produced (figure 4.18) along with a summary plot comprising to state of the entire system (figure 4.19).

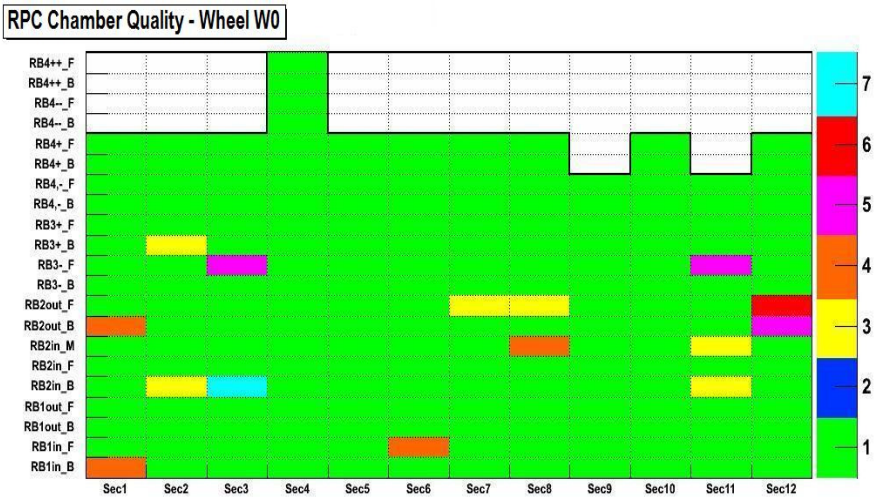

Figure 4.17: This figure shows the results of the RPC certification algorithm for wheel W0 during a collision run taken in 2010. The x-axis represents the 12 sectors in which the wheel is divided in the azimuthal angle ϕ, while rolls are displayed on the y-axis. The numeric/color code is: 1 = Good, 2 = Off, 3 = Noisy Strips, 4 = Noisy Roll, 5 = Partially Dead Roll, 6 = Dead Roll, and 7 = Bad Occupancy Shape.

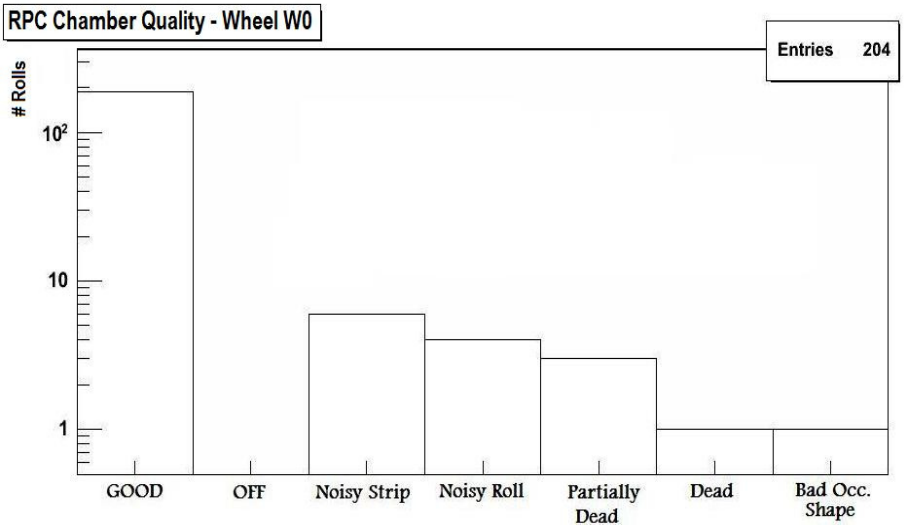

Figure 4.18: 1D representation of the 2D-histogram in figure 4.17.

The QSM algorithm was presented to the RPC collaboration in March 2009 and, after approval, integrated in the RPC DQM system as a client module. Since such time it has proven to be a valuable tool for assessing detector behavior and data quality. More details will be given in Section 4.4.

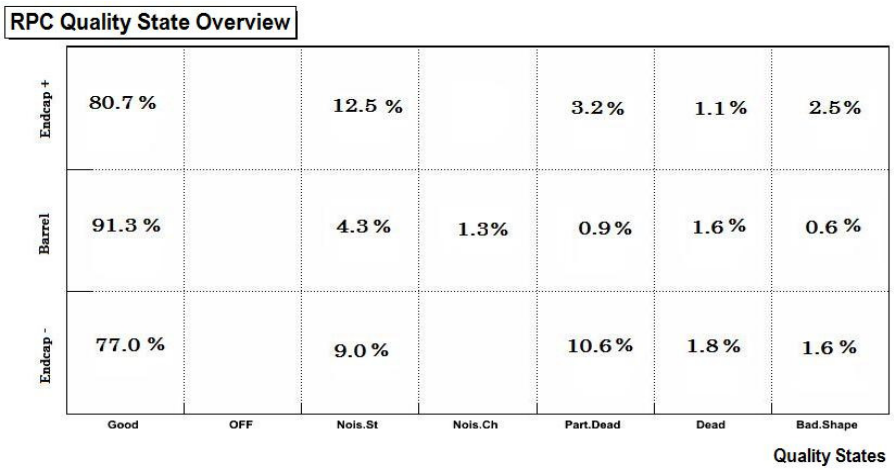

Figure 4.19: Summary overview of the RPC system as evaluated by the Quality State Machine for run 142317 (91214 events with at least a muon trigger).

4.4 Data Certification

Data certification [111] for RPCs is mainly based on the information coming from DQM online and offline but uses DAQ data too. The procedure can be divided in automatic and manual certification.

Automatic certification is based on the results of standard quality tests applied to the occupancy distributions of each roll. The fraction of responding Front-End electronic Boards (FEB), Front-End electronic Chips (FEC), or single electronic channels is computed. The application is flexible enough to switch among the three option at expert request. A FEB, FEC, or single channel is said to be responding when the number of single hits it recorded exceeds a certain threshold, currently set to 1. The ultimate result is a float number between 0 and 1 reflecting detector performance and a quality flag, i.e. “good”, “bad”, and in case no quality calculations were performed “unknown”. Following CMS specification, the quality flag is set to “bad” and expert intervention is required when the floating point value is beneath 0.95. Both flags are assigned to various detector segments. The RPC community chose to assess quality results at the granularity of the sector. There are 60

sectors in the barrel region and 36 in the endcaps. The quality information is displayed on the GUI as a list of floats and summarized in user friendly 2-D histograms (see fig. 4.20). In addition, a DAQ quality flag is calculated. This flag represents the percentage of allocated Front End Drivers (FEDs).

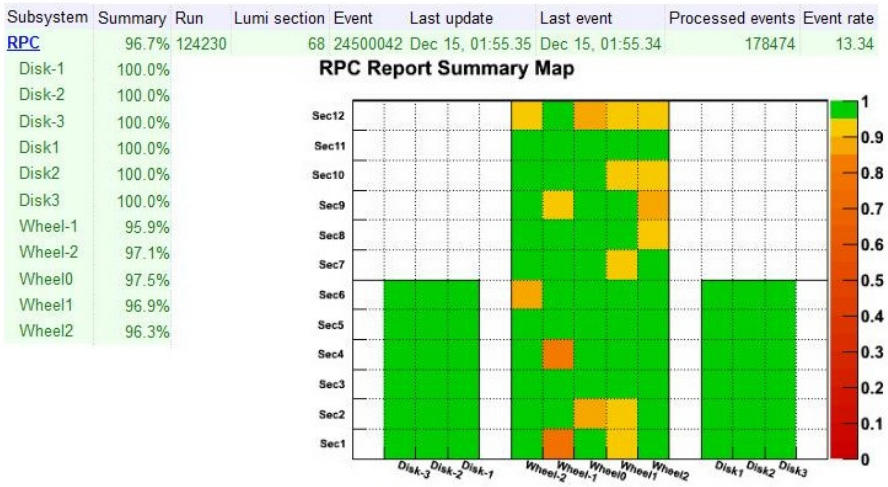

Figure 4.20: The automated certification results as displayed by the DQM GUI.

Manual certification is performed both online and offline by central DQM shifters. Online shifts take place twenty-four-seven, during detector operation at the CMS "on-detector" control room in Cessy, France. Offline DQM shifts are carried out, only in day time, at the CMS control center, on the main CERN site. Shift activities are supported by regular remote shifts; two shifts per day at Fermilab (USA) and one shift per day at DESY (Germany).

Shifters are asked to look at a limited number of summary histograms, produced by the Quality State Machine (section 4.3) and report on possible inconsistencies or problems. Instructions are available to facilitate this task. Shifter also monitor FED errors. In case of fatal errors, such as wrong FED IDs or inconsistent data size, the system is immediately flagged as bad. Offline shifters are also asked to monitor chamber efficiencies. An efficiency higher than 90% is considered "good".

Both during commissioning phases and during early LHC operations, the emphasis has been on the manual run-by-run certification, which relies on visual inspection of histograms. Presently, strong efforts are being made to move to the automatic certification with higher time resolution keeping the manual one as a control instance.

The end result is a list of "good" and "bad" runs, which is regularly

reviewed by detector experts. Weekly meetings are held by the Physics Validation Team, to collect the final decisions and communicate them to the entire CMS collaboration. At this stage quality flags are copied to the offline condition database[2] and to the Dataset Bookkeeping System (DBS) [112]. During the year 2009, RPC DQM certified 1979 runs, 547 of which are in presence of beams. The detector was flagged as "good" in 89% of the runs, "bad" in 8% of them. Certification procedures were not applied in the remaining 60 runs mainly due to lack of statistics or to failure of DQM applications. All "bad" runs have been reviewed and results found are given in figure 4.21. Five of them showed synchronization or trigger configuration problems, 50 presented low chamber efficiencies ($< 90\%$), 5 had FED errors, and 10 presented high noise levels. Thirty runs exhibited occupancy distributions different from expected. This was mainly due to experts working on system configurations. In 4 runs high voltage was off, while in 20% of the "bad" runs the system was in safe mode (low voltage on, but high voltage in standby) because of instable beams. Therefore, the detector was operating as expected but not in data taking conditions. Finally, in 28 runs DQM application problems caused automatic certification to fail and the quality flag was set erroneously to "bad" by the central DQM shifter. A clearer set of shifter instruction have been produced to avoid this mistake in the future.

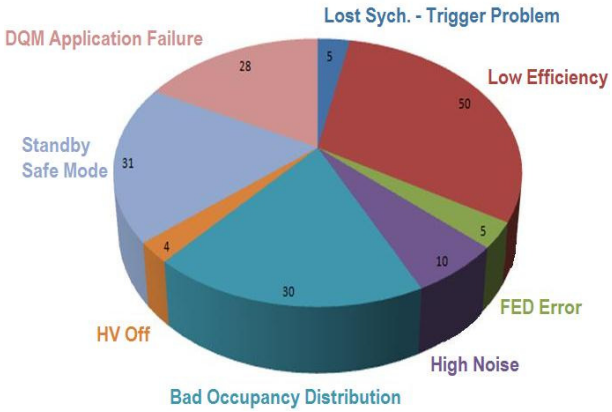

Figure 4.21: Pie chart illustrating the different reasons for "bad" data certification results 547 runs token in 2009 in presence of beams.

[2]A condition database is a database used to store data describing the state, i.e. the condition, of any detector subsystem. They include data quality indicators, bad channel lists, and detector settings needed in offline analyses.

In 2010, CMS has recorded 2184 runs with collision at 7 TeV center-of-mass energy. RPCs were excluded from 38 run, declared "good" in 2073 of them and "bad" in the remaining 73.

4.5 History DQM

As explained in the previous sections, DQM delivers monitoring information and data certification on a run-by-run. In other words, at the beginning of a new run, histograms and quality results are reset. No information from previous runs is available: a true fresh start. However, the need to monitor detector and trigger performance over time and run ranges has been expressed several times. Monitoring time evolution of physics parameters not only allows to control stability of the detector, but also to broadly identify the moment a given problem appeared, its duration, and recurrence. To meet this monitoring need, an auxiliary tool has been developed, the History plotting tool for Data Quality Monitoring system (HDQM) [113].

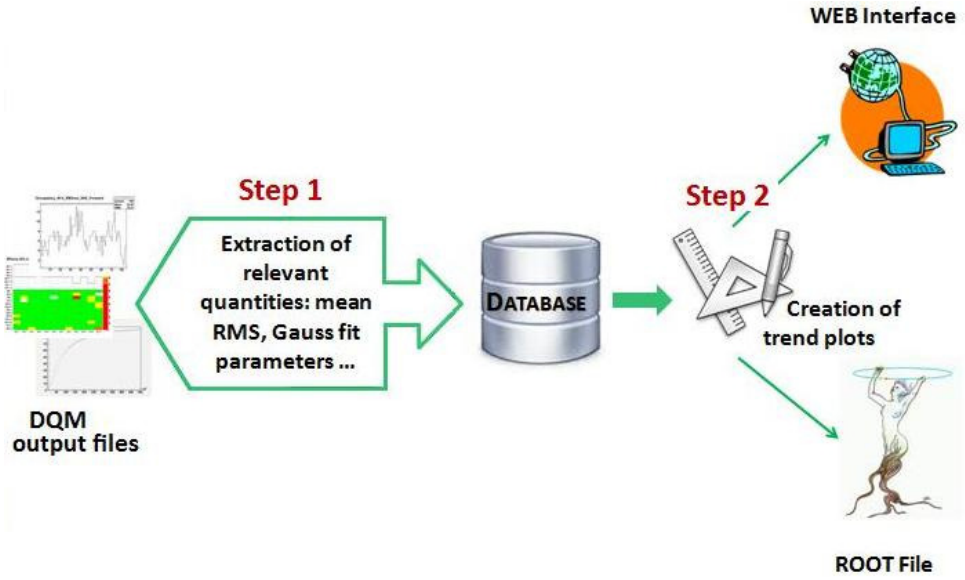

Figure 4.22: Two steps structure of HDQM: storage of summary information in the condition database and creation/visualization of trend plots.

HDQM has been implemented as a two step process (figure 4.22). The first step starts when the Offline DQM ends. DQM output files, in fact, hold the entire monitoring information: histograms, quality test results, and data certification decision. HDQM extracts relevant quantity values from such files and stores them in a condition database along with the run number they

refer to. The information that can be extracted from any given histogram quantities falls in four categories:

Statistical - This category comprises mean, RMS, and number of entries of any given histogram

Landau - Landau distribution parameters are included in this group: peak value, error and full width at half maximum.

Gauss - Gaussian fits may be performed on any distribution. Mean and RMS are returned.

User Defined - Any user defined quantity differing from the ones mentioned above finds a place in this fourth category. Examples are: number of entries in a given been, maximum/minimum of the distribution, average value calculated on the y-axis, etc..

Step two regards creation and visualization of trend plots; values extracted in step one are re-read from the database and plotted as a function of the run number. Plots are saved to ROOT files and made available on a WEB interface.

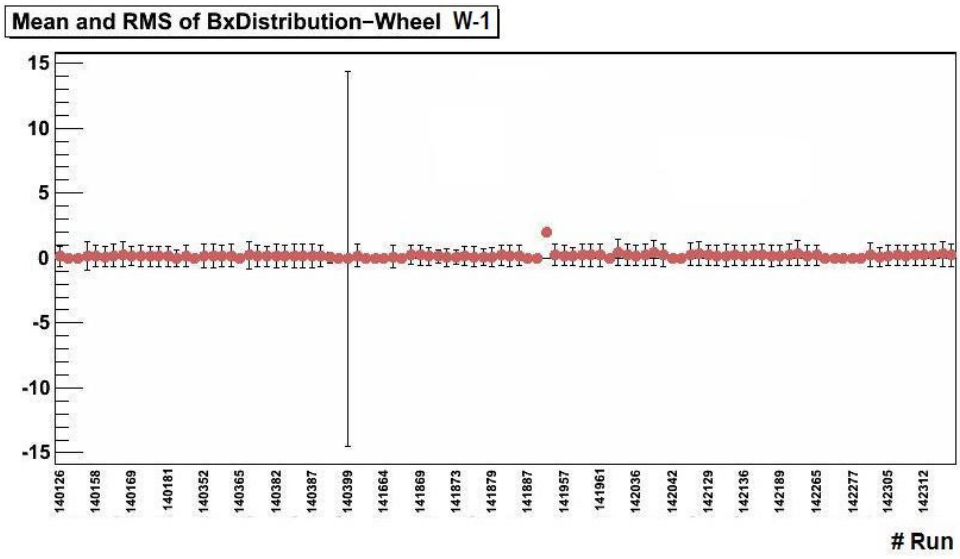

Figure 4.23: Time evolution of the bunch crossing mean and RMS for wheel W-1. Values are plotted as a function of the run number.

The RPC DQM Group uses the tools offered by HDQM to monitor the evolution in time of a handful of detector relevant parameters: total number of single hits, mean wheel/disk efficiency, bunch crossing mean value

and RMS, and number of rolls in each Quality State category (section 4.3). Meaning and physics relevance of these parameters has been already explain in section 4.2.1 of the present chapter. In figure 4.23 evolution in time of the bunch crossing mean and RMS for wheel W-1. Values are plotted as a function of the run number. The two runs where synchronization was lost are clearly visible.

Chapter 5

Detector and Trigger Performance

The RPC Data Quality Monitoring (DQM) system, in length described in chapter 4, is here used to study detector and trigger performance. CMS RPCs have, in fact, been extensively tested during production, assembly, installation, and commissioning phases. Hundreds of millions of cosmic muons have been collected in order to prepare for extended data taking. Now, after a year of LHC operation, 7 TeV collision data may be used to study detector behavior and trigger capabilities in true running conditions. Operations were important to assert system stability, debug hardware, synchronize electronics, and ultimately obtain a measurement of detector performance.

In the present chapter, RPC detector and trigger performance studies are presented. In section 5.1 results obtained with cosmic data, collected with the nominal axial field strength of 3.8 T and the tracking system on, are reviewed, while in the subsequent sections, performance results using 2010 LHC collision data are shown.

5.1 Cosmic Run Four Tesla

To commission the experiment for extended data taking the CMS collaboration conducted in 2008 a month-long cosmic-data taking exercises, known as Cosmic Run At Four Tesla (CRAFT08) [108]. CMS recorded 270 million cosmic-ray-triggered events, with the solenoid at its nominal axial field strength of 3.8 T and the tracking system on. Data recorded by RPCs during CRAFT08 runs are here analyzed using RPC data quality monitoring and performance tools. Detector and trigger behavior are studied.

RPCs participated in CRAFT08 with the entire barrel and a small fraction of the endcaps, which at the time were at an early commissioning stage. About 99% of the barrel electronic channels were active during the data taking, while the remaining 1% were masked due to high noise rate. Operating

voltage was set to 9.2 kV and readout electronic thresholds were set to 230 mV, corresponding to an induced charge of 180 fC [114].

A systematic study of chamber efficiency as a function of the operating voltage was performed for about 70% of the barrel chambers. Estimate of the average intrinsic detector efficiency is about 90%. This study also indicated a few hardware failures and cable map errors, now fixed.

Average noise per second and per cm^2 was computed for each roll. Distribution of the number of rolls as a function of the average noise is shown in figure 5.1, for one specific run. Only 3% of the rolls have an average noise rate greater than 1 Hz/cm^2.

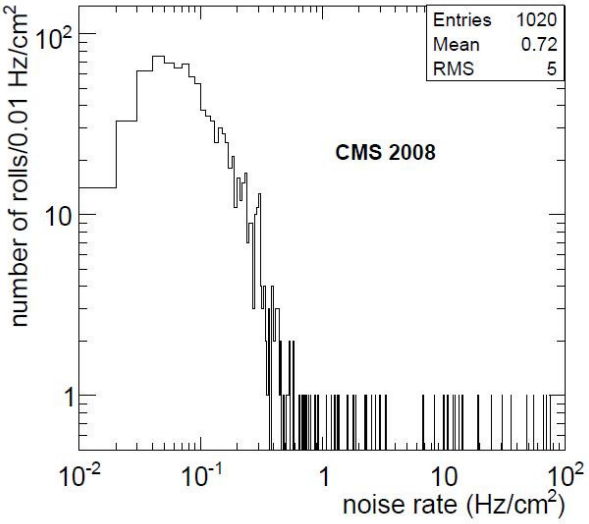

Figure 5.1: Distribution of the number of rolls as a function of the average noise during CRAFT08. Channels exceeding 100 Hz/cm^2 are masked and do not contribute to data taking. Operating voltage is 9.2 kV.

The average cosmic muon RPC trigger rate was about 140 Hz, for the barrel alone. Sporadic RPC trigger spikes related to noise pick-up from external sources were also detected, affecting about 10^{-3} of the total data taking time. A special effort has been made to understand the sensitivity of the RPCs to external noise sources. The detector grounding has been improved where possible, and further studies are in progress. Preliminary analyses have demonstrated that the fake trigger rate is reduced by two orders of magnitude when the LHC trigger algorithm is used instead of the dedicated cosmic ray trigger employed during the CRAFT exercise. The LHC trigger algorithm requires more stringent constraints on the incoming muon direction and is less sensitive to the detector noise.

Figure 5.2 presents a typical example of the time distribution of RPC

data. Time is measures with respect to the bunch crossing assigned by the RPC Level-1 global trigger logic, based on the coincidence of at least 3 chambers along a muon trajectory. The peak in the central bin corresponds to data which were synchronous with the RPC Level-1 trigger. The spread to two neighboring bins was mainly caused by incorrect choice of the synchronization phase, relevant only for cosmic ray runs. The spread over the other bins was due to non-perfect synchronization of contributing triggers, and to background noise.

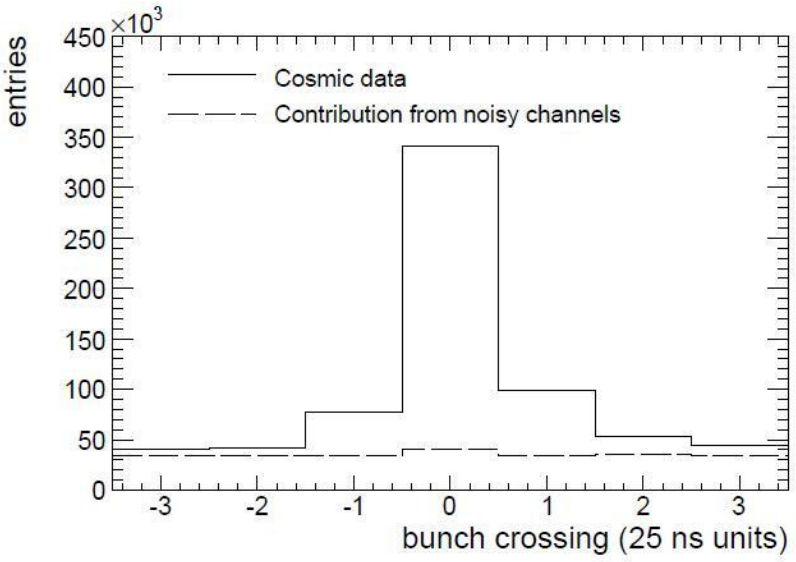

Figure 5.2: Time delay distribution (in bunch crossing units of 25 ns) of RPC data with respect to the RPC trigger signal. The dashed line shows the contribution of background electronic noise.

The CRAFT08 experience was repeated in 2009. In that occasion, CMS recorded 320 million events with the magnet solenoid at 3.8 T and the tracking system on. The RPC system was *fully* operational in CRAFT09 [115]. Data recorded by RPC in this occasion, is here used to calibrate the detector working point as function of the high voltage (HV) and front-end electronic threshold (TH). Samples of data are taken varying HV in the range 8.8 kV - 9.5 kV and fixing the TH at the two different values of 210 mV and 220 mV. An example of such analysis is given in figure 5.3. The roll noise rate, expressed in Hz/cm^2, is also shown in the same plot. Efficiency plateau is reached at 9.3 kV and noise values stay well below 1 Hz/cm^2 for this roll. Instead, in figure 5.4 the distribution of global efficiency for all RPC barrel chambers is shown.

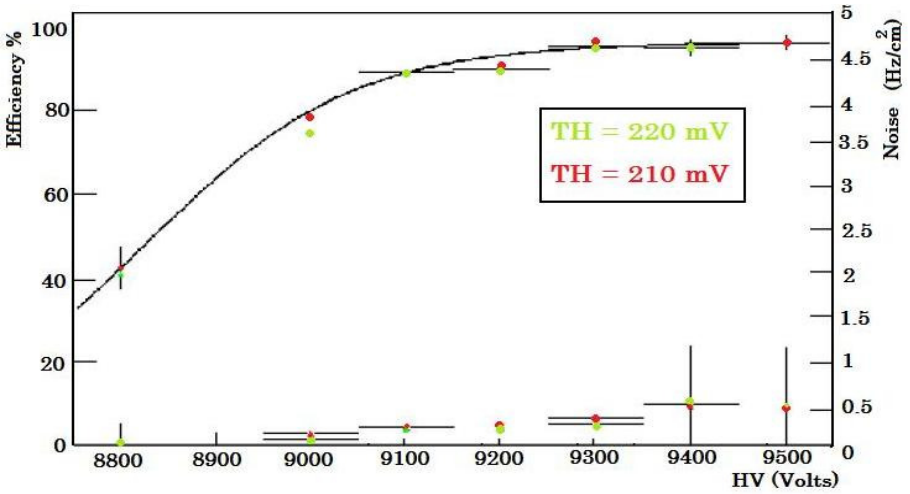

Figure 5.3: High voltage (HV) and threshold (TH) scan for a specific RPC roll during CRAFT09. In this case, plateau is reached at 9.3 kV. Noise rates are also shown.

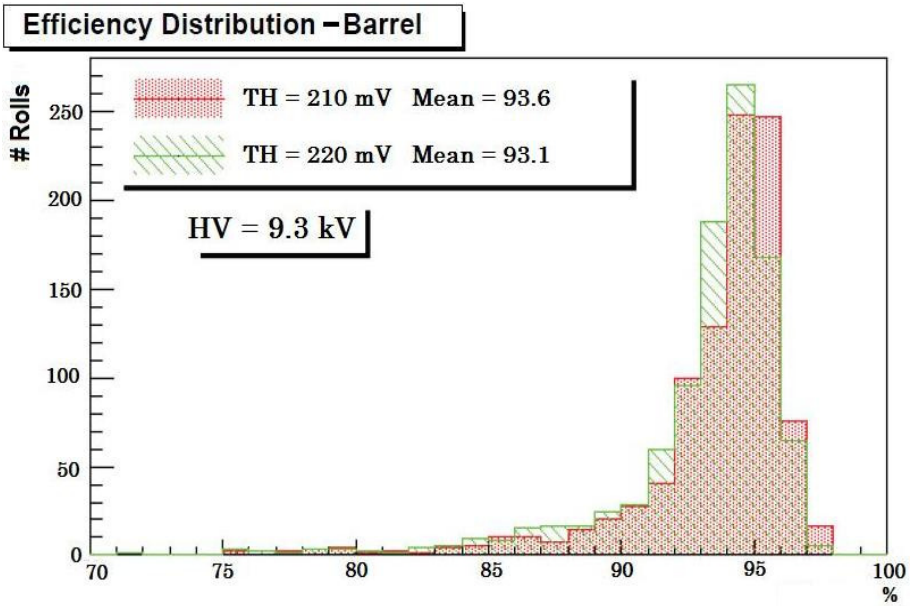

Figure 5.4: Efficiency distributions during CRAFT09. Operating voltage (HV) was fixed at 9.3 kV. Two different electronic thresholds (TH = 210 mV and TH = 220 mV) were used.

5.2 RPC Performance with 7 TeV Collision Data

The early part of 2010 saw the continuous ramp-up of LHC beam energies. On March 30^{th}, 7 TeV center-of-mass energy was reached. Collisions at this record-shattering energy continued until the end of October, after which commissioning for lead ions began. During these $\sim$ 7 months, CMS recorded 43.17 pb^{-1} of integrated luminosity. Here a sub set of this data is used to determine detector performance.

5.2.1 RPC Monitor Data Skim

To study RPC performance, a carefully tailored data skim has been adopted, the *RPC 2010 - 7 TeV COLLISIONS SKIM*, based on the official /MuMonitor/ dataset, recorded by CMS in p-p collisions at a center-of-mass energy of 7 TeV. A dataset is a set of files representing a coherent data sample. Datasets are produced by applying event selection criteria to collected data. In particular, /MuMonitor/ is a collection of events triggered by a selection of single-muon triggers and intended for monitoring purposes. On top of this, the official CMS JSON[1] file has been used to select only events taken with pristine detector conditions. In fact, JSON files allow to automatically select luminosity sections (23 s of data taking) with stable beams and with all sub-systems marked as "good" through data certification procedure (see section 4.4 for RPC data certification).

The data sample, used in the following analysis, corresponds to an integrated luminosity of 13485 nb^{-1}, recorded over 23 runs.

Selected events contain at least one high quality muon reconstructed in both tracking and muon system (*global muon*) with at least one valid hit in the muon chambers. A detailed description of muon track reconstruction in CMS can be found here [116]. Only muons with $|\eta| < 1.6$, corresponding to RPC geometrical acceptance, are considered. Muon transverse momentum p_T and pseudorapidity η distributions, as recorded by the Offline DQM, are shown in figures 5.5 and 5.6.

For all events passing the cuts, RPC hits associated to muon tracks reconstructed in the Muon system alone, i.e. *standalone tracks*, have been considered for cluster size, efficiency, and synchronization studies. RPC hits not associated to any reconstructed muon have, instead, been used in noise studies.

[1] JSON, acronym for JavaScript Object Notation, is a lightweight text-based open standard designed for human-readable data interchange.

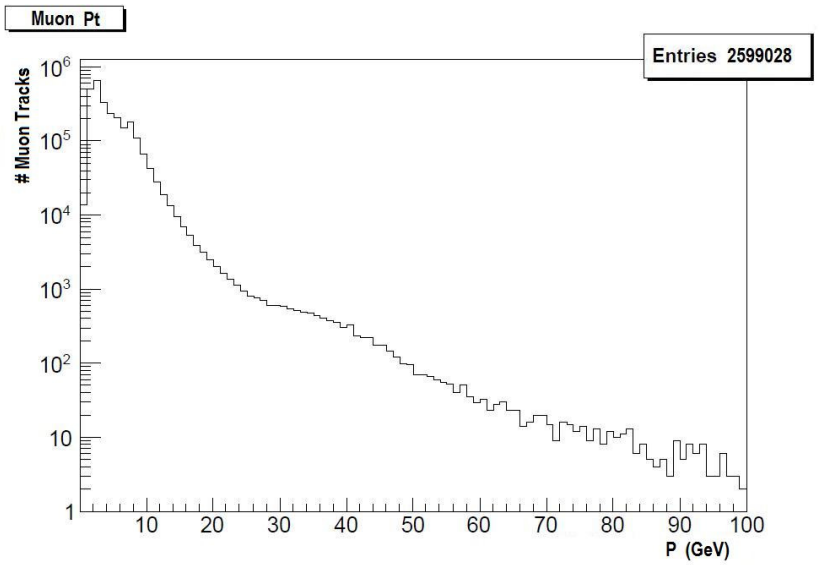

Figure 5.5: Muon Pt distribution.

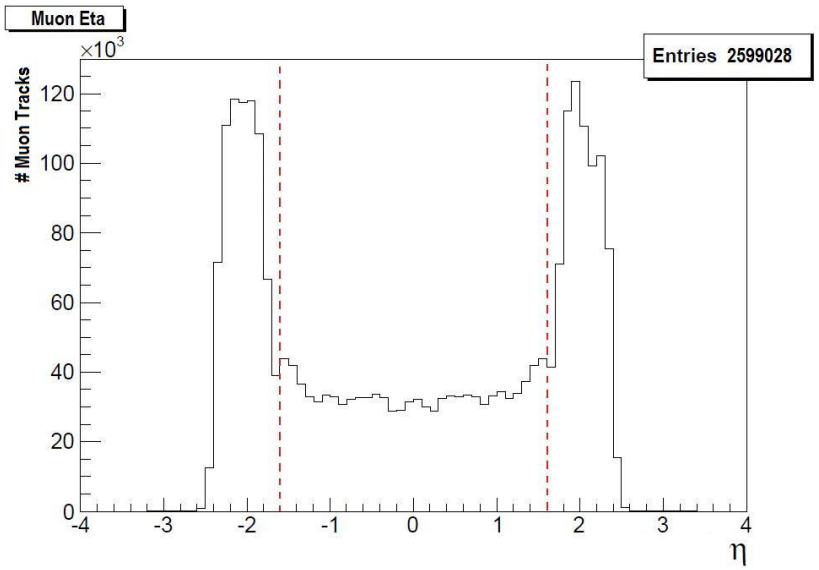

Figure 5.6: Muon η distribution

5.2.2 Detector Configuration

Barrel RPC chambers were set to an operating voltage of 9.3 kV. Two chambers, corresponding to 4 rolls, in wheel W-1 - one in the first layer of sector S4 and one in fifth layer of sector S5 - were completely switched off due to malfunctioning electronics. Almost all endcap chambers had an operating voltage of 9.5 kV. The exception being 20 chambers (60 rolls) set at 9550 V and 3 faulty chambers (9 rolls) completely switched off. All chambers had an electronic threshold of 220 mV, corresponding to 120 fC. Strips with known problems, i.e. noise values ¡ 100 Hz/cm^2 or bad synchronization, were excluded from readout. About 98% of detector channels were active.

System temperature is maintained well below 24°C, to guarantee proper RPC operation. High temperature values could cause integrity damage to the linseed oil layer on the electrodes. 310 temperatures probes are installed in the barrel region and 72 in the endcaps. Figure 5.7 shows, as an examples, the temperature measured by a single probe over the entire data taking period.

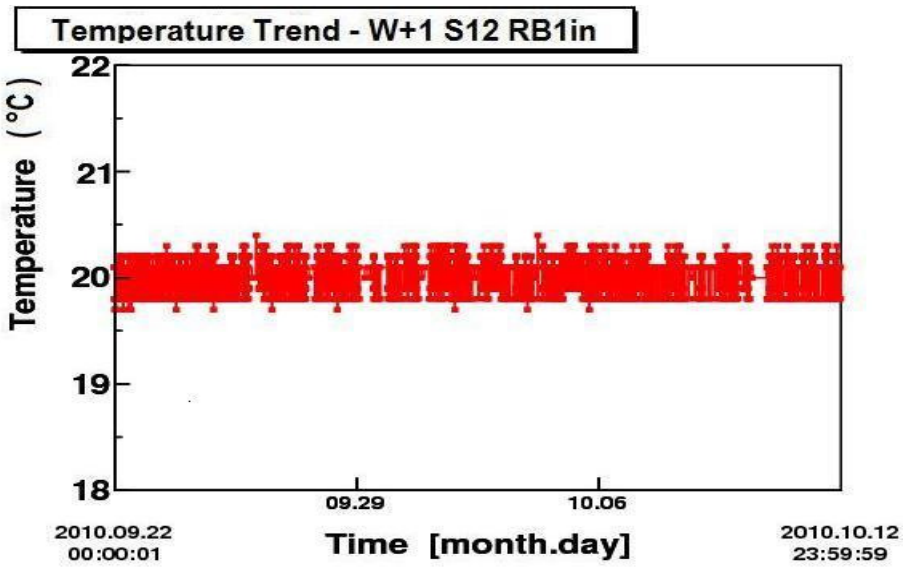

Figure 5.7: Temperature trend for chamber RB1in in sector S12 of wheel W+1. Data refers to the period: September 22nd - October 12th, 2010. Data are collected with a deadband of 0.3 °C. Deadbands are introduce to reduce data volume and avoid overloading data storage facilities.

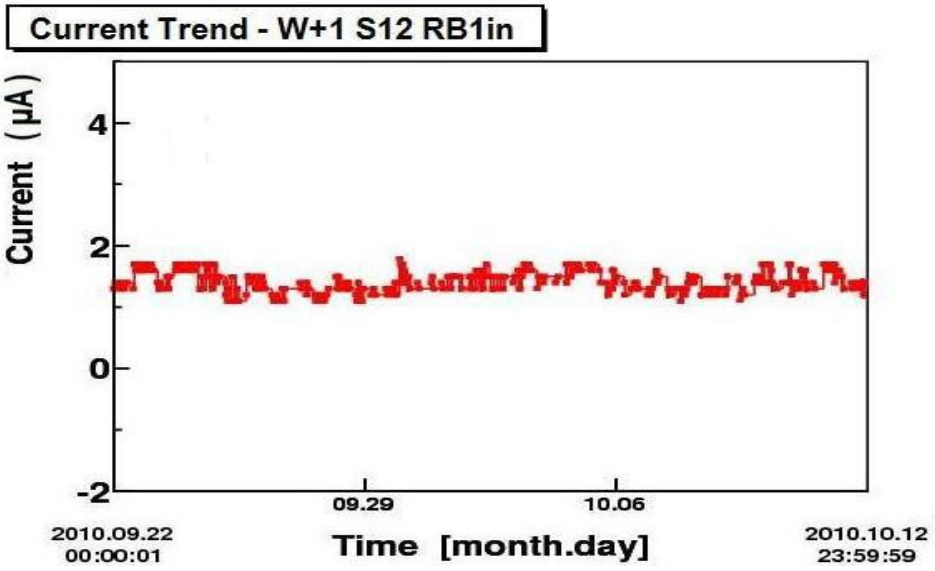

Figure 5.8: Dark current trend for chamber RB1in in sector S12 of wheel W+1. Data refers to the period: September 22^{nd} - October 12^{th}, 2010. Only periods with stable HV (no ramping-up nor ramping-down) were considered. Data are recorded with a deadband of 0.3 μA.

Also, chamber dark currents are closely monitored. A sudden current increase could indicate a malfunctioning in detector or in the electronics, lose of settings, wrong gas mixture, or simply an environmental change. Current values for the same chambers of figure 5.7 are shown, as an example, figure 5.8. Average currents were stable around 1.5 μA.

Finally the gas flowing in and out of the detector is monitored during the entire period. RPCs need to be flushed with a continuous flow of gas to avoid operating with exhausted gas. On the other hand, high flow could cause mechanical damage to the chambers. Nominal flux is set to 0.5 equivalent gas gap volumes per hour. Figure 5.9 shows the gas flows recorded, common to two barrel chambers. Average flow-in is 15.3 $\pm$ 0.4 l/h and average flow-out is 15.5 $\pm$ 0.4 l/h. Total gas gap volume is about 30 l.

Stability of detector conditions is monitored using the Quality State Machine. Figures 5.10 and 5.11 show the number of Dead and Noisy rolls (exact definitions in section 4.3) for each different runs. Runs 147116 and 147749 were relatively short, thus accumulated statistics were not enough to perform the Quality State algorithm.

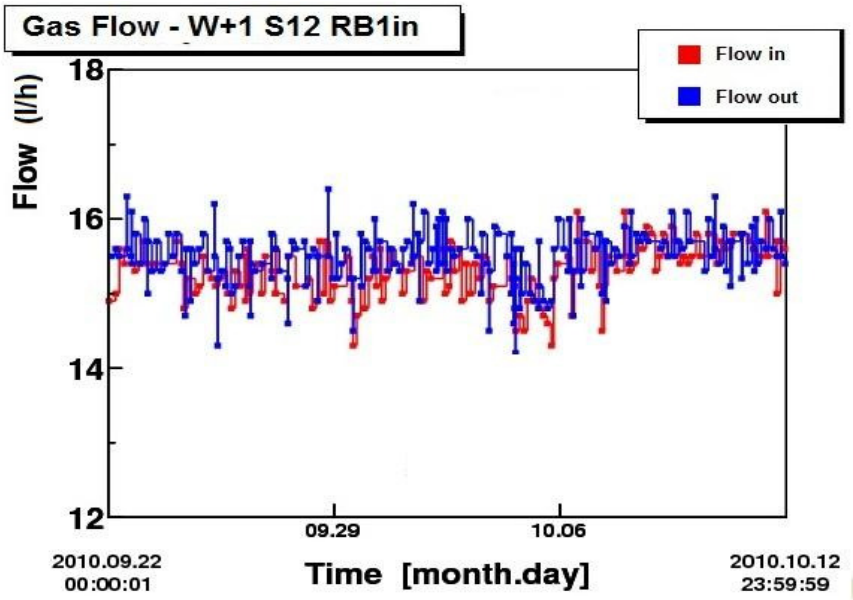

Figure 5.9: Gas flow trend (in and out of the gas gaps) for RB1in, in sector S12 of wheel W+1. Data refers to the period: September 22^{nd} - October 12^{th}, 2010. Data are collected with a deadband of 0.5 l/h.

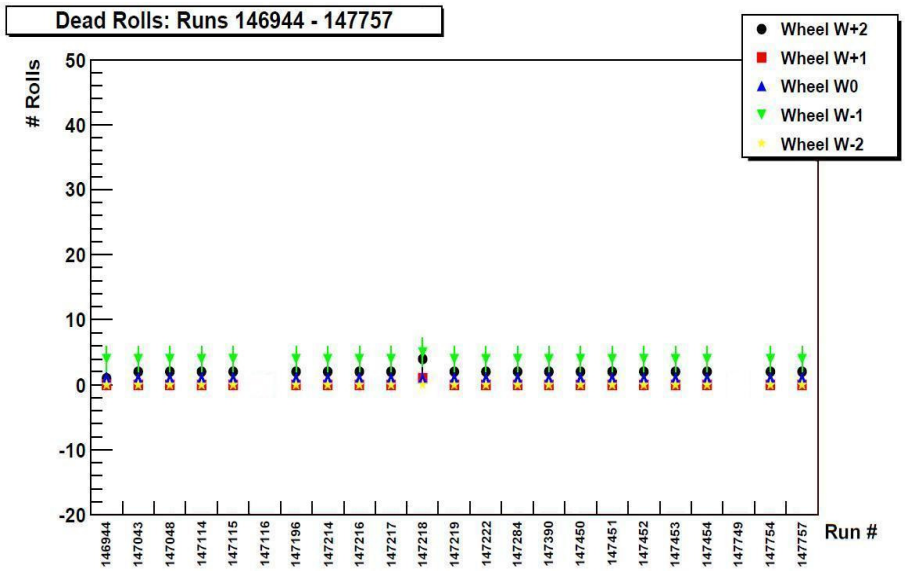

Figure 5.10: Number of Dead rolls as computed by the Quality Sate Machine algorithm as a function of the run number. For runs 147116 and 147749, no calculation was made due to lack of statistics.

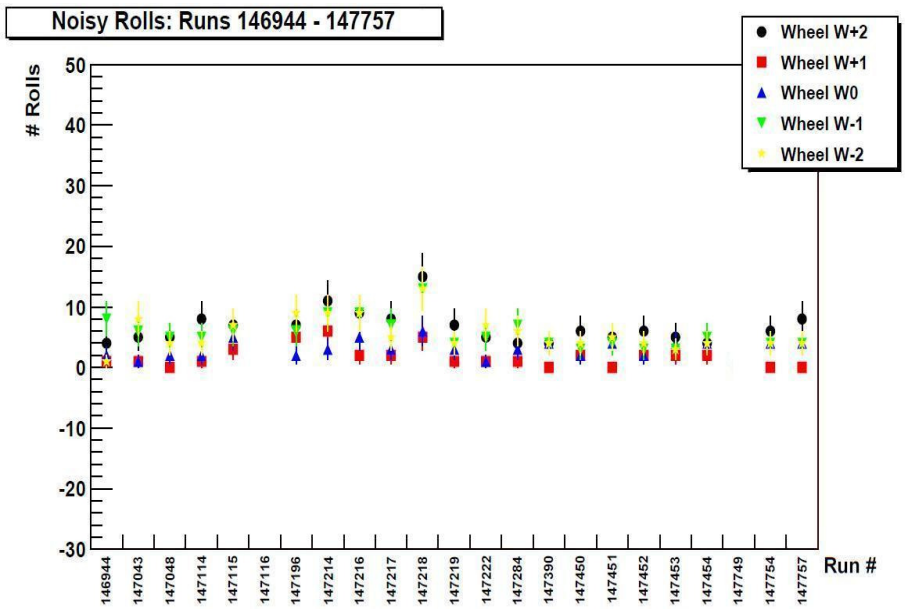

Figure 5.11: Number of Noisy rolls as computed by the Quality Sate Machine algorithm as a function of the run number. For runs 147116 and 147749, no calculation was made due to lack of statistics.

5.2.3 Results

RPC performance is studied in terms of cluster size, trigger and data synchronization, and efficiency. Meaning and physical relevance of these parameter have been discussed in detail in section 4.2.1.

Cluster Size

RPC trigger performance depends, among other things, on the cluster size, defined as the number of adjacent strips in the same roll fired at the passage of a ionizing particle. A large cluster size ($\gg 2$) could introduce uncertainties in muon pattern recognition algorithms and originate a significant number of ghost events. Figures 5.12 and 5.13 show cluster size distribution for each barrel layer and endcap ring respectively. As expected, average cluster size diminishes with increasing strip width.

Synchronization

For efficient triggering, all parts of the CMS detector must produce synchronous trigger signals for the same event. Delay of RPC trigger signal with respect to the main LHC clock is shown in figure 5.14. The delay is given in units of bunch crossing (25 ns). More than 99% of the triggers were synchronous.

Delay of RPC signals with respect to the Level-1 Trigger signal has been studied for each and every roll. Data misalignment may have negative effects on detection and reconstruction efficiency. An example of a well synchronized roll is given in figure 5.15; all hits are in the central bin. Noise signal time delay is shown (in blue) for comparison. Less than 7% of rolls in the barrel had poor synchronization, as well as about 11% of rolls in the endcaps.

Chamber Efficiency

Muon detection efficiency has been calculated for every roll, by making use of the independent tracking and trigger information provided by DTs in the barrel and CSCs in the endcaps. Figures 5.16 and 5.17 show average efficiency distributions for barrel and endcaps respectively. Rolls with known problems are excluded. More than 95% of rolls in the barrel and about 89% in the endcaps have efficiency greater $\geq 90\%$.

Local efficiency are also performed. Figure 5.18 shows an example of an endcap roll with high (average efficiency = 98%) and uniform efficiency. The typical trapezoidal shape is clearly seen. The lower efficiency regions, visible as small yellow spots, are due to the PVC spacers. Instead, an example of a problematic chamber is given in figure 5.19. The extended region at low efficiency is probably due to gas flow problems.

Residuals distributions are also studied (figures 5.20 and 5.21). Residuals are defined as the distance between the extrapolated muon track impact point and the closest RPC hit. Sigmas of these distributions are equal to 1.3 cm for the barrel and to 1.2 cm for the endcaps. Values agree with expected spacial resolution of the order of the cm.

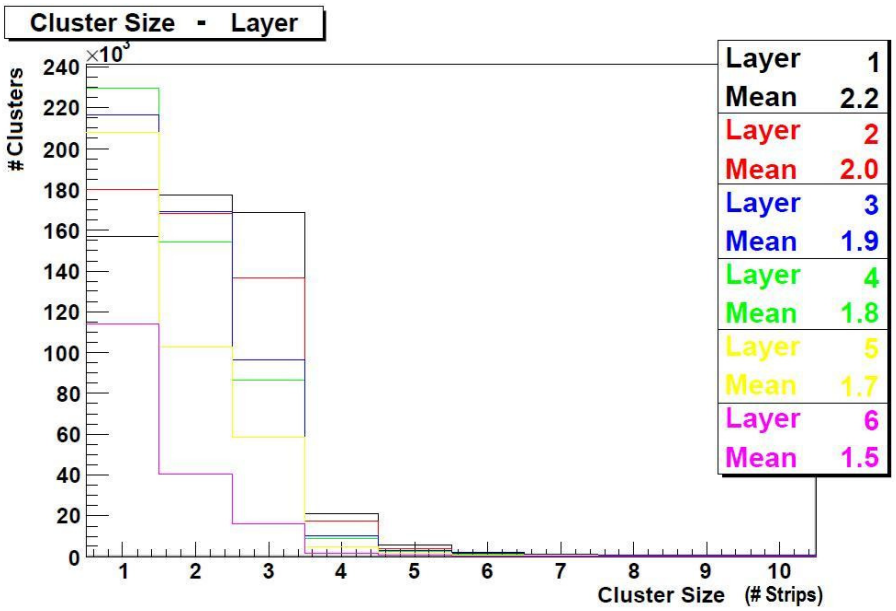

Figure 5.12: Cluster size distributions per layer. Average cluster size diminishes with increasing layer number, i.e. with increasing strip width.

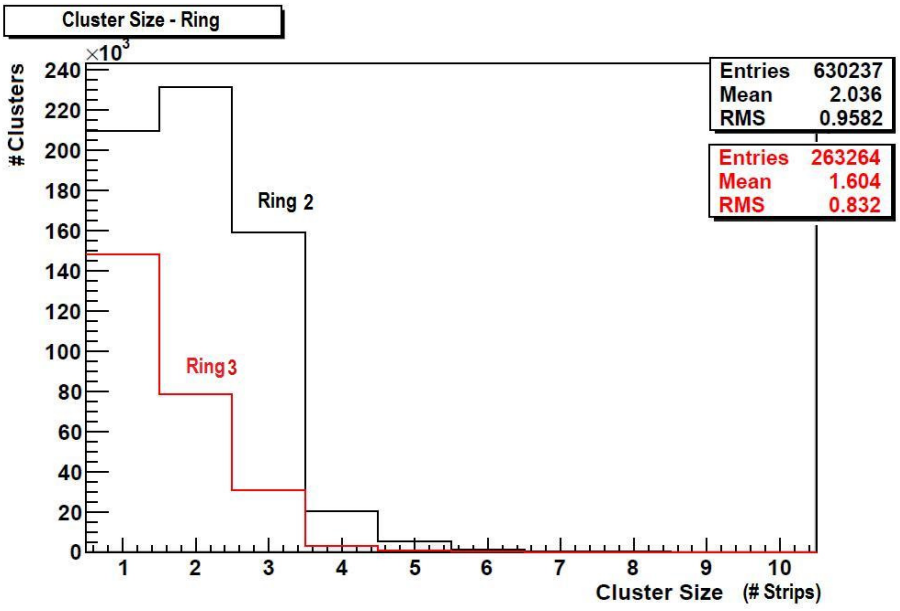

Figure 5.13: Cluster size distributions per ring. Average cluster size diminishes with increasing strip width.

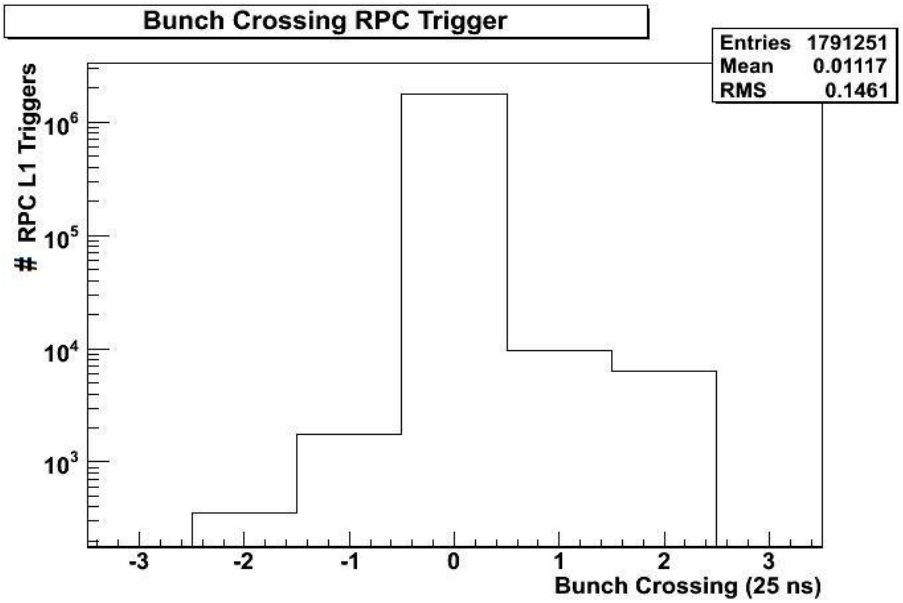

Figure 5.14: Delay of RPC trigger signal with respect to the main LHC clock.

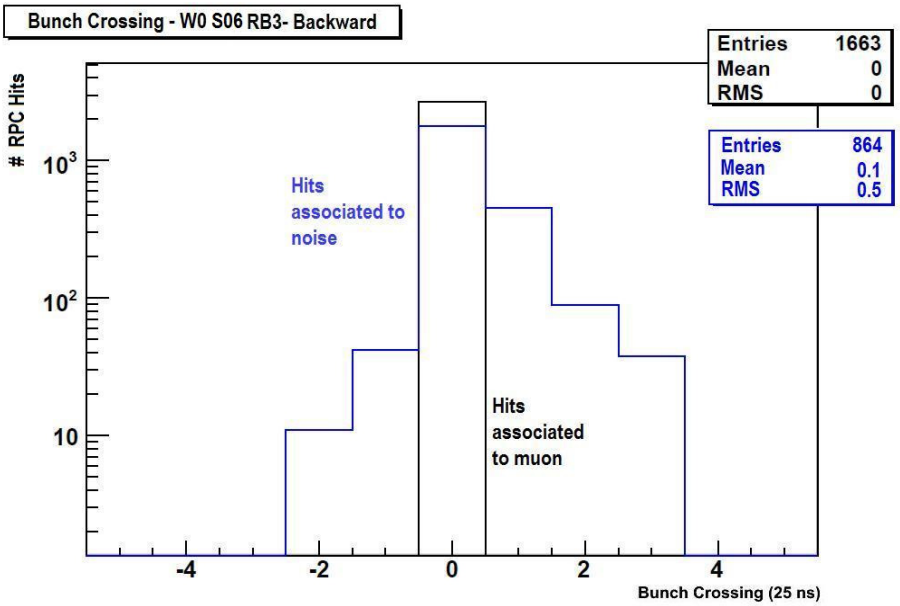

Figure 5.15: Delay of the RPC signals (in black) with respect to the Level-1 Trigger signal for roll RB3- Backward in wheel W0 sector S6. Noise signal time delay is shown (in blue) for comparison.

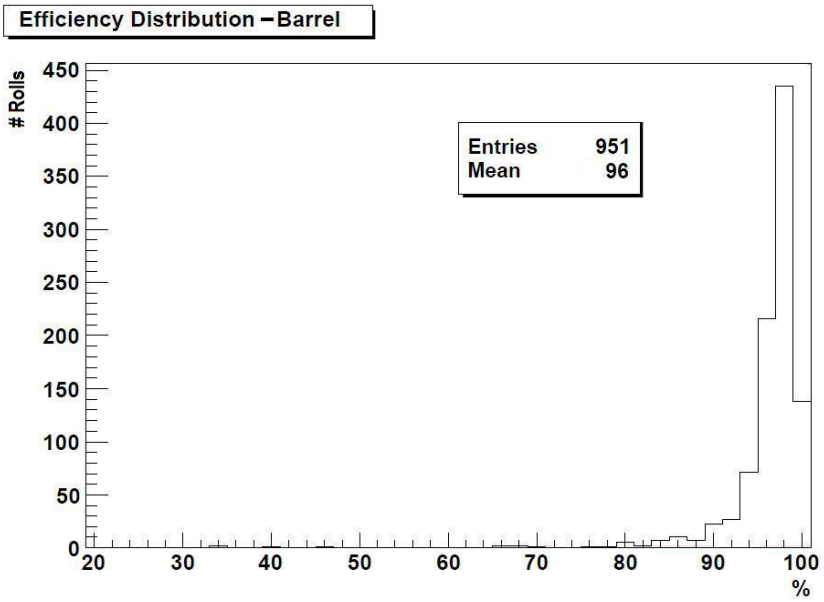

Figure 5.16: Average efficiency distribution for barrel rolls.

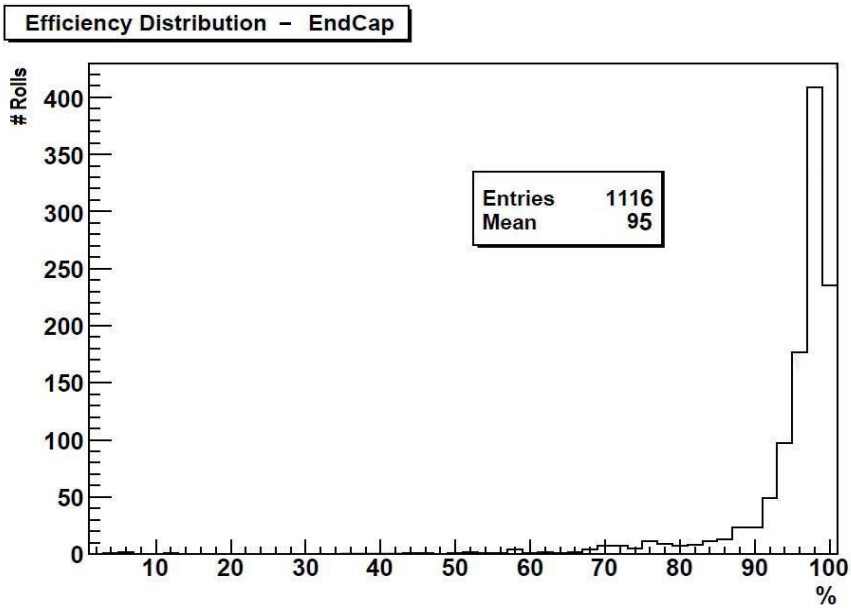

Figure 5.17: Average efficiency distribution for endcap rolls.

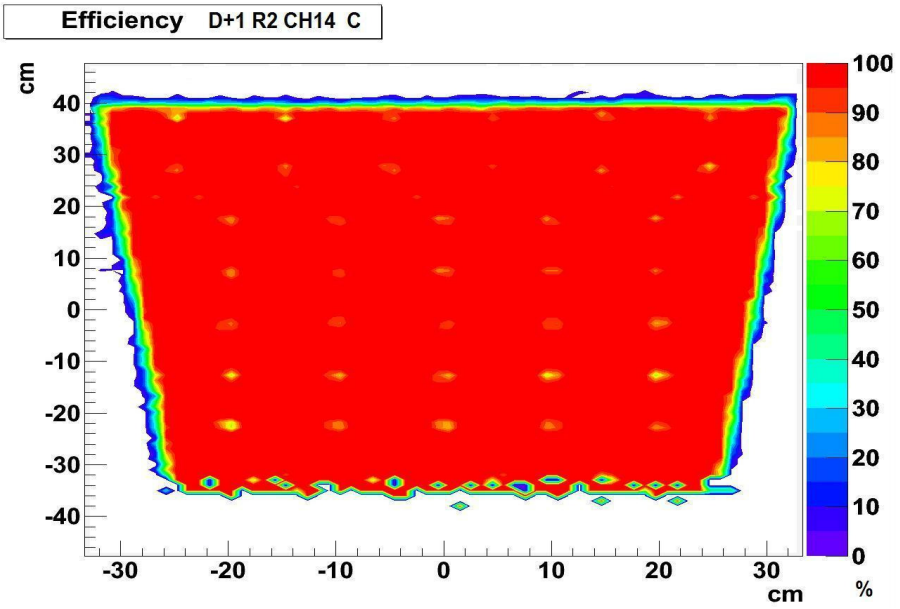

Figure 5.18: Local efficiency for roll CH14 C in disk D+1 ring R2. The typical trapezoidal shape is clearly seen. The lower efficiency regions, visible as small yellow spots, are due to the PVC spacers.

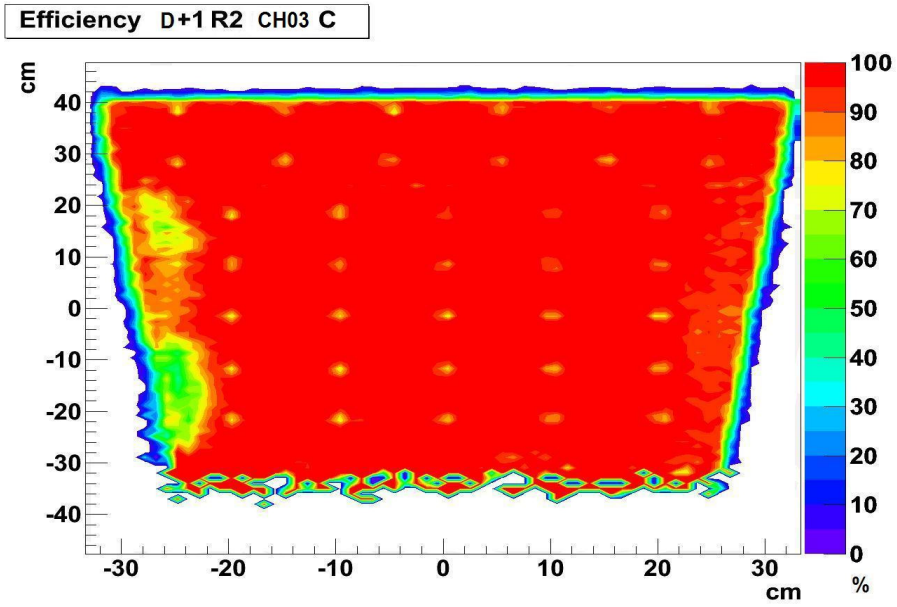

Figure 5.19: Local efficiency for roll CH03 C in disk D+1 ring R2. The extended low efficiency region on the left side is probably due to problems in the gas flow.

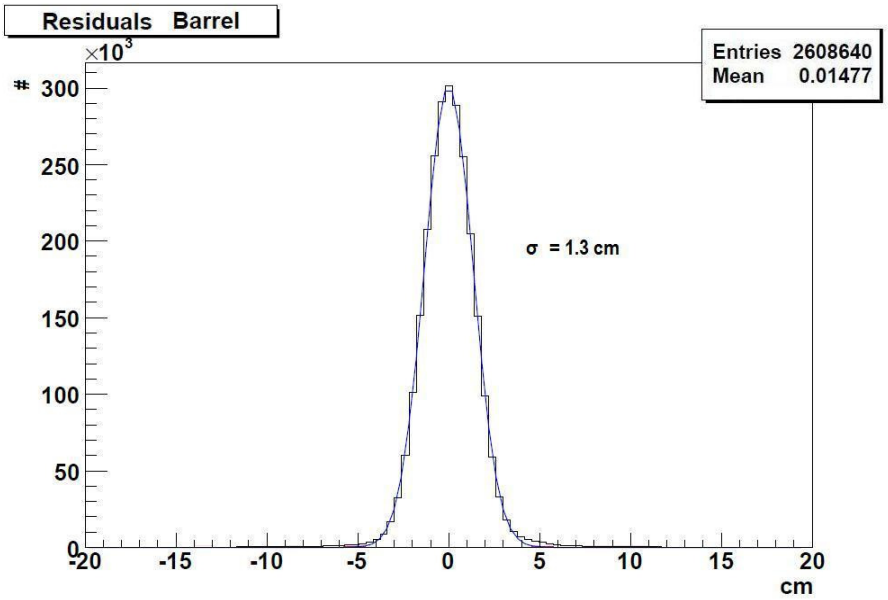

Figure 5.20: Residuals distribution for barrel rolls.

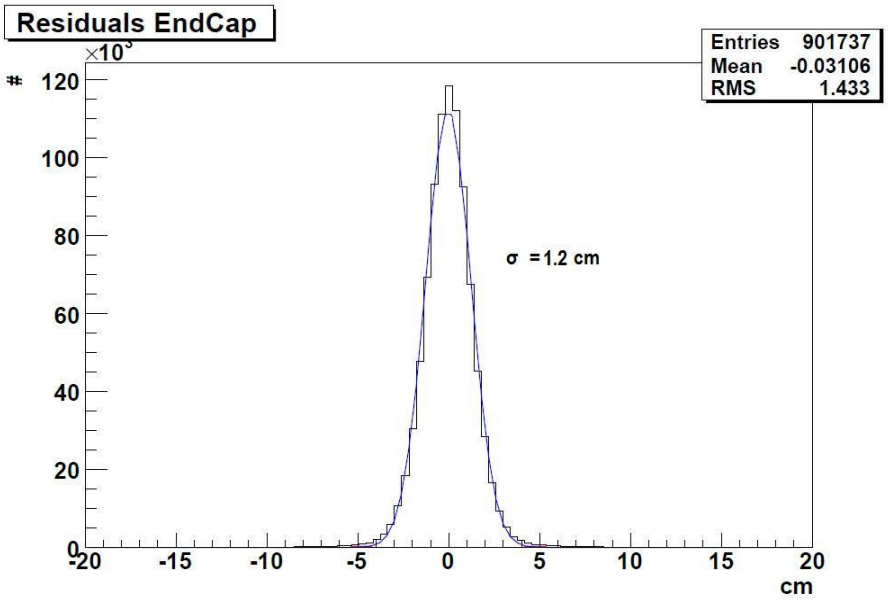

Figure 5.21: Residuals distribution for endcap rolls.

Conclusions

This doctoral thesis work has been carried out in the frame of the Compact Muon Solenoid (CMS) experiment at LHC. Its focus has been the data monitoring and performance studies of the Resistive Plate Chamber (RPC) subdetector. The author has been following this project over the last three years, as main responsible for the RPC DQM Group, taking part at the compilation of the requirements, as well as the design and development of the RPC DQM system, currently used by the CMS Collaboration. This has required a deep knowledge of detector physics and of the various RPC subcomponents, as well as their behavior under different working conditions. This doctoral thesis work has been published as a CMS Note [104] and presented at the 12^{th} Topical Seminar on Innovative Particle and Radiation Detectors (IPRD10), in June 2010 in Siena, Italy.

DQM covers the tasks of debugging hardware, monitoring detector and trigger behavior, certifying data quality, and validating alignment/calibration results, software releases, and simulated data. It has been developed within the CMS reconstruction and physics analysis software framework (CMSSW) and based on object-oriented programming languages. It is flexible, scalable, and easily customizable so to be used within different monitoring environments. Online applications run as an integral part of the event data processing. Instead, offline applications runs as part of the reconstruction process at Tier-0 and at the Tier-1s.

Monitoring information, which includes histograms, alarm states, and quality test results, is provided to experts and shifters through a web-based graphical user interfaces and stored to ROOT files. Twenty-four-seven shifts take place at the "on-detector" CMS control room, supported by daytime shifts at remote control rooms (CERN, DESY, Fermilab). Inconsistencies in data or deviations from reference distributions are promptly reported and appropriate corrective actions are take to maintain detector stability and ensure high quality data.

The monitoring system is completed by the History plotting tool for Data Quality Monitoring (HDQM), which allows to follow the evolution of detector performance in time and across different runs.

The RPC DQM has proven to comply with all CMS specifications and has been successfully integrated in the central CMS DQM in 2009. Regular upgrades and improvements have been performed, following the tight CMS software update schedule. A total of 1979 collision runs were successfully certified in 2009 and 2184 in 2010. Certification decisions were based on the results of standard quality and statistical tests, as well as on the output of the Quality State Machine (QSM) algorithm. The QSM has been custom developed by the RPC DQM Group to fulfill the need of automation in monitoring processes while describing the system in an accurate way.

DQM was been used to study RPC detector and trigger performance. A sample of 13485 nb^{-1} of 7 TeV data, recorded by CMS during 2010, has been analyzed. About 98% of the detector was active. The remaining percentage suffered from known problems and was excluded from readout. More than 99% of RPC trigger signals were synchronous with the main LHC clock. Average efficiency is 96% in the barrel and about 95% in the endcaps. Average cluster size per layer or per ring was $\lesssim 2$. All measurements are in good agreement with previous results in cosmic ray studies, as reported.

This first year of extensive data taking has also been used as a system benchmark and the RPC DQM lived up to the challenge. Heavily used by both detector-experts and shifters, it has shown, time and again, its critical importance for correct detector operation and for reliable certification of data for physics analyses.

Acknowledgments

It is a pleasure to thank the many people who made this thesis possible.

It is difficult to overstate my gratitude to my supervisors, Dr. Pierluigi Paolucci and Prof. Crisostomo Sciacca. Throughout the last three years, they provided encouragement, sound advice, and good teaching.

Deep gratitude goes to Dr. Andreas Meyer, convener of the CMS DQM project, for giving me many pointers and detailed explanations.

I also benefited from many discussions with the members of the wider RPC community. Particular thanks are due to Dr. Davide Piccolo and Dr. Luca Lista for their kind help, advice and discussions.

I am indebted to my many colleagues, for providing a stimulating and fun environment in which to learn and grow. I am especially grateful to Orso Iorio, Michele De Gruttola, and Annapaola De Cosa.

I wish to thank my dear friends Rita Carbone and Filip Thyssen for helping me get through the difficult times, and for all the emotional support, comradeship, entertainment, and caring they provided.

Lastly, and most importantly, I wish to thank my parents. They bore me, raised me, supported me, taught me, and loved me. To them I dedicate this thesis.

Bibliography

[1] P. Langacker, arXiv:hep-ph/0901.0241 (2009).

[2] S.Weinberg, Phys. Rev. Lett. 19 1264 (1967).

[3] A.Salam, Elementary particle Theory , Ed. N. Svarholm (1968).

[4] ALEPH Collaboration, DELPHI Collaboration, L3 Collaboration, OPAL Collaboration, SLD Collaboration, LEP Electroweak Working Group, SLD Electroweak Group, and SLD Heavy Flavour Group, Phys. Rept. 427 (2006) 257.

[5] DØ Collaboration, S. Abachi et al., Phys. Rev. Lett. 78 (1997) 3818-3823.

[6] CDF Collaboration, A. A. Affolder et al., Phys. Rev. Lett. 84 (2000) 835-840.

[7] http://www-cdf.fnal.gov/physics/new/top/top.html.

[8] Q.R. Ahmad, et al., Phys. Rev. Lett. 87 (2001) 071301.

[9] P. W. Higgs, *Phys. Lett.* **12**, 132 (1964).

[10] P. W. Higgs, *Phys. Rev.* **145**, 1156 (1966).

[11] G. 't Hooft and M. J. G. Veltman, *Nucl. Phys.* **B50**, 318 (1972).

[12] B. W. Lee and J. Zinn-Justin, *Phys. Rev.* **D7**, 1049 (1973).

[13] G. Arnison et al., *Phys. Lett.* **B166**, p. 484 (1986).

[14] R. Ansari et al., *Phys. Lett.* **B186**, p. 440 (1987).

[15] http://pdg.lbl.gov/2010/tables/contents_tables.html.

[16] T. Hambye and K.Riesselmann, *Phys. Rev.* D **55** 7255, 1997, (Preprint arXiV:hep-ph/9610272).

[17] J. A. Casas and M. Quiros, *Phys. Rev.* B **342** 171, 1995, (Preprint arXiV:hep-ph/9409458).

[18] J. A. Casas and M. Quiros, *Phys. Rev.* B **382** 374, 1996, (Preprint arXiV:hep-ph/9603227).

[19] M. Quiros, *The Nature of the Higgs Sector* Journal of Physics: Conference Series **171** (2009) 012010.

[20] *LEP Design Report*, CERN-LEP/84-01, International report, CERN (1984).

[21] *Design report Tevatron 1 Project*, FERMILAB-DESIGN-1982-01, (1982).

[22] http://lepewwg.web.cern.ch/LEPEWWG/.

[23] The TEVNPH Working Group for the CDF and DØ Collaborations, *Combined CDF and DØ Upper Limits on Standard Model Higgs-Boson Production with up to 6.7 fb^{-1} of Data*, submitted to High Energy Physics - Experiment, (July 26th 2010), arXiv:1007.4587v1 [hep-ex].

[24] T. Hambye and K. Riesselmann, *SM Higgs Mass Bounds from Theory*, hep-ph/9708416.

[25] Tegmark, M. et al., Cosmological parameters from SDSS and WMAP, Phys. Rev. D 69 (2004) 103501.

[26] S. Weinberg,*The Quantum Theory of Fields, Volume 3: Supersymmetry*, Cambridge University Press, Cambridge, (1999). ISBN 0-521-66000-9.

[27] A. Leike, Phys. Rept. 317 (1999) 143-250.

[28] C. T. Hill and E. H. Simmons, Phys. Rept. 381 (2003) 235-402.

[29] K. D. Lane, Technicolor 2000, hep-ph/0007304.

[30] N. Arkani-Hamed, A. G. Cohen, and H. Georgi, Phys. Lett. B513 (2001) 232-240.

[31] N. Arkani-Hamed, A. G. Cohen, E. Katz, and A. E. Nelson, JHEP 07 (2002) 034.

[32] The Large Hadron Collider Project, http://lhc.web.cern.ch/lhc/.

[33] http://www.cern.ch.

[34] ATLAS Collaboration, *ATLAS Detector and Physics - Performance Technical Design Report*, Vol. I, CERN/LHCC 99-14, 1999.

[35] CMS Collaboration, *The Compact Muon Solenoid - Technical Proposal*, CERN/LHCC 94-38, 1995.

[36] ALICE Collaboration, *ALICE technical proposal*, CERN/LHCC 95-71 LHCC / P3, 1995.

[37] LHCb Collaboration, *LHCb technical proposal*, CERN/LHCC 98-004 LHCC / P4, 1998.

[38] CMS Collaboration, D. Acosta (Ed.), *CMS, Physics Technical Design Report, Vol. 1: Detector Performance and Software*, CERN-LHCC-2006-001.

[39] CMS Collaboration, A. De Roeck (Ed.), *CMS, Physics Technical Design Report, Vol. 2: Physics Performance*, CERN-LHCC-2006-021.

[40] *ATLAS: Detector and Physics Performance Technical Design Report. Vol. 1*, CERN-LHCC-99-14.

[41] *ATLAS Detector and Physics Performance. Technical Design Report. Vol. 2*, CERN-LHCC-99-15.

[42] M. Spira and P. M. Zerwas, *Electroweak Symmetry Breaking and Higgs Physics*, CERN-TH/97-379 (1997).

[43] B. Aubert et al. [BABAR Collaboration], Phys. Rev. Lett. **87**, 091801 (2001).

[44] The LHC Study Group, *The Large Hadron Collider Conceptual Design*, CERN/AC 95-05 (1995).

[45] https://twiki.cern.ch/twiki/bin/view/CMSPublic/LumiPublicResults2010.

[46] http://www.bnl.gov/rhic/.

[47] CMS collaboration, *The CMS tracker system project: technical design report*, CERN-LHCC-98-006, http://cdsweb.cern.ch/record/368412.

[48] CMS collaboration, *The CMS tracker: addendum to the technical design report*, CERN-LHCC-2000-016, http://cdsweb.cern.ch/record/490194.

[49] CMS collaboration, *The electromagnetic calorimeter project: technical design report*, CERN-LHCC-97-033, http://cdsweb.cern.ch/record/349375.

[50] CMS collaboration, *ECAL: addendum to the technical design report*, CERN-LHCC-2002- 027, http://cdsweb.cern.ch/record/581342.

[51] R. Loos et al., *CMS ECAL Preshower and Endcap Engineering Design Review. v.2 - Preshower*, CMS-2000-054-MEETING, CERN-ECAL-EDR- 4, http://cdsweb.cern.ch/record/539819.

[52] CMS collaboration, *The hadron calorimeter project: technical design report*, CERN-LHCC-97-031, http://cdsweb.cern.ch/record/357153.

[53] S. Abdullin et al., D*esign, performance, and calibration of CMS hadron-barrel calorimeter wedges*, Eur. Phys. J. 55 (2008) 159, CMS-NOTE-2006- 138, http://cdsweb.cern.ch/record/1049915.

[54] D. Denterria et al., *CMS physics technical design report: addendum on high density QCD with heavy ions*, J. Phys. G 34 (2007) 2307, CERNLHCC- 2007-009, http://cdsweb.cern.ch/record/1019832.

[55] CERN/LHCC 97-32, CMS Collaboration, *The Muon Project, Technical Design Report*, (1997).

[56] CERN/LHCC 2000-38, CMS Collaboration, *The TriDAS Project, Technical Design Report, Volume 1: The Trigger Systems*, CERN-LHCC-2000-038, http://cdsweb.cern.ch/record/706847.

[57] M. Jeitler et al. *The Level-1 Global Trigger for the CMS Experiment at LHC*, Presented at the 12th Workshop on Electronics for LHC Experiments and Future Experiments, http://wwwhephy.oeaw.ac.at/p3w/electronic1/ GlobalTrigger/GlobalTrigger.htm.

[58] CMS collaboration, The TriDAS project, technical design report. Volume 2: Data acquisition and high-level trigger technical design report, CERNLHCC- 2002-026, http://cdsweb.cern.ch/record/578006.

[59] J. Shiers, *The Worldwide LHC Computing Grid (worldwide LCG)*, Computer Physics Communications 177, 219 - 223 (2007), no. 1-2.

[60] CMS Collaboration, *CMS: The computing project. Technical design report*, CERN-LHCC-2005-023.

[61] E Rutherford, H. Geiger, "An Electrical Method of Counting the Number of a-Particles from Radio-Active Substances," Proceedings of the Royal Society (London) A 81, 141-161 (1908).

[62] W. Price: *Nuclear Radiation Detection*, McGraw-Hill, New York (1958).

[63] J. W. Keuffel: *Parallel-Plate Counters*, Rev. Sci. Instrum. 20 (1949), 202-8.

[64] M. Conversia, L. Federici: *Flash chambers of plastic material*, Nucl. Instr. and Meth. 151 (1978) 93 - 102.

[65] Yu.N. Pestov: *Status and Future Developments of Spark Counters with Localized Discharge*, Nucl. Instr. and Meth. 151 (1978) 45 - 47.

[66] Y.N. Pestov e G.V. Fedotovich, Preprint IYAF 77-78, SLAC Translation 184 (1978).

[67] R. Santonico e R. Cardarelli: *Development of Resistive Plate Counters*, University of Chicago, E. Fermi Institute('04), Nucl. Instr. and Meth. 187 (1981).

[68] R. Santonico e R. Cardarelli: P*rogress in Resistive plate counters*, Nucl. Instr. and Meth. A 263 (1988).

[69] E. Cerron Zeballos et al.: *High Rate Resistive Plate Chambers*, Nucl. Instr. and Meth. A 367 (1995) 388-393.

[70] W. R. Leo, *Techniques for Nuclear and Particle Physics Experiments*, 1987.

[71] A. von Engel, *Ionized Gases*, Clarendon Press, Oxford, 1955.

[72] M. Maggi, *Preliminary results on double-gap RPC in a high background environment*, Proceedings at the IV International Workshop on RPC and related detectors, Napoli (1997).

[73] M. Abbrescia et al., *A Model for the simulation of RPCs in avalanche mode*, Proceeding in the 4th International Workshop on Resistive Plate Chambers and Related Detectors, Napoli 1997.

[74] M.Abbrescia et al., *The Simulation of RPCs in avalanche mode*, Proc. of the 4th Int. Workshop on RPC and Related Detectors, Napoli, Italy, 15-16 Oct. 1997.

[75] V. Radeka, Ann. Rev. Nucl. Part. Sci. 38 (1988) 217.

[76] E. Cerron Zeballos et al., **CERN/PPE/95-166**.

[77] G. Pugliese, *The RPC System for the CMS Experiment*, at the IEEE Conference, San Diego 1-November 2006.

[78] M.Abbrescia et al.:*Effect of the Linseed Oil Treatment on the Performance of the Resistive Plate Counters*, CMS NOTE-1997/018 .

[79] P. Vitulo et al., *Propreties of Bakelite surfaces*, Proceeding in the 4th International Workshop on Resistive Plate Chambers and Related Detectors, Napoli 1997.

[80] M. Abbrescia et al., *The simulation of resistive plate chambers in avalanche mode: charge spectra and efficiency*, Nucl. Instr. and Meth. A (1999).

[81] G. Pugliese on behalf of the CMS Collaboration, *The RPC system for the CMS experiment*, 2006 IEEE Nuclear Science Symposium Conference Record, 2006.

[82] M. Abbrescia et al., *Properties of $C_2H_2F_4$ based gas mixtures for avalanche mode operation of Resistive Plate Chambers*, CMS Note 97/004.

[83] P.Camarri et al., *Streamer suppression with SF_6 in RPCs operated in avalanche mode*, Nucl. Instr. and Meth. A 414 (1998).

[84] A. Benussi et al., *The CMS RPC gas gain monitoring system: An Overview and Preliminary Results.*, Nucl. Instrum. Meth. A 602 (2009) 805-808.

[85] A. Paoloni et al., *RPC operation at high temperature*, Nucl. Instr. and Meth. A 508 (2003).

[86] A. Benussi et al., *The CMS RPC gas gain monitoring system: An Overview and Preliminary Results.*, Nucl. Instrum. Meth. A 602 (2009) 805-808.

[87] G. Iasselli et al., *Study of the detailed Geometry of the Barrel RPC Strips*, CMS IN 2000/044.

[88] J. Królikowski et al. *Acceptance of the Baseline and Modified RPC System Geometry*, CMS IN 2001/026.

[89] D. Acosta et al., *CMS High Level Trigger*, CERN CMS Analysis NOTE 2007/009, 2007.

[90] The CMS Collaboration, *The Trigger Project, Technical Design Report: the Level-1 Trigger*, CERN/LHCC 2000-038, 2000.

[91] N. Amapane et al. *Monte Carlo Simulation of Inclusive Single- and di-Muons Samples*, CMS NOTE 2002/041, 2002.

[92] J. Erö et al., *The CMS drift tube trigger track finder*, CMS-NOTE-2008-009, http://cdsweb.cern.ch/record/1103001.

[93] D. Acosta et al., *Performance of a pre-production track-finding processor for the level-1 trigger of the CMS endcap muon system*, Proceedings of the 10th Workshop on Electronics for LHC and Future Experiments, Boston U.S.A. (2004), http://cdsweb.cern.ch/record/814321.

[94] Z. Jaworski, I.M. Kudla, W. Kuzmicz, M. Niewczas, *Resistive Plate Chamber (RPC) based muon trigger system for the CMS experiment - pattern comparator ASIC*, Nucl. Instr. and Meth. in Phys. Res A 419, pp. 707-710, 1998.

[95] H. Sakulin et al., *The Level-1 Global Muon Trigger for the CMS Experiment.*, Proceedings of 9th LECC 2003 Workshop, Amsterdam, The Netherlands, 29 Sep. - 3 Oct. 2003, CERN CMS CR2003/040.

[96] A. Afaq et al. *The CMS High Level Trigger System*, IEEE Transactions on Nuclear Science, VOL. 55, NO. 1, February 2008.

[97] R. E. Kalman, *A new approach to linear filtering and prediction problems*, Transaction of the ASME-Journal of Basic Engineering, vol. 35, 1960.

[98] K. Bunkowski, *Optimization, Synchronization, Calibration and Diagnostic of the RPC PAC Muon Trigger System for the CMS detector Authors*, CMS TS-2010/009, 2010.

[99] L. Tuura, A.B. Meyer, I. Segoni and G. Della Ricca *CMS data quality monitoring: systems and experiences* Proc. CHEP09, Computing in High Energy Physics, (Prague, Czech Republic) 2009.

[100] CMS Collaboration, *Commissioning of the CMS High-Level Trigger with cosmic rays*, arXiv:0911.4889 [physics.ins-det].

[101] L.Tuura, L. Eulisse, A.Meyer, *CMS Data Quality monitoring web service*, Proc. CHEP09, Computing in High Energy (2009).

[102] http://root.cern.ch/.

[103] V. Briglijevic et al., *Run Control and Monitor System for the CMS Experiment*, CERN, Genéve, Svizzera.

[104] A. Cimmino et al., *Data Quality Monitoring for the CMS Resistive Plate Chamber Detector*, CMS NOTE 2010/013, 2010.

[105] The CMS Collaboration, *The Trigger and Data Acquisition project, Volume2 - Technical Design Report*, CERN/LHCC 2002-26, CMS TDR 6.2 (2000).

[106] S. Oualline *Practical C++ Programming* (2th ed.), O'Reilly Media (2002).

[107] M. Lutz *Learning Python* (4th ed.), O'Reilly Media (2009), ISBN 978-0596158064.

[108] S. Chatrchyan et al. [CMS Collaboration], *Commissioning of the CMS Experiment and the Cosmic Run at Four Tesla.*, JINST **5** (2010) T03001 [arXiv:0911.4845 [physics.ins-det]].

[109] S. Costantini et al,. *Noise Monitoring Tools with RPC Online and Offline Data*, CMS IN -2010/002, 2010.

[110] Wagner, F., *Modeling Software with Finite State Machines: A Practical Approach*, Auerbach Publications, 2006, ISBN 0-8493-8086-3.

[111] CMS Collaboration, *CMS Data Processing Workflows during an Extended Cosmic Ray Run*, arXiv:0911.4842v2 [physics.ins-det].

[112] A. Afaq et al., *The CMS Dataset Bookkeeping Service*, Journal of Physics: Conference Series 119 (2008) 072001.

[113] D. Giordano, A.-C. Le Bihan, A. Pierro and M. De Mattia, *History Plotting Tool for Data Quality Monitoring*, Nuclear Inst. and Methods in Physics Research A, Reference: NIMA50295, DOI information: 10.1016/j.nima.2009.06.109.

[114] CMS Collaboration, *34. Performance Study of the CMS Barrel Resistive Plate Chambers with Cosmic Rays.*, CMS-CFT-09-010, JINST 5 T03017 (2010).

[115] R. Trentadue on behalf of the CMS Collaboration, *CMS RPC trigger and detector performance during the 2009 Cosmic Run At Four Tesla (CRAFT09)*, 2009 IEEE Nuclear Science Symposium Conference Record N13-178 (2009).

[116] G. Abbiendi et al, *Muon Reconstruction in the CMS Detector.*, CMS AN-2008/097 (2008).